Institute for Anatomy and Cell Biology
Department of Neuroanatomy

Theoretical Medicine and Biosciences
of the Faculty of Medicine
of the Saarland University, Homburg/Saar


# Retinoic Acid Signaling during Homeostatic Synaptic Plasticity

A thesis submitted to the

Faculty of Medicine of the Saarland University

in fulfillment of the requirement for the degree of

**Doctor of Philosophy (Ph.D.)**

2017

Submitted by

**Maik Hintze**

born 1 May, 1986
in Potsdam, Germany

Supervisor:

Co-supervisor:

**Declaration (Eigenständigkeitserklärung)**

I hereby declare that this Ph.D. thesis entitled

**Retinoic Acid Signaling during Homeostatic Synaptic Plasticity**

is a presentation of my original research work. No sources or aids other than those quoted and listed as references have been used.

No portion of this work has been submitted elsewhere in support of any application for any degree or other qualification.

Homburg, 07 February, 2017

Maik Hintze

## Acknowledgements

The work described in this manuscript has been greatly supported by numerous people, who not only provided helpful suggestions and hands-on help about how to perform experiments, but also gave mental support through their friendship. I wish to express my gratitude to all the people who have worked with me and supported me personally.

I feel very grateful to Prof. Frank Schmitz who has always been very supportive throughout the time of my Ph.D. studies, and who gave me valuable input and guidance through his visits at Stanford. It was him who made this whole project possible in the first place, and it is great pleasure working and discussing with him.

I am deeply indebted to Dr. Lu Chen, Stanford University, for entrusting me with such a challenging project and for her continuous mentorship. It has been a great pleasure working with such an enthusiastic scientist, and I will continue to benefit from the curiosity of mind that she taught me.

I also want to acknowledge the tremendous support I received through Prof. Thomas Franz, Bonn University, who allowed me to work in his lab and continue my studies after my return to Germany. Many experiments described in this manuscript would not have been completed without his generous support.

I feel personally attached to many members of the Chen Lab with whom I have shared three years of ups and downs through the rocky landscape of scientific experiments. I specially thank Shubha for her kindness and friendship which were of utmost value and will remain my best personal memories through the years of my Ph.D. The other lab members who have become more friends than colleagues will not be forgotten, namely Tony, Fede, Esther, Ada, Xiao Zhenjie, Kristin, Yu-Tien, Ray, Jessie, and Angela. Working with them as well as fruitful discussions have been some of the most pleasant memories of my Ph.D. work. Jinkyoung worked hard with me on the transcriptional reporter experiments to obtain some of the data that went into this manuscript.

Dr. Andrew Olson from the Stanford SIM1 Imaging Core Facility provided access to outstanding imaging equipment, and only his helpful suggestions and comments made many of the imaging experiments described in this manuscript possible.

I feel personally connected to my landlady in Palo Alto, Helen Tombropoulos, who has not only rented her room to me, but who became a true friend through her kindness and care. Dawn and Rahul who lived in the same house have also been great and pleasant company who I will not forget. I will also keep my dear friend Zhongxu from Dallas in good memory.

My stay at Stanford University was financially supported by a scholarship from the Boehringer Ingelheim Funds who through their network also provided many opportunities to get in touch with countless outstanding scholars and students, investigative minds and passionate researchers.

Of course, none of this would have been possible without the support of my family and friends in Germany and all over the world. I want to mention my dearest friends Marco, Chrissie, Bettina, Navina, Basti, Daiwei, Kati, and Nina, who have been far and yet so near.

My great thanks goes to my parents and grandparents who have never ceased to support me and whose love is beyond measures.

*Dedicated to my grandfather*

**Hermann Otten**

*(1936—2014)*

# CONTENTS

# SUMMARY

The mammalian brain is composed of billions of neurons that build functional units by forming multiple and complex connections to constitute neuronal networks. Synapses are the specialized structures through which neurons connect. The remarkable ability of the brain to analyze and generate appropriate responses to an animal's ever-changing environment is based on its power to reshape synaptic connections. Such changes of synaptic connections and neuronal network connectivity, termed synaptic and network plasticity, respectively, are seen as biological correlates of learning and memory, and deciphering their molecular mechanisms may help to understand the function of the brain as a whole.

HEBBian plasticity is a feed-forward mechanism whereby strongly activated synaptic connections get even further strengthened. Therefore, a biological feed-back loop termed homeostatic synaptic plasticity (HSP), acts as a natural regulator to avoid excessive strengthening of very active connections at the expense of less active ones. Our lab demonstrated previously that all-*trans* retinoic acid (RA) acts as a central signaling molecule during HSP. In the present study, we wanted to ask where and when RA is active during HSP, and find or develop suitable bioreporter methods to address these questions.

We first focused on transcription-based reporters that exploit RA's ability to bind to cellular RA receptors (RARs) and thereby activate transcription of specific genes. Our previously used transcription-based reporter contains a green fluorescent reporter gene (GFP) driven by a weak promoter (TK promoter) that is regulated by a RA response element (RARE-TK::GFP). This reporter suffers from a small dynamic range and allows RA detection only within a very short time window before getting saturated. We developed an improved reporter based on the yeast transcription factor Gal4 and its DNA binding sequence "upstream activating sequence" (UAS) which are both foreign to mammalian cells and thereby reduce chances of undesired cellular regulation of the reporter. Our novel design utilizes a chimeric receptor composed of the Gal4 DNA-binding domain (Gal4-DBD) and a ligand-binding domain from one of three different RARs (RAR-LBD), as

well as a firefly luciferase and enhanced GFP reporter fusion gene (fLuc-EGFP) expressed by a weak promoter ($E4_{TATA}$) located downstream of a UAS (UAS-$E4_{TATA}$::fLuc-EGFP). The chimeric Gal4-RAR receptor bound to the UAS can enhance transcription only in the presence of RA. We show that this reporter design overcomes the limitations of our previously used RARE-TK::GFP reporter and faithfully detects RA production in transfected neurons after several days of reporter expression. The stable responsiveness of the improved reporter is prerequisite for its utility for *in vivo* applications which rely on viral reporter delivery and long-term expression. We also show with both our previous and improved reporters that blocking calcineurin activity in dissociated hippocampal neuron cultures is sufficient to induce cellular RA production, suggesting that calcineurin is the critical calcium sensor that senses and relates synaptic activity levels to RA production within the HSP signaling cascade.

We next wanted to develop a method to directly indicate the presence of RA with high spatial and temporal resolution. We designed a modular sensor protein that would allow the detection of conformational changes by measurements of FÖRSTER resonance energy transfer (FRET). We fused the RARα-LBD to a NR box, a specific peptide motif which can bind to the RARα-LBD in an RA-dependent manner. This fusion protein is sandwiched between cyan (CFP) and yellow fluorescent proteins (YFP), rendering conformational changes amenable to FRET measurements. The sensor assumes an extended conformation in the absence of RA, yielding low FRET efficiency. In the presence of RA, the LBD should recruit the NR box peptide leading to a compact conformation, thus yielding higher FRET efficiency. Despite various modifications of the sensor design, we failed to obtain responsiveness to RA with this method.

We obtained a different genetically encoded sensor for RA (aGEPRA) which directly translates the RA-dependent conformational changes of the RAR-LBD into FRET changes. We successfully expressed aGEPRA in dissociated hippocampal neurons and recorded FRET changes during pharmacological blockade of synaptic activity. Within two hours of synaptic activity blockade some neurons showed increasing reporter activity

("responders") while others responded with a decrease ("non-responders"). However, almost all control cells observed for two hours without synaptic activity blockade behaved like "responders", hampering the interpretation of our results. We tend to exclude technical reasons and suggest that the lack of signal integration is a central limitation of the aGEPRA FRET sensor, prohibiting the detection of low endogenous RA levels.

Last, we tested the utility of ratiometric FRET for 2-photon microscopy. We show that quantitation of ratiometric FRET is feasible with the Clover-mRuby2 FRET pair which exhibits a large separation of the 2-photon excitation spectra between donor and acceptor fluorophores. FRET changes are also qualitatively detectable with aGEPRA even though the spectral overlap between its CFP and YFP fluorophores are spectrally less well resolved; therefore, thorough calibration of the method would be required to allow for precise absolute FRET quantification.

We conclude that only integrating, transcription-based reporters seem to provide sufficient sensitivity to detect RA levels produced during HSP. The non-integrating aGEPRA FRET sensor seems to lack the sensitivity required to visualize endogenous neuronal RA levels produced during synaptic activity blockade.

# ZUSAMMENFASSUNG

Das Gehirn besteht aus vielen Milliarden Nervenzellen, die komplexe Verbindungen eingehen um neuronale Netzwerke, die funktionellen Einheiten des Gehirns, zu bilden. Synapsen sind spezialisierte Strukturen, mit denen Nervenzellen untereinander Kontakt herstellen. Die Fähigkeit des Gehirns, auf eine sich ständig ändernde Umgebung eines Lebewesens zu reagieren basiert auf der Formbarkeit dieser synaptischen Verbindungen. Solche Veränderungen synaptischer Verbindungen und neuronaler Netzwerke werden synaptische beziehungsweise Netzwerkplastizität genannt, und sie bilden vermutlich die biologische Grundlage des Lernens und Gedächtnisses. Die diesen Prozessen zu Grunde liegenden Mechanismen zu studieren ist unverzichtbar, um die Funktionsweise des Gehirns als ganzes verstehen zu können.

HEBB'sche Plastizität ist ein Verstärkungsmechanismus, durch den hochaktive Synapsen weiter verstärkt werden können. Ein biologischer Regulationsprozess, genannt homöostatische synaptische Plastizität (HSP), wirkt der HEBB'schen Plastizität entgegen und verhindert dadurch eine Überaktivierung stärkerer Verbindungen zu Ungunsten der schwächeren. Wir konnten in früheren Untersuchungen zeigen, dass all-*trans* Retinolsäure (RA) eine zentrale Rolle in der Regulation von HSP spielt. Wir gingen in der vorliegenden Arbeit der Frage nach, wo und wann RA während der HSP aktiv ist, und testeten oder entwickelten geeignete Methoden zur Untersuchung dieser Fragestellungen.

RA kann an zelluläre RA Rezeptoren (RARs) binden und dadurch die Transkription spezieller Gene aktivieren, was man zur Entwicklung transkriptions-basierter Reporter nutzen kann. Unser bislang verwendeter transkriptions-basierter Reporter enthält ein grün fluoreszierendes Reportergen (GFP), das von einem schwachen TK Promoter unter Regulation eines RA Responselements exprimiert wird (RARE-TK::GFP). Wir haben einen verbesserten transkriptions-basierten Reporter entwickelt, der auf dem Transkriptionsfaktor Gal4 und dessen DNA-Bindungsstelle „upstream activating sequence" aus der Hefe beruht, um den dynamischen Bereich und die zeitliche Nutzbarkeit zu erweitern. Die ver-

wendeten Komponenten kommen in Säugerzellen nicht vor und sollten auch keiner unerwünschten zellulären Regulation unterworfen sein. Wir nutzen einen chimären Rezeptor bestehend aus der Gal4 DNA-Bindedomäne (Gal4-DBD) und einer RAR Liganden-Bindedomäne (RAR-LBD), sowie eine mit GFP fusionierte Leuchtkäfer-Luciferase als Reportergen (fLuc-EGFP), das von einem schwachen Promoter ($E4_{TATA}$) hinter einer UAS exprimiert wird (UAS-$E4_{TATA}$::fLuc-EGFP). Der Gal4-RAR Rezeptor bindet an die UAS und erhöht in Gegenwart von RA die Transkription des Reportergens. Wir zeigen, dass dieses Prinzip unseren vorherigen RARE-TK::GFP Reporter übertrifft, indem ein Nachweis der RA-Produktion noch nach mehrtägiger Reporterexpression gelingt, was eine Anwendung des neuen Reporters durch Virus-vermittelte Gewebsexpression *in vivo* ermöglicht. Sowohl mit unserem bisherigen als auch dem neu entwickelten Reporter konnten wir eine RA-Produktion in Nervenzellen zeigen, in denen Calcineurin pharmakologisch inhibiert wurde. Wir schließen daraus, dass Calcineurin der Calcium-Sensor ist, der synaptische Aktivität über die Calcium-Konzentration erkennt und auf dieser Grundlage die RA-Produktion während der HSP regulieren kann.

Zum Nachweis von RA mit hoher zeitlicher und räumlicher Auflösung entwickelten wir einen modularen Sensor, dessen Konformationsänderungen wir durch FÖRSTER Resonanz-Energietransfer (FRET) sichtbar machen können. Wir fusionierten die RARα-LBD mit einer NR Box - einer spezifischen Peptidsequenz, die RA-abhängig an die LBD binden kann. Anfügen von cyan (CFP) und gelbem Fluoreszenzprotein (YFP) an das NR Box-LBD Fusionsprotein sollte dessen Konformationsänderungen durch FRET messbar machen: Eine in Abwesenheit von RA gestreckte Sensorkonformation zeigt wenig FRET, während die NR Box in Gegenwart von RA an die LBD binden und eine geschlossene Konformation herbeiführen sollte, was eine höhere FRET-Effizienz bewirken würde. Trotz zahlreicher getesteter Modifikationen des Sensors gelang uns mit dieser Methode kein Nachweis RA-abhängiger Konformationsänderungen.

aGEPRA ist ein anderer FRET-basierter RA Sensor, der den Konformationswechsel der RAR-LBD direkt in eine Änderung des FRET-Signals übersetzt. Wir konnten diesen

Reporter in Nervenzellen exprimieren und FRET-Signale über zwei Stunden während einer pharmakologischen Blockade synaptischer Aktivität messen. Während der Blockade zeigten einige Zellen ein steigendes („Responder“), und andere ein abfallendes Reportersignal („Non-Responder“). Die meisten Kontrollzellen, deren synaptische Aktivität nicht blockiert wurde, verhielten sich jedoch allgemein ähnlich den „Responder“ Zellen, obwohl in Kontrollzellen keine RA-Synthese stattfinden sollte. Diese Ergebnisse sind wahrscheinlich nicht technisch bedingt, sondern womöglich auf eine mangelnde Sensitivität des aGEPRA FRET Sensors zurückzuführen, da er das Signal nicht zeitlich oder räumlich integrieren und folglich sehr niedrige RA-Konzentrationen nicht anzeigen kann.

Wir testeten zuletzt, in wieweit ratiometrische FRET-Messungen mit 2-Photonen-Mikroskopie erfasst werden können und stellen fest, dass quantitative Messungen für FRET-Paare mit hinreichender spektraler Separation ihrer 2-Photonen-Anregungsspektren möglich sind, wie wir anhand des Clover-mRuby2 FRET-Paares zeigen. FRET-Änderungen sind auch bei FRET-Paaren mit weniger deutlicher spektraler Auftrennung der Fluorophore zumindest qualitativ messbar, wie bei aGEPRA mit seinem CFP-YFP FRET-Paar; eine absolute Quantifizierung kann in solchen Fällen jedoch nur bei sorgfältiger Kalibrierung der Methode gelingen.

Wir ziehen den Schluss, dass nur integrierende Reporter eine hinreichende Sensitivität liefern, um niedrige RA-Konzentrationen während der HSP zu erfassen. Dem nicht-integrierenden aGEPRA FRET Sensor mangelt es hingegen an Sensitivität, um endogene RA-Produktion darzustellen, wie sie während der Blockierung synaptischer Aktivität in Nervenzellen aktiviert wird.

# 1. INTRODUCTION

Mammals are characterized by very dynamic and complex behavior resulting from the interplay between the animal's internal state and its environment. The brain is the organ that collects, processes, analyses, and integrates environmental cues and information about the internal state to initiate appropriate responses by adjusting behavior or internal body homeostasis. To fulfill this task, the brain has evolved to be the most complex and sophisticated of all organs, both structurally and functionally: instead of acting as a static processor for predefined arithmetical problems, it rather functions as a highly dynamic integrator that is continuously shaped by the flow of information it receives from its environment. The function of the brain is based upon the various neural networks comprised of electrically active neurons. These neurons are connected by numerous synapses, specialized structures that allow information to flow from one neuron to another. Through various biochemical processes, the strength and other properties of synapses can be modified based on the activity history of the network, thereby optimizing a network's capacity for information processing. This phenomenon is commonly referred to as synaptic plasticity, and it has become increasingly clear that deciphering its underlying molecular mechanisms is the first step toward understanding the complex function of the brain as a whole.

## 1.1 Neuronal Synaptic Plasticity

When synapses emerged as the major sites for neuronal signal transmission (Lopez-Munoz *et al.*, 2006), Donald Hebb proposed that they might also be plastic entities for information processing and memory storage (Seung, 2000). It has since been shown that synaptic plasticity is critically involved in various forms of brain function (Sweatt, 2016), including motor control (Pugh and Raman, 2009), sensory input computation (Singer *et al.*, 2009), learning and memory (Di Filippo *et al.*, 2009), and cognition. Forms of synaptic plasticity whereby activated synapses become strengthened have been termed HEBBian synaptic plasticity, even though the causal relationship between synaptic plasticity and brain function has yet to be formally demonstrated (Martin *et al.*, 2000, Takeuchi *et al.*,

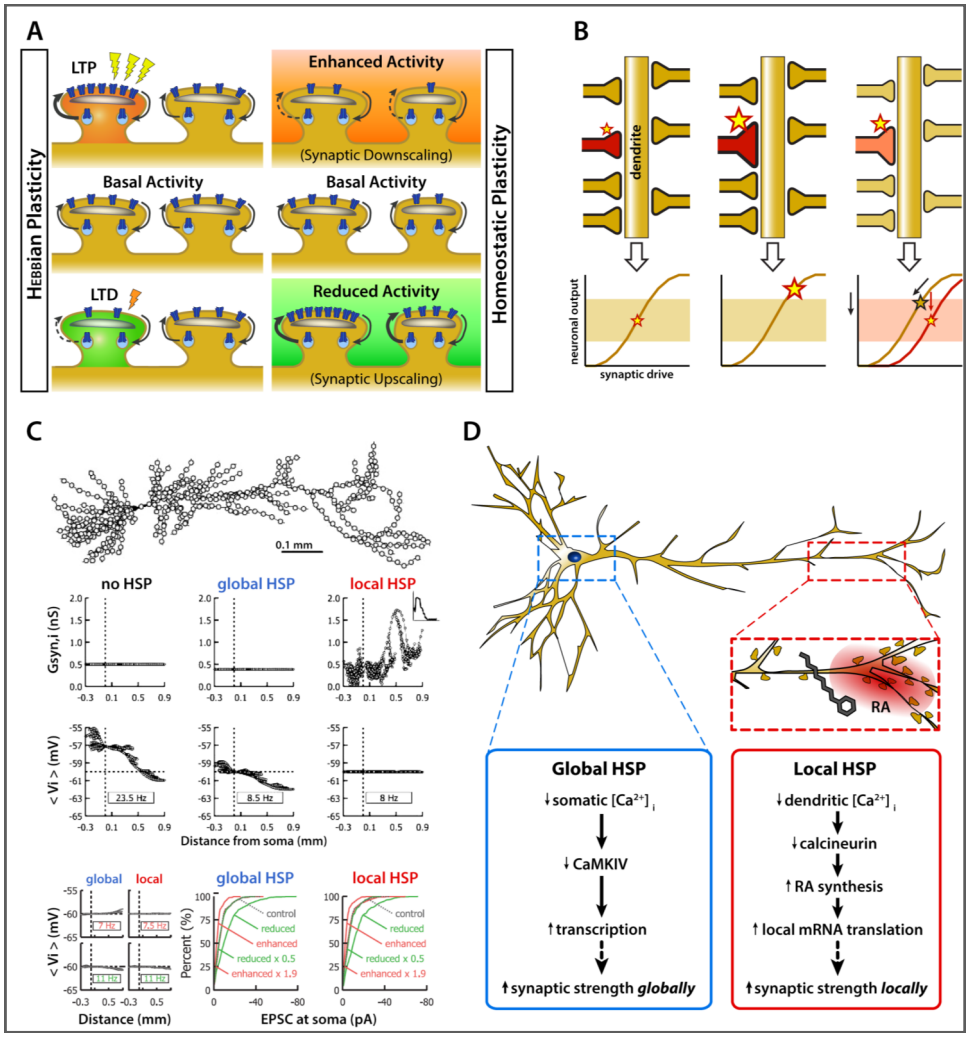


FIGURE 1.1| **Concepts of Neuronal Synaptic Plasticity. A**, *HEBBian and homeostatic synaptic plasticity*. A strongly activated synapse (illustrated by lightnings in left panel) is strengthened (LTP, top left panel) while moderate or weak synaptic activation leads to a weakening (LTD, bottom left panel) of only the activated synapse by a HEBBian mechanism. Homeostatic synaptic plasticity (HSP; right panels), by contrast, affects a large subset or possibly all synapses at once. Enhanced activity causes homeostatic synaptic downscaling (top right panel), while reduced activity leads to homeostatic synaptic upscaling (bottom right panel). (after Chater and Goda, 2014) **B**, *Necessity for HSP*. Strong activation of a given synapse (red synapse in left panel) induces HEBBian LTP. LTP may eventually cause overflowing synaptic input, saturating the postsynaptic neuron's dynamic range where it can meaningfully respond (middle panel, shaded area in input-response diagram). HSP can reduce overall input to restore set-point activity level (right panel) by multiplicatively re-adjusting the strengths of all synapses in two possible ways: in a pre-synaptic way, all synaptic inputs are scaled down to push the input level back into the dynamic range on the existing input-response curve (right panel, beige input-response curve). Alternatively, by scaling down postsynaptic receptor density a neuron may adjust its output level to the enhanced input, establishing a new input-response curve with a different dynamic range (right panel, red input-response curve). **C**, *Computational models of HSP*. Changes in synaptic properties of a model neuron (top panel) are computed according to global or local modes of HSP. Conductances Gsyn,i and voltages Vi of individual synapses are regulated differently by global or local HSP on a microscopic scale (middle panels), but such differences are concealed by ranked cumulative histogram plot analysis of miniature EPSCs (bottom panel). (modified from Rabinowitch and Segev, 2006b) **D**, *Cell biology of global and local HSP*. Both forms of HSP require a reduction of intracellular calcium levels, $[Ca^{2+}]_i$. Prolonged reduction of *somatic* calcium levels leads to the activation of a tran-

2014). Two forms of synaptic plasticity with mechanistically and functionally distinct characteristics can be distinguished (Yu and Goda, 2009) (Figure 1.1A): The aforementioned HEBBian mechanisms, often expressed as long-term potentiation and depression (LTP, LTD), act in an input-specific manner and only affect the subset of synapses that are activated (Figure 1.1A, left panel). HEBBian mechanisms therefore alter the properties of neuronal circuitry in response to specific inputs. By contrast, homeostatic mechanisms, such as synaptic scaling, regulate the synaptic strengths of most, possibly all, synapses converging onto one neuron (Turrigiano and Nelson, 2004). Homeostatic mechanisms are negative feedback-based processes aimed at maintaining a stable level of activity of the affected postsynaptic neuron even under variable overall input conditions (Feldman, 2009). These synaptic processes are collectively referred to as homeostatic synaptic plasticity (HSP) (Figure 1.1A, right panel).

HEBBian synaptic plasticity was first experimentally reported in the early 1970s in the hippocampi of rabbits, where long-term potentiation was observed after high-frequency electrical stimulation of the perforant path (Bliss and Lomo, 1973). Two decades later, long-term depression of hippocampal synapses was described after low-frequency electrical stimulation of the presynaptic cell (Dudek and Bear, 1992, Mulkey and Malenka, 1992). These observations laid the grounds to experimentally confirm Hebb's hypothesis that synaptic plasticity might be the structural and functional basis for memory formation in the central nervous system. However, a conceptual conflict soon became apparent from theoretical considerations (Bienenstock *et al.*, 1982) and computational models of HEBBian plasticity (Oja, 1982, Miller and MacKay, 1994): strengthening of highly active synapses by HEBBian mechanisms might cause overactivation of a neuron by saturating its physiological output level (Figure 1.1B, middle panel). Moreover, if the same mechanisms tend to weaken less active synapses, HEBBian plasticity would eventually lead to a

FIGURE 1.1| **Concepts of Neuronal Synaptic Plasticity.** (continued)

scription-dependent mechanism that restores normal firing rate by *globally* increasing the synaptic accumulation of heteromeric AMPA receptors (blue box). Reductions in *dendritic* calcium activate a biochemical cascade that increases local RA production, leading to the disinhibition of dendritic mRNA translation and *locally* increased synaptic insertion of homomeric AMPA receptors (red box). (after Chen *et al.*, 2014)

"winner-take-all" potentiation of the most active synapses, while all weaker synapses would vanish (Goldberg *et al.*, 2002). Because this contradicts our experience that memory is plastic and non-saturable, and because neuronal networks appear to be stable over extensive periods of time *in vivo* and *in vitro*, homeostatic mechanisms must exist to stabilize neuronal networks. Simply put, feed-forward neuronal network destabilization by HEBBian mechanisms requires a homeostatic, feedback-based means of neuronal network stabilization. The homeostatic feedback regulation of synaptic strength therefore counteracts the overall long-term activity changes of the network, i.e. increased network activity leads to a weakening of excitatory synapse strength, while suppressed network activity leads to excitatory synapse strengthening (Figure 1.1B, right panel). To avoid the immediate neutralization of HEBBian information storage, homeostatic feedback needs to operate at much longer time frames than HEBBian processes. While HEBBian plasticity is expressed within seconds to minutes after a stimulus, homeostatic feedback regulation occurs hours to days after prolonged network activity perturbation.

Homeostatic synaptic plasticity has indeed been observed experimentally after pharmacological activity perturbations of neuronal networks *in vitro*, either in dissociated neuronal cultures or in slice cultures (Turrigiano *et al.*, 1998, Wang *et al.*, 2011, Ju *et al.*, 2004, Sutton *et al.*, 2004, Sutton *et al.*, 2006, Thiagarajan *et al.*, 2005, Aoto *et al.*, 2008, Sarti *et al.*, 2013). Because bath application of neuronal activity-blocking drugs affects all cells and excitatory synapses of the neuronal networks alike, it leads to an overall increase in synaptic transmission. When miniature excitatory post-synaptic currents (mEPSCs) recorded from a pharmacologically silenced neuronal culture are ranked by amplitude and plotted against mEPSCs from an untreated control culture, the slope will be greater than one, while two control cultures plotted against each other yield a slope equal to one. It has therefore been suggested that homeostatic processes adjust the strengths of all synapses (or at least a large subset of synapses) multiplicatively, thereby keeping their relative strengths unchanged (Turrigiano *et al.*, 1998, Aoto *et al.*, 2008). Even though this multiplicative increase of synaptic strength was initially believed to be "global" across the

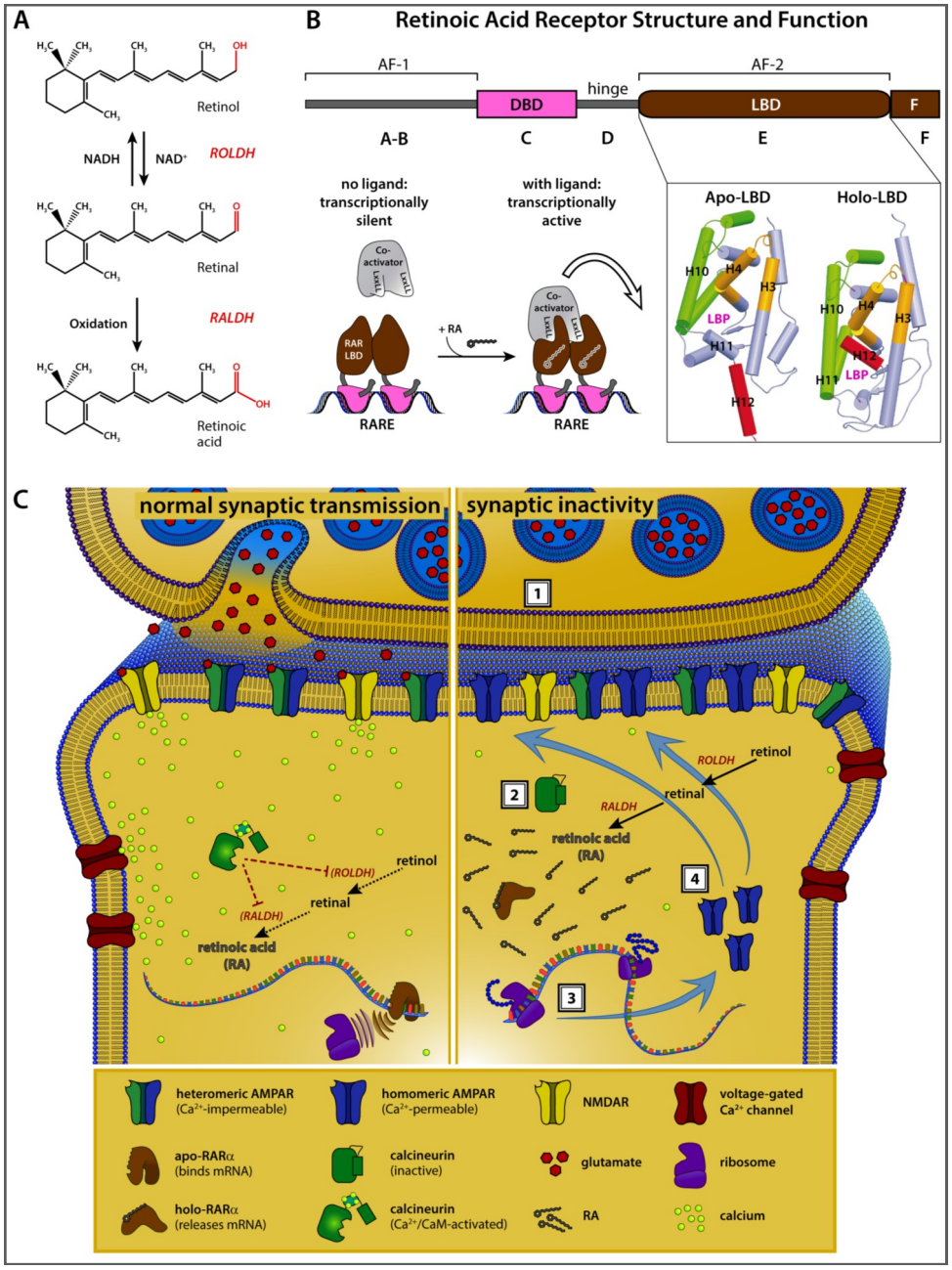


FIGURE 1.2| **RA Signaling during Homeostatic Synaptic Plasticity. A**, *Biochemistry of retinoids.* Retinoids are stored as retinyl esters which may be hydrolyzed to release free retinol when needed. It is then converted to retinal in a chemical equilibrium reaction catalyzed by ROLDHs. Retinal is irreversibly oxidized by RALDHs to yield retinoic acid. **B**, *Retinoic acid receptor structure and function.* Retinoid receptors contain 6 domains labeled A-F. The C domain is the DNA binding domain (DBD) and the E domain is the ligand binding domain (LBD), connected via a flexible hinge located in the D domain. The N-terminal ligand-independent activating function AF-1, and the ligand-dependent C-terminal AF-2 are indicated. Bottom right panel: The ligand-induced conformational switch of the LBD comprises outward rotation of helix 11 (H11) to form a linear extension of H10. H12 simultaneously flips inward over the ligand binding pocket (LBP) to form a hydrophobic groove with H3 and H4 into which transcriptional coactivators can bind (modified from Bourguet *et al.*, 2000a). Bottom left panel: Coactivators can interact with ligand-activated LBD by means of their consensus "NR box" binding motif (LxxLL), thereby stimulating RA-mediated transcription (white curved arrow) downstream of a "retinoic acid response element", RARE. **C**, *Molecular signaling cascade of RA-mediated homeostatic synaptic plasticity.* During normal synaptic activity, postsy-

these enzymes in the RA synthesis pathway blocks homeostatic synaptic plasticity (Aoto *et al.*, 2008).

RA is a small signaling molecule with a well-established role as a developmental morphogen (Maden, 2007), but it is also important in the adult brain to maintain normal function (Lane and Bailey, 2005). RA exerts its major biological functions by binding to its specific receptors, the retinoic acid receptors (RAR), which act in combination with retinoid X receptors (RXR). These two receptor classes are commonly referred to as retinoid receptors (Huang *et al.*, 2014). All retinoid receptors belong to the nuclear hormone receptor (NR) superfamily, and like other NRs they contain - among other domains - a DNA binding domain (DBD) for binding to specific DNA sequences called retinoic acid response elements (RARE), and a ligand binding domain (LBD) that binds their respective ligands (Brelivet *et al.*, 2012, Sever and Glass, 2013). Binding of RA to any of its receptors induces a canonical conformational switch of the unliganded apo-form to the ligand-activated holo-form of the LBD, comprising an outward rotation of helix 11 (H11) and back-folding of H12 over the ligand binding pocket of the LBD (Bourguet *et al.*, 1995, Renaud *et al.*, 1995, Wurtz *et al.*, 1996, Bourguet *et al.*, 2000a, Bourguet *et al.*, 2000b, Moras and Gronemeyer, 1998). This rearrangement of superficial helices creates a hydrophobic groove to which transcriptional coactivators can bind with a conserved "LxxLL" peptide sequence (where L represents leucin, and x represents any amino acid) termed "NR box", a consensus binding motif shared among all transcriptional coactivators of nuclear receptors (Heery *et al.*, 1997, Darimont *et al.*, 1998, Pogenberg *et al.*, 2005). The recruitment of transcriptional coactivators enhances retinoid receptor-mediated transcriptional activation of genes located downstream of the RARE (Huang *et al.*, 2014, Moutier *et al.*, 2012, Moras and Gronemeyer, 1998, Perissi and Rosenfeld,

FIGURE 1.2| **RA Signaling during Homeostatic Synaptic Plasticity.** (continued)

naptic calcium is maintained at a sufficient level for keeping calcineurin active (left panel). During synaptic inactivity (1), calcium concentration drops below a level required for calcineurin activation. Inactivated calcineurin leads to disinhibition of RA production (2), causing the dissociation of RARα from synaptic AMPA receptor mRNAs to allow their local translation (3). Newly synthesized homomeric AMPA receptors are incorporated into the postsynaptic membrane (4), increasing excitatory synaptic strength to restore normal synaptic input levels. (after Chen *et al.*, 2014 )

2005) (Figure 1.2B).

In contrast to its transcription-modulating activity, the recently discovered function of RA in synaptic plasticity and homeostasis is far less understood: RA and RARα have been identified as novel regulators of synaptic signaling and homeostatic synaptic plasticity that together regulate dendritic protein translation and synaptic insertion of the ionotropic glutamate receptor subunit GluA1 during chronic activity blockade (Aoto *et al.*, 2008, Poon and Chen, 2008) (Figure 1.2C). However, the precise intracellular signaling pathways leading to the production of RA, recruitment of RARα to synapses and eventually to the local translation of GluA1 and perhaps other mRNAs remain elusive (Groth and Tsien, 2008).

## 1.3 Calcineurin Signaling at the Synapse

After a "phosphodiesterase inhibitory protein" purified and cloned in 1978 was discovered to be expressed abundantly in brain tissue and regulated by calcium/calmodulin interactions, it was soon given the name "calcineurin" (CaN) (Klee and Krinks, 1978, Klee *et al.*, 1979). CaN is a protein serine/threonine phosphatase present in multiple neuronal compartments, including pre- and postsynaptic terminals, the cytosol, and the nucleus. It interacts with and acts upon a wide variety of target proteins and thereby influences a multitude of cellular processes such as neuronal morphology, neurotransmission, synaptic plasticity, and gene transcription (Groth *et al.*, 2003). At the synapse, CaN plays central roles in neurotransmitter and ion channel trafficking and function, structural protein network dynamics, and kinase/phosphatase balance regulation (Figure 1.3A). Many of CaN's rather acute and rapid effects on synaptic function involve the regulation of trafficking and ion permeability of neurotransmitter receptors and ion channels (Baumgartel and Mansuy, 2012). The most prominent example of CaN's direct influence on receptor abundance at the postsynaptic membrane is the dephosphorylation-dependent internalization of GluA1 subunit-containing glutamate receptors of the α-amino-3-hydroxy-5-methyl-4-isoxazole proprionate (AMPAR) type (Santos *et al.*, 2009). CaN-mediated dephosphory-

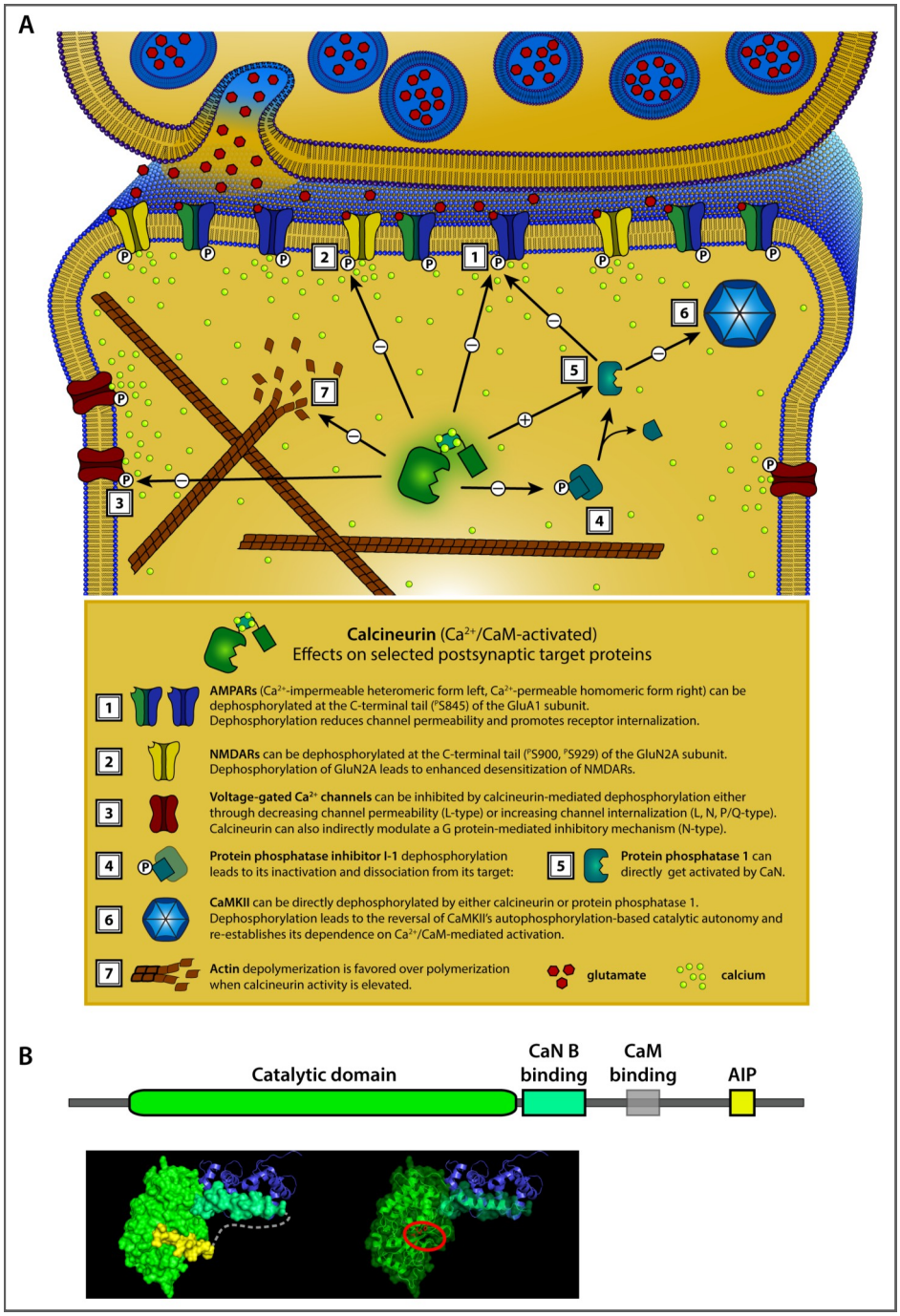


FIGURE 1.3| **Calcineurin Signaling at the Synapse. A**, *Postsynaptic targets of calcineurin signaling.* Calcineurin's major roles are the regulation of synaptic neurotransmitter receptor and ion channel homeostasis by dephosphorylating specific phosphosites (P). Another major function is the regulation of the synaptic cytoskeleton by depolymerizing actin filaments and destabilizing the post-synaptic density. For further details and references, see main text. **B**, *Calcineurin domain structure.* Calcineurin is a modular protein phosphatase with a catalytic Ser/Thr protein phosphatase domain homologous to other Ser/Thr protein phosphatases. A unique feature is calcineurin's regulatory domain which consists of three sub-domains: a calcineurin B binding domain (CaN B binding) to which the accessory calcineurin B subunit binds to complete the enzyme complex, a calmodulin binding domain (CaM binding) where $Ca^{2+}$/calmodulin can bind at sufficient calcium concentrations to activate calcineurin's enzymatic activity, and an autoinhibitory peptide (AIP) that occludes the catalytic cleft under resting conditions until $Ca^{2+}$/calmodulin binding causes the

entire neuron and therefore named "synaptic scaling" (Turrigiano *et al.*, 1998), computational modeling showed that a "local", dendrite-specific mechanism could yield similar experimental results (Rabinowitch and Segev, 2006a) (Figure 1.1C). One of the major open questions about homeostatic synaptic plasticity therefore is, how "global", or how "local" HSP truly is (Turrigiano, 2012, Chen *et al.*, 2014) (Figure 1.1D). And if it is a truly local event, then how is it locally confined, and how are the borders of its local confinement regulated and shifted by synaptic activity levels?

Many forms of synaptic plasticity, both HEBBian and homeostatic mechanisms alike, are mediated by neurotransmitter receptor regulation in the postsynaptic membrane. A change in synaptic activity leads to the activation of biochemical signaling cascades that affect postsynaptic neurotransmitter receptor activity at various levels, including gene transcription, local (dendritic) mRNA translation, receptor insertion into the membrane from intracellular reserve pools, lateral diffusion in and out of the active zone of the synapse, or modulation of ion permeability by means of phosphorylation or other post-translational modifications of the receptor molecules (Lee and Kirkwood, 2011). Because HEBBian and homeostatic mechanisms seem to share at least some signaling cascades involved in postsynaptic neurotransmitter receptor regulation, but affect synaptic sensitivity in opposite directions, it will be interesting to determine how and where the signaling cascades diverge between the two opposing mechanisms (Kotaleski and Blackwell, 2010).

## 1.2 Retinoic Acid Signaling and Homeostatic Synaptic Plasticity

As a membrane-permeable lipophilic signaling molecule, all-*trans* retinoic acid (RA) is produced *ad hoc* whenever necessary because it cannot be stored in its active form. Retinoid precursors can be stored intracellularly as retinyl esters, which can hydrolytically release all-*trans* retinol when RA is needed. The biosynthetic pathway of RA production involves a two-step oxidative reaction; all-*trans* retinol is first converted into all-*trans* retinal by retinol dehydrogenases (ROLDHs) in a reversible equilibrium redox reaction. Retinal then becomes irreversibly oxidized by retinaldehyde dehydrogenases (RALDHs) to yield RA (Napoli, 1996) (Figure 1.2A). It has been shown that blocking either one of

lation of GluA1 after weak synaptic stimulation and moderate calcium entry leads to rapid but prolonged AMPAR internalization (Beattie *et al.*, 2000, Man *et al.*, 2007), which is considered the molecular basis for synaptic long-term depression (LTD) (Mulkey *et al.*, 1993, Mulkey *et al.*, 1994, Kessels and Malinow, 2009, Santos *et al.*, 2009). Another important group of glutamatergic neurotransmitter receptors are the N-methyl-D-aspartate type glutamate receptors (NMDAR). The C-terminal tail of the GluN2A subunit of NMDARs can be dephosphorylated by CaN, leading to decreased channel open probability and increased receptor desensitization (Lieberman and Mody, 1994, Tong *et al.*, 1995, Krupp *et al.*, 2002). Beyond its effects on glutamatergic neurotransmitter receptors, CaN-mediated dephosphorylation also affects voltage-gated calcium channels (Budde *et al.*, 2002), leading to receptor inactivation (Lukyanetz *et al.*, 1998, Burley and Sihra, 2000, Dittmer *et al.*, 2014) and internalization (Wu *et al.*, 2005). In complete analogy to the modulation of glutamatergic synapse function, CaN can also regulate inhibitory synaptic transmission (Jones and Westbrook, 1997, Robello *et al.*, 1997) by direct dephosphorylation of the γ2 subunit of A-type γ-amino-butyric acid receptors ($GABA_AR$) (Wang *et al.*, 2003, Luscher *et al.*, 2011), and thereby decrease GABAergic neurotransmission (Chen *et al.*, 1995, Jones and Westbrook, 1997, Robello *et al.*, 1997, Wang *et al.*, 2003).

The modulation of synaptic neurotransmitter and ion channel abundance and function requires active regulation of protein trafficking and motility. Consequently, the regulation of cytoskeletal and structural protein dynamics constitutes a second important aspect of synaptic CaN function. Consistent with increased dynamics and internalization of synaptic receptors and ion channels, CaN activation leads to the depolymerization of filamentous actin (F-actin) to its monomeric form, globular actin (G-actin) (Gomez *et al.*, 2002, Morishita *et al.*, 2005). Through its effects on synaptic actin dynamics, CaN also influences the composition of the complex structural protein network that forms the postsynaptic

FIGURE 1.3| **Calcineurin Signaling at the Synapse.** (continued)

displacement of the AIP from the catalytic domain to allow catalysis to occur. Top panel schematically illustrates domain structure, bottom panel shows space-filling atomic model with domains color-coded as in top panel. Accessory CaN B domain is represented as ribbon model in purple, and catalytic cleft is encircled in red in the space-filling model without the AIP on the right (PDB: 1AUI).

density (PSD). CaN itself is integrated into the PSD (Husi *et al.*, 2000) by binding to A-kinase anchoring protein (AKAP79/150) (Dell'Acqua *et al.*, 2002), an important signaling complex organizer within the PSD that also recruits protein kinases A and C (PKA and PKC) (Coghlan *et al.*, 1995, Klauck *et al.*, 1996, Oliveria *et al.*, 2003). AKAP79/150 is in turn associated with F-actin, whose depolymerization leads to the dissipation of AKAP79/150 complexes (Gomez *et al.*, 2002). Furthermore, AKAP79/150 can bind other PSD members of the membrane-associated guanylate kinase (MAGUK) superfamily, linking the AKAP79/150 complex to postsynaptic glutamate receptors (Colledge *et al.*, 2000, Oliveria *et al.*, 2003). These large signaling complexes assembled around AKAP79/150 become either partially disassembled or functionally inhibited by dissociation of AKAP79/150 from the actin cytoskeleton and its migration away from the PSD, leading to a depression of glutamatergic synaptic transmission (Tavalin *et al.*, 2002).

The third - and perhaps most complex - of CaN's synaptic functions is its coordinating role in balancing protein kinase and phosphatase activities (Woolfrey and Dell'Acqua, 2015). Many synaptic protein kinases and phosphatases are themselves subject to phosphorylation, and their phosphorylation states can regulate enzymatic activity and/or localization. CaN's most direct action within the postsynaptic protein kinase/phosphatase network is the dephosphorylation of the protein phosphatase inhibitor I-1, which leads to the dissociation from its target, protein phosphatase 1 (PP1), rendering PP1 catalytically active (Mulkey *et al.*, 1994). CaN and PP1 share many downstream targets, and their combined activities can shift synaptic protein kinase/phosphatase balance towards a phosphatase-dominated state. They can together decrease local PKA and PKC activities within the PSD by removal of the PKA and PKC-recruiting scaffold AKAP79/150 (Oliveria *et al.*, 2003, Colledge *et al.*, 2000, Tavalin *et al.*, 2002), but they also dephosphorylate $Ca^{2+}$/calmodulin-dependent protein kinase II (CaMKII) to eliminate its autophosphorylation-induced catalytic "autonomy" (Miller and Kennedy, 1986) and restore its catalytic dependence on the activation by $Ca^{2+}$/calmodulin (Strack *et al.*, 1997).

At the behavioral level, pharmacological and genetic studies suggest important functi-

ons of CaN in memory formation, consolidation, and/or extinction (Mansuy *et al.*, 1998a, Mansuy *et al.*, 1998b, Winder *et al.*, 1998, Ikegami and Inokuchi, 2000, Malleret *et al.*, 2001, Zeng *et al.*, 2001). Especially CaN's prominent role in slow phases of memory such as memory consolidation and extinction, its regulation by calcium levels, and its promiscuous interactions with a large number of substrates during synaptic plasticity, make it a potential regulator of homeostatic plasticity that is believed to act on a similarly slow time scale.

Structurally, calcineurin is composed of two obligatory subunits, one larger catalytic calcineurin A subunit (CnA) and the smaller accessory calcineurin B subunit (CnB). The catalytic subunit consists of a catalytic domain with structural homology to other protein serine/threonine phosphatases, and additional regulatory domains that confer calcineurin's calcium responsiveness (Figure 1.3B): a calcineurin B binding helix (BBH) where the accessory CnB subunit binds, followed by an autoinhibitory domain (AID) comprising a calmodulin binding domain (CaMB) to which $Ca^{2+}$/calmodulin can bind, and an autoinhibitory peptide (AIP) close to the C-terminal. Under resting conditions, the AIP occludes the catalytic cleft, thereby inhibiting substrate access. When intracellular calcium levels rise, activated $Ca^{2+}$/calmodulin can bind to the CaMB region in close proximity to the AIP, inducing a conformational change that leads to the displacement of the AIP and opening of the catalytic cleft, rendering CaN catalytically active (Rusnak and Mertz, 2000). Moreover, the very N-terminal and C-terminal portions of the protein are, respectively, formed by N-terminal, and C-terminal domains of unknown function that display high sequence variation across species or between different CaN isoforms within a single species.

## 1.4 Cell-based Bioreporter Assays for Biomolecules

Insight into the internal metabolic state of an organism and its cells is indispensible to answer many questions in biology. Classical biochemical methods require lysing or fixing the tissues or cells of interest and are therefore limited to static, "snapshot-like" images of

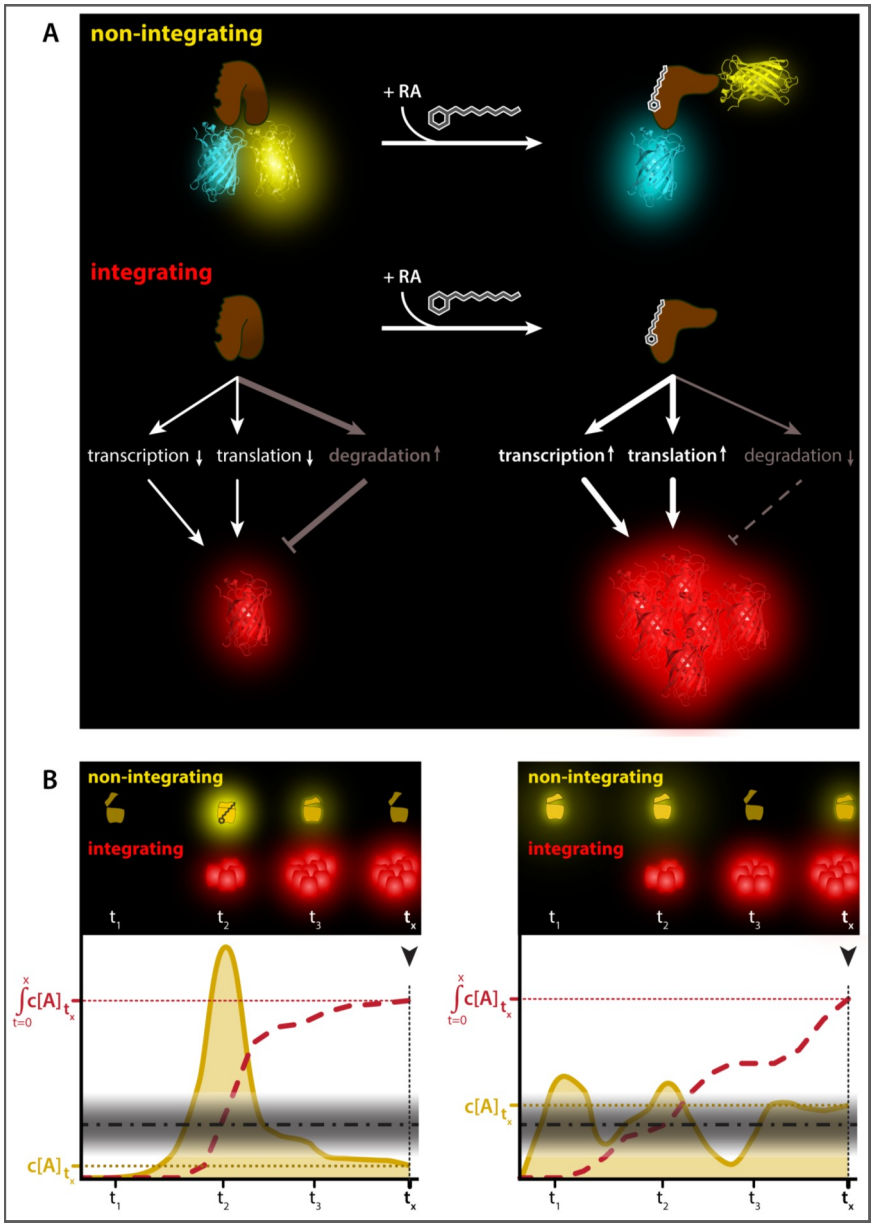


FIGURE 1.4| **Cell-Based Bioreporter Assays. A**, *Conceptual comparison of non-integrating and integrating reporter assays. Non-integrating* reporters combine sensor and reporter activities in a single protein. Therefore, sensor activity directly translates into reporter activity proportionally and with high spatial (subcellular) and temporal (sub-second) resolution. Non-integrating reporters are often based on naturally occurring "receptor" proteins fused to one or two fluorescent proteins. Binding of their specific ligand induces a conformational change which translates into a change of fluorescence properties. We refer to these reporters as non-integrating systems because reporter activity is strictly confined in time and space to the actual presence of analyte. *Integrating* reporter assays, by contrast, consist of a sensor protein that can modulate the transcription or translation (or in rare cases the degradation) of a separate reporter, commonly a gene encoding for a fluorescent or luminiscent protein. The sensor protein regulates reporter protein abundance without directly affecting activities of individual reporter protein. A transient sensor activation during the total assay time is often sufficient for detectable reporter accumulation. Because reporter proteins may remain stable well beyond sensor activation, they can accumulate in the target cell even with low or fluctuating sensor activity; we therefore refer to such reporters as integrating systems. **B**, *Time courses of non-integrating and integrating reporters.* Non-integrating reporters (yellow) reliably detect intense signals

the biochemical state of the system. After lysis or fixation, a cell or tissue sample is irreversibly destroyed and can therefore not be reprobed at a later time point or under different conditions. By contrast, physiological techniques make a living cell or tissue accessible for measurements of parameters of its changing internal states while experimental manipulations are made, but are often invasive and the measurements themselves may interfere with the parameters to be measured.

A growing number of cell-based reporter assays have therefore been developed where genetically encoded sensor molecules expressed in the cells and tissues of interest are utilized to overcome the limitations of classical biochemical or physiological techniques. Such genetically encoded sensor molecules can sense the metabolic state or a particular analyte's concentration and dynamics; sensor activation by the analyte can subsequently be translated into a reporter activity which should ideally be detectable by non-invasive methods, most commonly by fluorescence or luminescence readouts (Umezawa, 2005, Wang *et al.*, 2009, Michelini *et al.*, 2010).

Two general types of reporters may be distinguished: transcription-based reporters and transcription-independent, folding-based reporters (Figure 1.4). Transcription-based reporters make use of a sensor molecule that allows to couple a biological parameter to the expression level of a reporter gene whose product may accumulate within the cell. Therefore, reporters of this type may be considered as integrating reporters. Because transcription is necessary for reporter function, such reporters are limited to the speed of transcription (hours) and spatial resolution is confined to the whole-cell level without subcellular precision. Folding-based reporters, by contrast, are present in the cell independently of the examined biological parameter or analyte. In the presence of the analyte, such reporters

FIGURE 1.4| **Cell-Based Bioreporter Assays.** (continued)

(timepoint $t_2$ in the left panel) but may fail to detect low signals if analyte concentrations fluctuate at low levels around detection threshold of the assay (right panel, detection thresholds illustrated as gray shaded areas in the bottom diagrams). An integrating assay (red dashed line) has the advantage of steadily building up reporter signal during the time course of the assay, but endpoint assay readout (black arrowhead at timepoint $t_x$) obscures the fluctuation of analyte concentration over time. Therefore, a short burst of analyte (left panel) may yield a similar integrated assay signal as an analyte concentration moderately increased over background for an extended time period (right panel).

will undergo a conformational switch that allows the specific detection of signaling events in real-time (sub-second response time) and with subcellular resolution without signal integration over space and time (non-integrating reporters).

## 1.5 FÖRSTER Resonance Energy Transfer

Fluorescence is a phenomenon whereby a light-absorbing molecule (the fluorophore) can be excited by light of a specific wavelength to emit light of a longer wavelength (Figure 1.5A, left panel). In terms of quantum physics, a fluorophore that absorbs a photon of a specific energy is lifted to an electronic excited state (photoexcitation). Because the excited state is unstable, the fluorophore will spontaneously return to its ground state by releasing a photon with less energy than the excitation photon (photoemission). The energy difference between the absorbed and the emitted photon is reflected as a red shift of the emitted light with respect to the absorbed light (STOKES shift). These processes are schematized as JABŁOŃSKI diagrams to illustrate the allowed electronic states of the fluorophore and its energy transitions associated with photon absorption and emission (Jablonski, 1933).

Theodor Förster first mathematically described a radiation-free energy transfer from an excited fluorophore, the fluorescence donor, to an adjacent fluorophore, the fluorescence acceptor (Förster, 1948) (Figure 1.5A, middle panel). As the energy transfer occurs by means of electromagnetic resonance of the interacting chromophores' electronic dipoles, no photon is emitted during the process. The commonly used term "fluorescence resonance energy transfer" is therefore misleading, and FÖRSTER resonance energy transfer (FRET) should be used instead. Förster's formula shows that the efficiency of resonance energy transfer (FRET efficiency) decays with the sixths power of the distance between the two fluorophores, leading to a steep decay of FRET efficiency around a so-called FÖRSTER radius, $R_0$, where FRET efficiency equals 50% (Figure 1.5C). The FÖRSTER radius of a FRET pair depends on the overlap integral between the donor emission and the acceptor excitation spectra, the donor fluorescence lifetime, as well as the refractive index

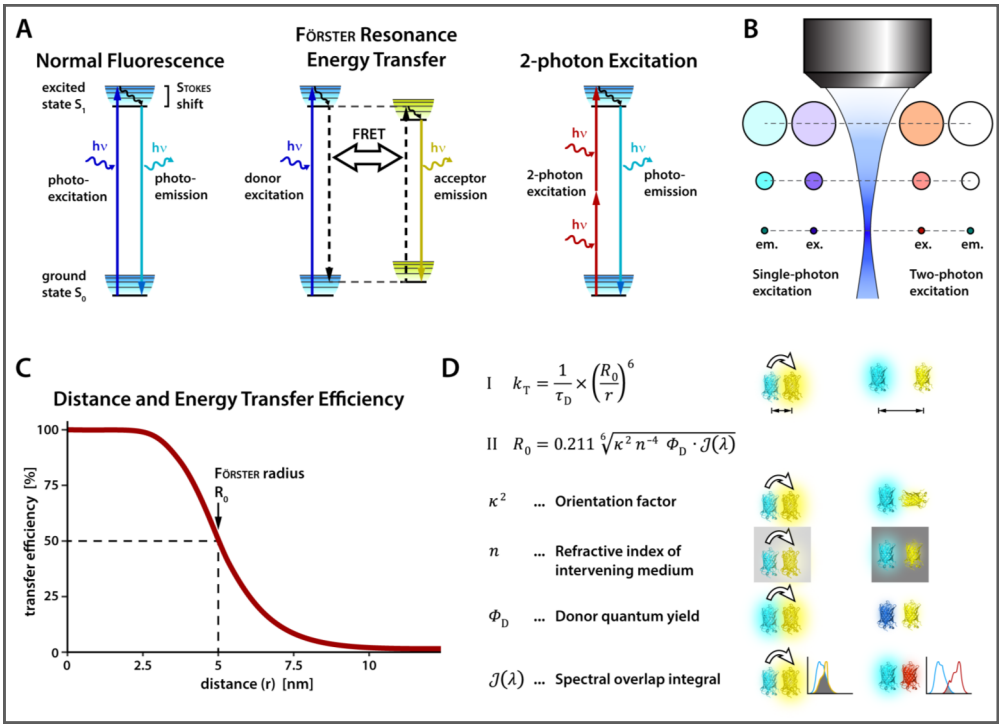


FIGURE 1.5| **Basic Concepts in Fluorescence Microscopy and FRET. A**, *JABLONSKI diagrams illustrating different modes of fluorescence.* A fluorophore can assume different electronic energy states, illustrated as horizontal lines in the JABLONSKI diagram. Left panel: During normal fluorescence, a photon of appropriate energy (dark blue wavy arrow) is absorbed by a fluorophore, lifting it from the ground state $S_0$ to its first excited state $S_1$ (straight dark blue upward arrow). Some energy gets lost by vibrational relaxation (black wavy arrow) before a photon is emitted for final relaxation (straight light blue downward arrow). The emitted photon has less energy than the absorbed photon (STOKES shift). Middle panel: During FÖRSTER resonance energy transfer, an excited donor fluorophore (light blue diagram) may relax by passing its energy on to an adjacent acceptor fluorophore (yellow diagram) by means of radiationless electronic dipole coupling (FRET). The FRET acceptor fluorophore becomes excited by the energy transfer and relaxes through vibrational relaxation and emission of a photon. Right panel: 2-photon excitation is the process of exciting a fluorophore by the almost concomitant absorption of two photons which together provide the energy for full excitation of the fluorophore. Relaxation occurs by normal vibrational relaxation and photoemission. **B**, *Comparison of single-photon and two-photon excitation modes.* A focused laser beam has the highest photon density for excitation (ex.) at its focal point, declining away from the focal point as the beam diameter increases. Emission (em.) is directly proportional to excitation photon intensity in single-photon excitation mode but in two-photon excitation mode it is evoked at the focal point only because of the quadratic relation between excitation and emission. (after Cahalan *et al.*, 2002) **C**, *Distance dependency of FRET.* FRET efficiency drops with the sixths power of the distance ($r$) between the donor and acceptor fluorophores. The FÖRSTER radius of 5 nm defines the distance of half-maximal FRET efficiency between a hypothetical FRET pair. **D**, *Mathematical description and pictorial illustrations of FRET parameters.* The FRET transfer rate $k_T$ expressed by equation I depends on the donor fluorescence lifetime $\tau_D$, the FÖRSTER radius $R_0$, and the 6th power of the distance $r$ between the two interacting fluorophores. Equation II describes dependence of $R_0$ on the orientation factor, refractive index of intervening medium, donor quantum yield, and the spectral overlap between the two interacting fluorophores. Picture diagrams illustrate high (left diagram; white curved arrows represent FRET) *vs.* low FRET conditions (right diagram): short *vs.* long distance between fluorophores, parallel *vs.* perpendicular orientation, low *vs.* high intervening refractive indices, high *vs.* low donor quantum yields, and large *vs.* little spectral overlaps between donor emission and acceptor excitation.

of the surrounding medium (Figure 1.5D). For most biologically relevant fluorophore pairs, including fluorescent proteins and many synthetic dyes, with excitation and emission spectra in the visible range, FÖRSTER distances approximate 5 nm in aqueous solution. These FRET pairs are ideally suited for the design of chimeric sensors where fluorescent tags are attached to a protein of interest such that conformational changes of the protein of interest become amenable to measurements of FRET changes between the fluorescent tags (Campbell, 2009).

## 1.6 Two-Photon Excitation Microscopy

Based on Maria Göppert-Mayer's theoretical concept of two-photon absorption (Göppert-Mayer, 1931), Winfried Denk and colleagues pioneered two-photon excitation laser scanning microscopy to observe biological samples (Denk *et al.*, 1990). Two-photon absorption, in contrast to traditional fluorescence as described above, is a process whereby the fluorophore becomes excited by the almost simultaneous absorption of two photons, which each provide half the required energy for its excitation (Figure 1.5A, right panel). Therefore, the two-photon excitation wavelength is approximately twice the conventional (single-photon) excitation wavelength; for typical fluorophores that emit in the green and red spectral range, conventional fluorescence microscopy requires excitation in the blue and green spectral range, while two-photon excitation microscopy usually requires excitation in the far-red or infrared spectral range. The incidence of two photons within a very brief amount of time (~$10^{-16}$ s) to excite the fluorophore requires very high light intensities which can be achieved by pulsed lasers that release very short high-energetic laser pulses (~100 femtoseconds long) at high frequencies (around 80 MHz). The probability of two photons impinging on a fluorophore molecule within the brief time span required for successful excitation is proportional to the squared light intensity (laser power per area, or the number of photons passing a unit area per unit of time). Because the power of a laser beam remains constant throughout its light path, the light intensity grows with decreasing cross-section, reaching its maximum at the focus of a focused laser beam. Sufficient laser intensity to excite a fluorophore by two-photon absorption is thus

only reached within a volume extending ~0.3 µm radially and ~0.9 µm axially around the focal spot of a microscope objective, practically eliminating out-of-focus excitation (Figure 1.5B). The red-shifted excitation laser wavelength also allows deeper tissue penetration with less scattering compared to conventional (single-photon) fluorescence microscopy (So, 2001, Cahalan *et al.*, 2002, Zipfel *et al.*, 2003).

## 1.7 Aim of This Work

Previous work from our lab established that RA is critically involved in the biochemical signaling cascade underlying homeostatic synaptic plasticity, but the precise time course and location of intracellular RA signaling, as well as its relevance *in vivo* are far less understood. The objective of this work was to test transcription- or FRET-based bioreporter methods for their compatibility with (1) long-term expression, making them suitable for *in vivo* applications, and (2) spatiotemporally resolved RA detection, making them useful to determine subcellular compartments of RA synthesis during homeostatic synaptic plasticity. To this end we explored existing methods and developed novel approaches which would allow us to address these important open questions in future experiments.

# 2. MATERIALS AND METHODS

## 2.1 Materials, Consumables and Reagents

TABLE 2.1| **Materials, Consumables and Reagents.** Tissue culture consumables categorized by cell type. Chemicals listed in alphabetical order.

| **Hippocampal Rat Neuron Culture Consumables** | | | |
|---|---|---|---|
| Reagent | | Supplier | Catalog # |
| Neurobasal Medium | (NB) | Gibco | *21103* |
| Neurobasal Medium, phenol red-free | | Gibco | *12348* |
| Fetal bovine serum, Optima | (FCS) | Atlanta Biological | *S12450* |
| B-27 media supplement | (B-27) | Invitrogen | *17504044* |
| GlutaMAX™ | (GlutaMAX) | Gibco | *35050* |
| Cytosine β-D-arabinofuranoside hydrochloride | (Ara-C) | Sigma | *C6645* |
| Minimum Essential Medium + Earle's Salts | (MEM) | Gibco | *11090* |
| Hank's Balanced Salt Solution | (HBSS) | Gibco | *14170* |
| Poly-L lysine | (PLL) | Sigma | *P2636-500MG* |
| Trypsin | | Sigma | *T1005* |
| HEPES | | Gibco | *15630-080* |
| 24-well tissue culture dishes | | Falcon | *353047* |
| Cover glasses, 12 mm, thickness 0.09-0.12 mm | (CS) | Carolina | *633009* |
| **HEK and HEK 293T Cell Culture Consumables** | | | |
| Reagent | | Supplier | Catalog # |
| Dulbecco's Modified Essential Medium | (DMEM) | Gibco | *11965* |
| Fetal bovine serum, Optima | (FCS) | Atlanta Biological | *S12450* |
| Tissue culture dishes, 100 mm | | Falcon | *353003* |
| 24-well tissue culture dishes | | Sarstedt (TPP) | *92424* |
| Microscope cover glasses No. 1, 13 mm | (CS) | Marienstedt GmbH | *01 115 30* |
| Gelatin from porcine skin, type A | (Gelatin) | Sigma | *G1890-100G* |
| Trypsin/EDTA Solution (10x) | (Trypsin) | Millipore | *L2153* |
| **Chemicals, Reagents and Drugs** | | | |
| Reagent | Chem. Formula | Supplier | Catalog # |
| Agar | | Sigma | *A1296-1KG* |
| Agarose | $C_{24}H_{38}O_{19}$ | Lonza | *50005* |
| Aldi-6 | | Mochli-Rosen Lab | |
| Ampicillin (anhydrous) | | Sigma | *A9393-5G* |
| Boric acid | $H_3BO_3$ | Merck/Millipore | *1001650500* |
| Calcium chloride (anhydrous) | $CaCl_2$ | Merck/Millipore | *1023782500* |
| CNQX | $C_9H_4N_4O_4$ | Tocris | *0190* |
| 4-Diethylaminobenzaldehyde (DEAB) | $(C_2H_5)_2NC_6H_4CHO$ | Sigma | *D86256* |
| DABCO | $C_6H_{12}N_2$ | Sigma | *D27802-25G* |
| Dimethyl sulfoxide (DMSO) | $(CH_3)_2SO$ | Sigma | *276855-250ML* |
| Disodium hydrogen phosphate heptahydrate | $Na_2HPO_4$*7 $H_2O$ | Merck/Millipore | *1065751000* |
| Disodium tetraborate decahydrate | $Na_2B_4O_7$*10 $H_2O$ | Merck/Millipore | *1063081000* |
| FK506 | | Tocris | *3631* |
| FK1012 | | Graeff Lab | |

TABLE 2.1| **Materials, Consumables and Reagents (continued)**

| **Chemicals, Reagents and Drugs (continued)** | | | |
|---|---|---|---|
| Reagent | Chem. Formula | Supplier | Catalog # |
| Fluoromount G® | | Southern Biotech | *0100-01* |
| D(+)-Glucose-monohydrate | $C_6H_{12}O_6*H_2O$ | Merck/Millipore | *40740500* |
| Glycerol | $C_3H_8O_3$ | Merck/Millipore | *1040931000* |
| HEPES | $C_8H_{18}N_2O_4S$ | Sigma | *H3375-1KG* |
| Hydrochloric acid, 37% (fuming) | HCl | Sigma | *H1758-500ML* |
| Kanamycin sulfate | | Sigma | *B5264-250MG* |
| LB broth base powder | | Invitrogen | *12780-029* |
| Lipofectamine® 2000 | | Invitrogen | *11668-019* |
| Magnesium sulfate heptahydrate | $MgSO_4*7\ H_2O$ | Merck/Millipore | *1058860500* |
| Mowiol 4-88 | | Fluka | *81381* |
| Paraformaldehyde (PFA) | $(CH_2O)_n$ | Merck/Millipore | *1040051000* |
| Potassium chloride | KCl | Calbiochem | *529552-250GM* |
| Potassium dihydrogen phosphate | $KH_2PO_4$ | Merck/Millipore | *1048731000* |
| all-*trans* Retinoic acid | $C_{20}H_{28}O_2$ | Sigma | *R2625* |
| Sodium bicarbonate | $NaHCO_3$ | Merck/Millipore | *1063920500* |
| Sodium chloride | NaCl | Merck/Millipore | *1370175000* |
| Sodium dihydrogen phosphate monohydrate | $NaH_2PO_4*H_2O$ | Merck/Millipore | *1063491000* |
| Sodium hydroxide (pellets) | NaOH | Sigma | *795429-1KG-D* |
| Tetrodotoxin citrate (TTX) | | Abcam | *ab120055* |
| Tris Base | $C_4H_{11}NO_3$ | Pharma Biotech | *17-1321-01* |

## 2.2 Cell Culture Media and Solutions

TABLE 2.2| **Cell Culture Media Compositions**

| Cell Culture Media | | Media Compositions and Additives |
|---|---|---|
| High Glucose MEM | | 200 mL MEM<br>+ 51 g glucose |
| Serum Neuron Media | (SNM) | 500 mL MEM<br>+ 8 mL High Glucose MEM<br>+ 5 mL GlutaMAX™<br>+ 27.5 mL FCS<br>+ 1:40 B-27 |
| Neurobasal Growth Media | (NGM) | NB<br>+ 1:50 B-27<br>+ 1:400 GlutaMAX™ |
| HEK Cell Media | | DMEM<br>+ 10% FCS |

TABLE 2.3| **Compositions of Solutions Used in This Study**

| Solution | Composition (all reagents dissolved in $H_2O$ unless otherwise specified) |
|---|---|
| Borate buffer | 50 mM $H_3BO_3$, 12.5 mM $Na_2B_4O_7$*10 $H_2O$ |
| PLL for coating | 0.5 mg/mL PLL in borate buffer |
| Gelatin for coating | 0.5 g/L gelatin in $H_2O$ |
| 2x HEPES buffer | 1.4 mM $Na_2HPO_4$*7 $H_2O$, 140 mM NaCl, 50 mM HEPES, pH 7.05 |
| 2.5 M calcium chloride | 2.5 M $CaCl_2$ |
| 1 M calcium chloride | 1 M $CaCl_2$ |
| 10x PBS | 1.37 M NaCl, 27 mM KCl, 100 mM $Na_2HPO_4$*7 $H_2O$, 28 mM $KH_2PO_4$ |
| 1x PBS | 137 mM NaCl, 2.7 mM KCl, 10 mM $Na_2HPO_4$*7 $H_2O$, 2.8 mM $KH_2PO_4$ |
| 0.5x PBS | 68.5 mM NaCl, 1.35 mM KCl, 5 mM $Na_2HPO_4$*7 $H_2O$, 1.4 mM $KH_2PO_4$ |
| 2p-Imaging solution | 100 mM NaCl, 2.5 mM KCl, 1.3 mM $MgSO_4$*7 $H_2O$, 1 mM $NaH_2PO_4$*$H_2O$, 26.2 mM $NaHCO_3$, 110 mM glucose, 2.5 mM $CaCl_2$ |
| PFA fixation medium | 4% PFA (w/v) in PBS |
| Mowiol mounting medium | 6 g glycerol, 2.4 g Mowiol, 6 mL $H_2O$, 12 mL Tris (200 mM, pH 8.5), 2.5% (w/v) DABCO |

## 2.3 Drugs

TABLE 2.4| **Concentrations of Drugs Used in This Study**

| Drugs | Drug stocks | Final concentrations |
|---|---|---|
| Aldi-6 | 1 mM in DMSO | 1 µM in cell culture media |
| Ara-C | 4 mM in $H_2O$ | 4 µM in cell culture media |
| CNQX | 50 mM in DMSO | 5 µM in cell culture media |
| DEAB | 10 mM in DMSO | 10 µM in cell culture media |
| FK506 | 50 mM in DMSO | 5 µM in cell culture media |
| FK1012 | 45 µM in ethanol | 100 nM in cell culture media |
| RA | 10 mM in DMSO | 1 µM in cell culture media |
| TTX | 1 mM in $H_2O$ | 1 µM in cell culture media |
| Ampicillin | 100 mg/mL in $H_2O$ | 100 µg/mL in LB broth or LB agar |
| Kanamycin | 50 mg/mL in $H_2O$ | 50 µg/mL in LB broth or LB agar |

## 2.4 Methods

### 2.4.1 Dissociated Rat Hippocampal Neuron Culture

E22 rat embryos were collected by Caesarian section (after $CO_2$ anaesthesia and cervical dislocation of the mother, in accordance with Stanford Administrative Panel on Laboratory Animal Care) of timed-pregnant Sprague Dawley rats (Charles River Laboratories). Brains from embryos were collected in PETRI dishes containing pre-warmed and equilibrated high glucose HBSS in which hippocampi were dissected out. Hippocampal neurons were dissociated by trituration following trypsin digestion (19 min. at 37°C) and were then plated on PLL-coated coverslips in 24-well plates at 1x $10^5$ cells per well. Dissociated hippocampal cells were seeded in serum neuronal media (SNM), and at 1 day *in vitro* (DIV 1), 70% of SNM were replaced with neurobasal growth media (NGM). From DIV 7 on, 50% media changes were performed at 7-day intervals with fresh NGM, and AraC was maintained at 4 µM final concentration to inhibit proliferation of glia and dentate gyrus granule cells.

### 2.4.2 RARE-TK::EGFP Reporter Assay in Neurons

Neurons grown on coverslips as described above were transfected between DIV 10 and 13 with 0.8 µg of the RARE-TK::EGFP reporter plasmid per well using the lipofectamine™ 2000 method. Before transfection, 510 µL of neuron culture media were removed and stored at 37°C. For transfection, 0.8 µg of DNA and 0.5 µL of lipofectamine per well were dissolved separately into 25 µL of OptiMEM media each and incubated at ambient temperature for 5 min. Contents of DNA- and lipofectamine-containing tubes were then combined and mixed well, incubated at room temperature for another 20 min. before 50 µL of the mixture were added into the remaining 490 µL per well of the neuron culture. After an incubation period of 2 hours at 37°C and 5% $CO_2$, transfection media were aspirated and replaced with 500 µL of pre-conditioned media per well, supplemented with drugs as indicated. Neurons were incubated for 13 hours at 37°C and 5% $CO_2$ to allow for EGFP expression from the reporter plasmid, and cells were then fixed with 4% PFA in PBS for 20 min. at ambient temperature. After three washes with PBS, coverslips were

mounted onto glass slides using a drop of Fluoromount G® mounting media, and stored at room temperature until imaging. For imaging, coverslips were screened using an upright confocal microscope BX61WI with a 60x oil immersion objective (Olympus PlanApo N 60x/1.42 Oil). Cells exhibiting a clear nuclear green fluorescence at least as bright as cytosolic fluorescence level were identified as transfected and EGFP-expressing neurons, and images thereof were acquired using the confocal mode. At least ten cells on at least two coverslips were imaged per treatment group for every experiment. For each image, a stack of at least 4 slices at 0.5 µm steps in the Z direction was acquired, and stacks were Z-projected by pixel-wise maximum intensity projection. Flattened images were analyzed using the MatLab software package. After thresholding to eliminate background fluorescence, the cell soma was outlined to measure average intensity. Fluorescence intensities of all imaged cells are expressed as fold-values of the average of the respective DMSO-treated control group within the same experiment (normalized GFP fluorescence).

### 2.4.3 UAS-E4$_{TATA}$::EGFP-fLuc Reporter Assay in Neurons

Neurons grown on coverslips as described above were cotransfected between DIV 7 and 12 with 0.5 µg of the UAS-E4$_{TATA}$::EGFP-fLuc reporter plasmid and 0.2-0.3 µg of the Gal4-RARx receptor plasmid per well using the lipofectamine™ 2000 method. Before transfection, 500 µL of neuron culture media were removed and stored at 37°C. For transfection, mixed reporter and receptor DNAs and 0.5 µL of lipofectamine per well were dissolved separately into 25 µL of OptiMEM media each and incubated at ambient temperature for 5 min. Contents of DNA- and lipofectamine-containing tubes were then combined and mixed well, incubated at room temperature for another 20 min. before 50 µL of the mix were added into the remaining 500 µL per well of the neuron culture. After an incubation period of 2 hours at 37°C and 5% $CO_2$, transfection media were aspirated and replaced with 495 µL of pre-conditioned media per well. 2-6 days post-transfection, drugs as indicated were diluted in fresh NGM at 2x final concentration and 500 µL of drug-containing NGM were added to the wells. After incubation of cells with drugs for 24h at 37°C and 5% $CO_2$ coverslips were fixed, mounted and imaged as described above (see

RARE-TK::EGFP reporter assay in neurons).

### 2.4.4 aGEPRA G Imaging in Living Neurons

For live cell imaging, dissociated neurons were plated on nunc™ 8-chambered cover glasses at a density of 2.8 x $10^4$ cells per well. Cells were maintained as described under "Dissociated Rat Hippocampal Neuron Culture" except that phenol red-free NGM was used. Between DIV 10 and DIV 14, cells were transfected with aGEPRA G expression vector using per well of a chambered cover glass 0.175 µL of Lipofectamine 2000 and 0.175 µg of plasmid in 4.5 µL OptiMEM each. 9 µL of transfection mixture were added to 180 µL of NGM per well. Lipofectamine-containing media were aspirated after 2-3 hours and replaced with 360 µL pre-conditioned and fresh NGM at a 1:1 ratio. 2 days post-transfection, wells were supplied with 360 µL equilibrated, fresh NGM and imaged on an inverted Zeiss LSM 710 confocal microscope equipped with an oil-immersion objective (Carl Zeiss Plan-Apochromat 63x/1.40 Oil DIC) and an environmental control chamber. During image acquisition, temperature was maintained at 37°C and $CO_2$ was 5%. aGEPRA-expressing cells were thoroughly examined for healthy dendritic morphology and absence of fluorescent aggregates before selection for long-term imaging. For each cell, ten baseline images were recorded at 1 minute intervals, followed by drug application (TTX+CNQX or DMSO) and recording of 24 images at 5 minute intervals to yield 120 minutes total imaging time in the presence of the drug. Last, 1 µM RA was applied and another ten images were recorded at 1 minute intervals. For drug application, environmental control chamber was opened to access the nunc 8-well chamber, and 40 µL of phenol red-free NGM with indicated drugs at 10x dilution were added to the appropriate well to yield 400 µL of NGM containing a final 1x drug concentration. Final concentrations of drugs were CNQX, 10 µM (prepared as a 50 mM 5000x stock in DMSO); TTX, 1 µM (prepared as a 1 mM 1000x stock); DMSO 1:1000. At each time point, images were acquired in three channels; with 458 nm laser excitation we simultaneously recorded the CFP emission (475 nm - 500 nm emission window) and the FRET channel (516 nm - 590 nm), followed by the YFP emission channel (516 nm - 590 nm emission window) under

514 nm laser excitation. The confocal pinhole was completely open to maximize signal intensity, and Z-stacks with 1 - 2 µm step size were obtained for cells thicker than 3 µm. Image analysis was done using the imageJ-based Fiji application. Images were converted to 32-bit and smoothened using the Fiji smoothen function. Z-stacks were Z-projected for each channel by pixel-wise maximum intensity projection. The FRET channel was then thresholded using the thresholding tool by applying the "Triangle" method. Where necessary, the automatic threshold was manually adjusted to reduce background noise. Subthreshold pixel values were set to NaN ("not a number") to be excluded from further analysis. Ratiometric CFP/YFP images were calculated as CFP emission channel pixel value over thresholded FRET channel pixel value using the Ratio Plus ImageJ plugin without further thresholds or multiplication factors. For measurements of individual channel intensities (Figure 3.8), the CFP emission channel was separately thresholded using the "Triangle" thresholding method. The soma of the neuron was outlined in the ratiometric image as well as the thresholded CFP and FRET channels and the average pixel intensity was measured for each image of CFP emission, FRET emission, and $CFP_{em}/YFP_{em}$ ratio channels for the entire time stack . Because ratiometric images exhibited some variability even within the same cell (see Figure 5D), each value (CFP, FRET, ratio) was separately normalized to its corresponding average baseline intensity value (average of the first 10 images). The resulting normalized time-lapse traces for all recordings are shown in Figures 3.6 and 3.7.

### 2.4.5 HEK 293T Cell Culture and UAS-$E4_{TATA}$::EGFP-fLuc Reporter Assay in HEK 293T Cells

HEK or HEK 293T cells were maintained in DMEM + 10% FCS without antibiotics in tissue culture plastic dishes. At 3-4 day intervals, cells were detached from the growth surface and dissociated using a brief trypsin treatment. Cell suspensions were split at a 1:10 to 1:15 ratio and reseeded into fresh tissue culture plastic dishes. For the UAS-$E4_{TATA}$::EGFP-fLuc reporter assay, HEK 293T cells were seeded on gelatin-coated glass coverslips in a 24-well plate at a density of 75,000 cells per well. Cotransfection of reporter and receptor DNAs (1.5 µg per well of UAS-$E4_{TATA}$::EGFP-fLuc reporter plasmid and

either 100 ng of Gal4-RARx-VP16 receptor plasmid per well or 200 ng of Gal4-RARx receptor plasmid per well) was performed the evening after plating using the calcium phosphate method. Plasmid DNA was mixed with 2.5 µL of a 2.5 M $CaCl_2$ solution and the volume was adjusted to 25 µL with $H_2O$. DNA-calcium solution was then added drop-wise into 25 µL of 2x HEPES buffer and the mix was set at room temperature for 20 min. to allow formation of microcrystals. Total 50 µL of the resulting solution was then added drop-wise to the cells plated the day before. After overnight incubation at 37°C and 5% $CO_2$, transfection media was aspirated and replaced with fresh HEK cell media. 24h after transfection, cell culture media was replaced and cells were incubated for 24h in the dark with either 250 nM RA or 1:40,000 DMSO as vehicle control. Coverslips were then fixed using 4% PFA in PBS for 20 min. at room temperature and mounted using Mowiol mounting media. Coverslips were imaged using an upright epifluorescence microscope (Leica DMRB) equipped with a 40x objective lens. For quantification of GFP fluorescence intensity, color images were background thresholded using the Fiji "Color Threshold" adjustment tool with a lower brightness threshold between 7 and 15, using the same value for all images throughout the same experiment. The thresholded areas were loaded into the Fiji Particle Analyzer with a minimum particle size cutoff of 300 px to exclude speckles and noise. The remaining particles were outlined and overlayed over the original image as selection for quantification of GFP brightness by the "Average Intensity" measurement from the Fiji "Measure" tool.

### 2.4.6 Two-Photon Microscopy for Ratiometric FRET Measurements in HEK 293T Cells

HEK 293T cells for 2-photon microscopy were seeded on gelatin-coated coverslips in 24-well cell culture dishes at a density of 75,000 cells per well. The day after plating, cells were transfected with 1 µg of expression plasmid per well using the calcium phosphate method as described above. In separate wells we expressed either fluorophore individually (i.e. CFP4, YPet, Clover, mRuby2), or the FRET constructs (i.e. aGEPRA G, Clover-mRuby2 fusion).

Coverslips were submerged in 2 mL 2p-imaging buffer and placed on a custom-built two-photon microscope (based on an upright Olympus BX-61W microscope) equipped with a 40x water-dipping objective (Olympus LUMPlanFl W/IR-2, NA 0.8). A Mai Tai HP Deep See Ti:sapphire laser (Spectra Physics, Inc.), tunable from 690 to 1040 nm, was used at 15 mW laser output power for 2-photon excitation. All 2-photon microscopy recordings were done at ambient temperature. 2-photon laser excitation spectra for Clover, mRuby2, and the Clover-mRuby2 fusion FRET construct were recorded between 740 nm and 1040 nm at 5 nm steps with emission filter sets 525/70 (Clover) and 607/45 (mRuby2), separated by a 575 dichroic. 2-photon laser excitation spectra for CFP4, YPet, and the aGEPRA G FRET construct were recorded between 690 nm and 1040 nm at 5 nm steps with emission filter sets 480/40 (CFP4) and 535/50 (YPet), separated by a 505 dichroic. After a spectrum of aGEPRA G-expressing cells was obtained, 200 µL of 2p-imaging buffer supplemented with 10 µM RA was added to the cells by pipetting, yielding a final RA concentration of 1 µM. 5 min. after addition of RA, the second spectrum was obtained from the same cells.

Images were analyzed using Fiji image analysis software. Brightness was measured at cytosolic regions of interest in cells exhibiting intermediate levels of fluorescence. Intensity values were normalized to peak fluorescence and plotted against 2-photon laser excitation wavelength as described in the results section, where the method for quantification of FRET is also derived and explained ("3.5 Ratiometric FRET Measurements by Two-Photon Microscopy").

### 2.4.7 Spectrophotometry of FRET Constructs in HEK Cell Lysates

To obtain cell lysates containing the FRET-based RA reporter proteins, we seeded 2x $10^6$ HEK cells on a 100 mm tissue culture plate. The next morning, HEK cells were transfected with 12 µg of reporter plasmid DNA using the calcium phosphate method. Plasmid DNA was mixed with 25 µL of a 2.5 M $CaCl_2$ solution and the volume was adjusted to 250 µL with $H_2O$. DNA-calcium solution was then added drop-wise into 250 µL of 2x HEPES buffer and the mix was set at room temperature for 20 min. to allow formation of

microcrystals. Total 500 µL of the resulting solution was then added drop-wise to the HEK cells plated the day before. After 6-8 h incubation at 37°C and 5% $CO_2$, transfection media was aspirated and replaced with fresh HEK cell media. Cells were allowed to express the FRET constructs for 48 h, after which cells were dissociated by trypsin treatment and harvested by centrifugation (250x g, 5 min.). Cells were washed once by resuspending in 0.5x PBS and centrifugation, and the resulting cell pellets were then resuspended in 450 µL $H_2O$ per pellet, snap-frozen in liquid nitrogen and stored at -80°C until further use. After thawing on ice, 50 µL of 10x PBS were added to adjust salt concentration of the lysates to 1x PBS; lysates were then cleared by centrifugation in a tabletop centrifuge (13,200 x g for 10 min.) to eliminate cell nuclei and debris.

150 µL of cleared lysate were filled into a quartz cuvette with a path length of 1 cm and the fluorescence emission spectrum was obtained between 430 nm and 630 nm at 1 nm steps (5 nm slit width) under 434 nm excitation using a spectrophotometer (Horiba Jovin Yvon Fluoromax-4). Next, 15 µL of the same lysate were supplemented with 10 µM RA and added into the cuvette and mixed by pipetting to yield a final RA concentration of 1 µM. A second spectrum in the presence of 1 µM RA was then recorded as above. The two spectra without and with 1 µM RA were normalized to peak CFP emission at 477 nm and overlayed to visualize FRET changes induced by RA.

### 2.4.8 Construction of Gal4-RARx-VP16 Chimeric Receptors and UAS-E4$_{TATA}$::fLuc-EGFP Reporter

To construct the Gal4-RARx-VP16 chimeric receptors, the Gal4 DBD and a tandem repeat of 2x VP16 transactivator domain were separately synthesized as double-stranded linear DNA elements (gBlocks, Integrated DNA Technologies). The 2x VP16 gBlock was designed to contain a multiple cloning site preceding the coding sequence of the VP16 tandem repeat to facilitate future use of the construct. The Gal4-DBD gBlock was cloned into the pEGFP-N1 plasmid using the *Nhe*I and *Not*I restriction sites, replacing the EGFP as well as the vector's multiple cloning site. Five colonies were selected for DNA sequencing, none of which contained an insert completely matching the designed Gal4-DBD se-

quence. The colony containing the K43R mutation was identified as the most conservative (or structurally least disruptive) amino acid exchange and was hence selected for further experiments. Subsequently, the 2x VP16 tandem repeat insert was intdroduced into the Gal4-DBD plasmid using the *Eco*RI and *Not*I restriction enzymes. This afforded the Gal4-2x VP16 chimeric transcriptional activator plasmid with a multiple cloning site which served as a platform for making the Gal4-RARx-VP16 chimeric receptor constructs. RAR sequences were PCR-amplified from plasmids containing the full-length rat RARα, mouse RARβ, or rat RARγ and were then introduced into Gal4-2x VP16 plasmid. For the rat RARα and RARγ LBD sequences, *Eco*RI and *Bam*HI restriction enzyme sites were used, and for the mouse RARβ LBD, *Age*I and *Bam*HI restriction enzyme sites were used. Gal4-RARx chimeric receptor constructs were derived from the respective Gal4-RARx-VP16 plasmids by excising the 2x VP16 tandem repeat using *Bam*HI and *Bgl*II restriction enzymes and religating the two compatible ends.

To build the UAS-E4$_{TATA}$::fLuc-EGFP reporter plasmid, we first PCR-amplified the UAS-E4$_{TATA}$ regulatory sequence from the UAS$_5$-E4$_{TATA}$::fluc plasmid (Paulmurugan *et al.*, 2009) (a kind gift from the Paulmurugan lab) and subcloned it into the pEYFP plasmid using the *Ase*I and *Age*I restriction enzyme sites. A sequence encoding for a fLuc-EGFP fusion protein PCR-amplified from the pFluc(G4S)3-GFP plasmid (kind gift from the Paulmurugan lab) was introduced into the resulting plasmid using the *Age*I and *Not*I restriction enzyme sites, thereby replacing the YFP. This finally yielded the complete UAS-E4$_{TATA}$::fLuc-EGFP reporter plasmid used for cotransfection with the Gal4-RAR chimeric receptors.

### 2.4.9 Construction of Modular FRET Sensors for RA

Modular FRET sensors (Figure 3.4) were constructed in the pmCFP-N1 vector. mYFP and RARα LBD were PCR-amplified and sequentially introduced into the pmCFP-N1 vector using *Nhe*I and *Xho*I for mYFP, and *Xho*I and *Bam*HI restriction enzyme sites for the RARα LBD. mCFP was subsequently PCR-amplified with a forward primer containing a *Bam*HI restriction enzyme site and then seamlessly ligated into the previously ob-

tained plasmid to eliminate the remaining sites from the endogenous multiple cloning site. NR boxes with long and short linkers as well as AxxAA binding-incompetent NR box mutants were synthesized as a gBlock (Integrated DNA Technolgies) and introduced using *Xho*I and *Bgl*II restriction enzyme sites. This afforded plasmids containing modular FRET sensors for RA with domains separated by restriction enzyme sites and the general domain structure (*Nhe*I)-mYFP-(*Xho*I)-NR box-(*Bgl*II)-RARα LBD-(*Bam*HI)-mCFP-(*Not*I). The I393Q mutation was introduced by mutagenesis PCR using complementary mutagenic primers spanning the desired mutation on a plasmid containing the wild-type RARα LBD sequence. The resulting PCR product was then digested with methylation-sensitive restriction enzyme *Dpn*I which only destroys the methylated wild-type PCR template, leaving the non-methylated PCR product intact. This PCR product was then transformed into bacteria (XL10-Gold chemically competent *Escherichia coli*, strain DH5α, Agilent Technologies # 200315). Plasmid DNA was prepared from 3-5 mL of bacterial overnight culture using Genejet Plasmid Miniprep Kit (ThermoFisher # K0503) and correct sequences were confirmed by DNA sequencing (ElimBio).

### 2.4.10 Polymerase Chain Reaction (PCR)

PCR is the method of choice to selectively and efficiently generate large amounts of target DNA by enzymatic amplification of a given DNA template. Short oligonucleotide primers (typically 18-30 nucleotides long) flanking the DNA region to be amplified are designed such that primer extension in the 3' direction by the action of a DNA polymerase yields DNA fragments identical to the template. The sequence-specific incorporation of dNTPs into the growing strand follows the rule of complementary base pairing, ensuring specificity and accuracy of the reaction. Repeated cycles (usually 35 cycles) of heating and cooling provide optimal reaction conditions for sequential DNA double strand break-up ("melting" at 98°C), primer binding ("annealing" at a primer-specific Tm, usually between 58°C and 67°C) and primer extension by a heat-stable DNA polymerase ("extension" at 68°C). The amount of PCR product grows exponentially with increasing cycle number because all DNA strands, including those synthesized during the reaction

itself, may serve as templates for subsequent rounds of amplification.

PCR reaction mixtures were set up at 50 μL total volume per reaction. Primers were ordered from ElimBio and dissolved at a concentration of 100 μM. Final primer concentration in the PCR reaction mix was 0.5 μM. Primer Tm was calculated with the Tm calculator tool on the ThermoFisher Scientific website, and for any reaction the lowest calculated Tm of the primers used in the reaction was applied. Primer extension time per PCR cycle was calculated as 30 s/kbp of PCR product length.

TABLE 2.5| **PCR Primers Used in This Study**

| Chen Lab primer # | Sequence (capital letters are complementary to target) | Restriction enzyme sites | Description |
|---|---|---|---|
| 1416 | gagggctctctcctactcaagcttcttcgtgcttctgga tccGTGAGCAAGGGCGAGGAGCTG | *Bam*HI | forward primer to amplify XFP; used to introduce C-terminal CFP into FRET construct |
| 1417 | TCGCGGCCGCTTTACTTGTAC | *Not*I | reverse primer to amplify XFP; used to introduce C-terminal CFP into FRET construct |
| 1539 | cattacgctagcATGGTGAGCAAGGGCGAGGAG | *Nhe*I | forward primer to amplify XFP; used to include N-terminal YFP into FRET construct |
| 1540 | cattacctcgaggcGTACAGCTCGTCCATGCCGAG | *Xho*I | reverse primer to amplify XFP; used to include N-terminal YFP into FRET construct |
| 1545 | atggatcctgtccggACTTGTACAGCTCGTCCATGCCG | *Bam*HI, *Bsp*EI | reverse primer to amplify XFP; used to include N-terminal XFP into tandem CFP-YFP or YFP-CFP FRET as FRET positive controls; can be used in combination with 1411 or 1539 |
| 1556 | cactcgagAGCagatctGAGCTACACGCTGACACC | *Xho*I, *Bgl*II | Forward primer to introduce RARα LBD into flipped FRET constructs, C-terminal to NR box |
| 1557 | acggatccGTCCAAGCCCTCAGAGTTC | *Bam*HI | Reverse primer to introduce RARα LBD into flipped FRET constructs, C-terminal to NR box |
| 1558 | acggatccAGATTGAGTGGCTGGGC | *Bam*HI | Reverse primer to introduce RARα LBD-F into FRET constructs, C-terminal to NR box |
| 1568 | CTCACATGTTTCCAAAGATCcTAATGAAAATCACtGATC TCCGCAGCATC | | to remove naturally occurring *Bgl*II sites within the mouse RARβ LBD |
| 1569 | GATGCTGCGGAGATCaGTGATTTTCATTAgGATCTTTGG AAACATGTGAG | | to remove naturally occurring *Bgl*II sites within the mouse RARβ LBD |
| 1570 | GCTGAACGGGTGcagACATTGAAGATGGAGATC | | forward primer to introduce I393Q point mutation into rat RARα LBD |
| 1571 | CCATCTTCAATGTctgCACCCGTTCAGCTTCCC | | reverse primer to introduce I393Q point mutation into rat RARα LBD |
| 1575 | GCGCACCGGTGGATCCCATGGTGAGC | *Age*I, *Bam*HI | Used to amplify GEPRA constructs to clone into pEXFP-N1 vectors |
| 1576 | AGTCGCGGCCGCTCGAGTTACTTGTACAGCTCGTTCATG | *Not*I, *Xho*I | Used to amplify GEPRA B construct to clone into pEXFP-N1 vectors |
| 1584 | ccatgagctcTTCATGTCCTTCAGAATTCTCC | *Sac*I | Used to amplify mouse RARβ LBD from GEPRA G and AA constructs |
| 1585 | cgcccgcatgcatGAGAGCTATGAGATGACAGC | *Sph*I | Used to amplify mouse RARβ LBD from GEPRA G and AA constructs |
| 1621 | AGTTATTAATCCCGAGCTCATTTAGGTGACACTATAG | *Ase*I, *Sac*I | To amplify $UAS_5$-$E4_{TATA}$ promoter/enhancer region from UAS-E4-fluc vector for cloning into EXFP-N1 |

TABLE 2.5| **PCR Primers Used in This Study** (continued)

| Chen Lab primer # | Sequence (capital letters are complementary to target) | Restriction enzyme sites | Description |
|---|---|---|---|
| 1622 | GGCGACCGGTCCCCTCGAGACACCACTCGACACGGCACC | *Age*I, *Xho*I | To amplify $UAS_5$-$E4_{TATA}$ promoter/enhancer region from UAS-E4-fluc vector for cloning into EXFP-N1 |
| 1623 | gccggaattcGGGGAACTCATCGAGAAGG | *Eco*RI | To amplify RARα LBD from clone #275 for cloning into Gal4-MCS-VP16 (clone #699) |
| 1624 | gggcggatccGCCCTCAGAGTTCTCCAAC | *Bam*HI | To amplify RARα LBD from clone #275 for cloning into Gal4-MCS-VP16 (clone #699) |
| 1625 | gggcggatccTGGGGATTGAGTGGCTG | *Bam*HI | To amplify RARα LBD+F from clone #275 for cloning into Gal4-MCS-VP16 (clone #699) |
| 1626 | gggtaccggtGACGACCTCACTGAGAAGATCC | *Age*I | To amplify RARβ LBD from clone #276a for cloning into Gal4-MCS-VP16 (clone #699) |
| 1627 | gggcggatccTCCTTCAGAATTCTCCAGCATT | *Bam*HI | To amplify RARβ LBD from clone #276a for cloning into Gal4-MCS-VP16 (clone #699) |
| 1628 | gggcggatccCTGCAGCAGTGGTGACTGA | *Bam*HI | To amplify RARβ LBD+F from clone #276a for cloning into Gal4-MCS-VP16 (clone #699) |
| 1629 | gccggaattcGAGGAGCTCATCACCAAGGTC | *Eco*RI | To amplify RARγ LBD from clone #277 for cloning into Gal4-MCS-VP16 (clone #699) |
| 1630 | gggcggatccCATCTCAGGGTTCTCCAGCATC | *Bam*HI | To amplify RARγ LBD from clone #277 for cloning into Gal4-MCS-VP16 (clone #699) |
| 1631 | gggcggatccGGGGCCCTGGTCAGG | *Bam*HI | To amplify RARγ LBD+F from clone #277 for cloning into Gal4-MCS-VP16 (clone #699) |
| 1632 | atccgctagcgacaagcttATGAAGCTACTGTCTTCTATCGAAC | *Nhe*I, *Hind*III | To clone any Gal4-LBD-VP16 construct into EXFP-N1 vector, replacing EGFP and multiple cloning site |
| 1633 | agtcgcggccgcTTAAACGGGCCCTCTAGATCTAGAG | *Not*I | To clone any Gal4-LBD-VP16 construct into EXFP-N1 vector, replacing EGFP and multiple cloning site |
| 1634 | atccaccggtcgccaccATGGAAGACGCCAAAAACATAAAG | *Age*I | To clone fLuc-EGFP from Paulmurugan's vector into EXFP-N1, preserving multiple cloning site |
| 1635 | agtccgccggcgtTTACTTGTACAGCTCGTCCATGC | *Not*I | To clone fLuc-EGFP from Paulmurugan's vector into EXFP-N1, preserving multiple cloning site |

TABLE 2.5| **PCR Primers Used in This Study** (continued)

| Chen Lab primer # | Sequence (capital letters are complementary to target) | Restriction enzyme sites | Description |
|---|---|---|---|
| 1672 | ggtgactagtATGAGAGCTATGAGATGACAGC | *Spe*I | Cloning C-terminal aGEPRA B (RARβ LBD + YPet); used together with #1576 as reverse primer |
| 1673 | ggtgactagtATGGTGAGCAAG | *Spe*I | Cloning N-terminal aGEPRA B (CFP + RARβ LBD) |
| 1674 | tatactcgagttaTTCATGTCCTTCAGAATTCTCC | *Xho*I | Cloning N-terminal aGEPRA B (CFP + RARβ LBD) |
| 1675 | ggtgactagtATGACAGCTATGAACTGAGTCC | *Spe*I | Cloning C-terminal aGEPRA G (RARγ LBD + YPet) |
| 1676 | tatagaattcTTAGTCCTCGATGTTGTG | *Eco*RI | Cloning C-terminal aGEPRA G (RARγ LBD + YPet) |
| 1677 | GGTGACTAGTATGGTGAGCAAG | *Spe*I | Cloning N-terminal aGEPRA G (CFP + RARγ LBD) |
| 1678 | tatagaattcttaCTCAAACATCTCCGGGTTC | *Eco*RI | Cloning N-terminal aGEPRA G (CFP + RARγ LBD) |

TABLE 2.6| **Plasmids Used in This Study**

| **Modular FRET Sensors for RA** | | | | |
|---|---|---|---|---|
| Chen Lab clone # | Clone name | Made by | Species | Description |
| 642 | NR box gBlock | Maik | | tandem NR boxes gBlock cloned into pEYFP-N1 |
| 664 | flipFRET LBDnoF NRs | Maik | rat | short linker |
| 665 | flipFRET LBDnoF NRl | Maik | rat | long linker |
| 666 | flipFRET LBD+F NRs | Maik | rat | short linker |
| 667 | flipFRET LBD+F NRl | Maik | rat | long linker |
| 668 | flipFRET LBDnoF AAAs | Maik | rat | binding-incompetent AxxAA NR box mutant; short linker |
| 669 | flipFRET LBDnoF AAAl | Maik | rat | binding-incompetent AxxAA NR box mutant; long linker |
| 670 | flipFRET LBD+F AAAs | Maik | rat | binding-incompetent AxxAA NR box mutant; short linker |
| 671 | flipFRET LBD+F AAAl | Maik | rat | binding-incompetent AxxAA NR box mutant; long linker |
| 672 | flipFRETmut LBDnoF NRs | Maik | rat | LBD I393Q point mutation introduced by primers 1570/1571 into clone #664 to abolish corepressor binding to apo-LBD |
| 673 | flipFRETmut LBDnoF NRl | Maik | rat | LBD I393Q point mutation introduced by primers 1570/1571 into clone #665 to abolish corepressor binding to apo-LBD |
| 674 | flipFRETmut LBD+F NRs | Maik | rat | LBD I393Q point mutation introduced by primers 1570/1571 into clone #666 to abolish corepressor binding to apo-LBD |
| 675 | flipFRETmut LBD+F NRl | Maik | rat | LBD I393Q point mutation introduced by primers 1570/1571 into clone #667 to abolish corepressor binding to apo-LBD |
| 676 | flipFRETmut LBDnoF AAAs | Maik | rat | LBD I393Q point mutation introduced by primers 1570/1571 into clone #668 to abolish corepressor binding to apo-LBD |
| 677 | flipFRETmut LBDnoF AAAl | Maik | rat | LBD I393Q point mutation introduced by primers 1570/1571 into clone #669 to abolish corepressor binding to apo-LBD |
| 678 | flipFRETmut LBD+F AAAs | Maik | rat | LBD I393Q point mutation introduced by primers 1570/1571 into clone #670 to abolish corepressor binding to apo-LBD |
| 679 | flipFRETmut LBD+F AAAl | Maik | rat | LBD I393Q point mutation introduced by primers 1570/1571 into clone #671 to abolish corepressor binding to apo-LBD |

TABLE 2.6| **Plasmids Used in This Study** (continued)

| **Gal4-RAR and UAS-E4$_{TATA}$::fLuc-eGFP Reporter System** | | | | |
|---|---|---|---|---|
| Chen Lab clone # | Clone name | Made by | Species | Description |
| 694 | pUAS5-E4TATA::fluc | Paulmurugan Lab | | Use primers #1621 and #1622 to amplify UAS$_5$-E4$_{TATA}$ promoter/enhancer |
| 696 | UAS5-E4TATA in clone #86 | Maik | | UAS$_5$-E4$_{TATA}$ amplified from clone #694 using primers #1621/1622 and cloned into clone #86 using *Ase*I and *Age*I sites |
| 697 | pUAS5-E4TATA::fluc-EGFP | Maik | | Promoter/Enhancer region sequenced using primer #1636 |
| 698 | Gal4 DBD (K43R) | Maik | | gBlock of Gal4 DBD synthesized and cloned into pEYFP-N1 using *Nhe*I/*Not*I |
| 699 | pGal4-MCS-VP16 | Maik | | gBlock of VP16x2 synthesized and cloned into #698 using *Eco*RI/*Not*I |
| 700 | pGal4-RARa-VP16 | Maik | rat RARα | RAR alpha LBD 182-416 amplified from clone #275 using primers #1623/1624; PCR product cloned into clone #699 using *Eco*RI/*Bam*HI |
| 701 | pGal4-RARaF-VP16 | Maik | rat RARα | RAR alpha LBD+F 182-459 amplified from clone #275 using primers #1623/1625; PCR product cloned into clone #699 using *Eco*RI/*Bam*HI |
| 702 | pGal4-RARb-VP16 | Maik | mouse RARβ | RAR beta LBD 178-412 amplified from clone #276a using primers #1626/1627; PCR product cloned into clone #699 using *Age*I/*Bam*HI |
| 703 | pGal4-RARbF-VP16 | Maik | mouse RARβ | RAR beta LBD+F 178-448 amplified from clone #276a using primers #1626/1628; PCR product cloned into clone #699 using *Age*I/*Bam*HI |
| 704 | pGal4-RARg-VP16 | Maik | rat RARγ | RAR gamma LBD 214-414 amplified from clone #277 using primers #1629/1630; PCR product cloned into clone #699 using *Eco*RI/*Bam*HI |
| 705 | pGal4-RARgF-VP16 | Maik | rat RARγ | RAR gamma LBD+F 214-485 amplified from clone #277 using primers #1629/1631; PCR product cloned into clone #699 using *Eco*RI/*Bam*HI |
| 717 | pGal4-RARa(noF)-no VP16 | Maik/ Jinkyung | rat RARα | deleted VP16 domain from clone #700 by *Bgl*II-*Bam*HI digestion and religation to itself |
| 718 | pGal4-RARaF-no VP16 | Maik/ Jinkyung | rat RARα | deleted VP16 domain from clone #701 by *Bgl*II-*Bam*HI digestion and religation to itself |
| 719 | pGal4-RARb(noF)-no VP16 | Maik/ Jinkyung | mouse RARβ | deleted VP16 domain from clone #702 by *Bgl*II-*Bam*HI digestion and religation to itself |
| 720 | pGal4-RARbF-no VP16 | Maik/ Jinkyung | mouse RARβ | deleted VP16 domain from clone #703 by *Bgl*II-*Bam*HI digestion and religation to itself |

TABLE 2.6| **Plasmids Used in This Study** (continued)

| **GEPRA FRET Sensors for RA** | | | | |
|---|---|---|---|---|
| Chen Lab clone # | Clone name | Made by | Species | Description |
| 725 | GEPRA AA | Miyawaki Lab | mouse | Shimozono *et al.*, 2013 |
| 726 | GEPRA B | Miyawaki Lab | mouse | Shimozono *et al.*, 2013 |
| 727 | GEPRA G | Miyawaki Lab | mouse | Shimozono *et al.*, 2013 |
| 728 | aGEPRA AA | Miyawaki Lab | mouse | Plasmid #725 with solubility domain |
| 729 | aGEPRA B | Miyawaki Lab | mouse | Plasmid #726 with solubility domain |
| 730 | aGEPRA G | Miyawaki Lab | mouse | Plasmid #727 with solubility domain |
| 767 | Nterm CFP4-aGEPRA B | Maik | mouse | N-terminal part of aGEPRA B including CFP4 and solubility domain |
| 768 | Cterm YPet-aGEPRA B | Maik | mouse | C-terminal part of aGEPRA B including YPet and solubility domain |
| 769 | Nterm CFP4-aGEPRA G | Maik | mouse | N-terminal part of aGEPRA G including CFP4 and solubility domain |
| 770 | Cterm cpYPet-aGEPRA G | Maik | mouse | C-terminal part of aGEPRA G including cpYPet and solubility domain |
| **Clover and mRuby2 FRET Pair Plasmids** | | | | |
| Chen Lab clone # | Clone name | Made by | | Description |
| 774 | pcDNA3 Clover | Michael Lin Lab | | Clover in pcDNA3 expression vector |
| 775 | pcDNA3 mRuby2 | Michael Lin Lab | | mRuby2 in pcDNA3 expression vector |
| none | pcDNA3 Clover-mRuby2 | Maik | | Clover-mRuby2 fusion protein in pcDNA3 expression vector |
| **General Plasmids** | | | | |
| Chen Lab clone # | Clone name | Made by | Species | Description |
| 86 | pEYFP-N1 (mYFP A206K) | Christine Nam | | Contains frame shift mutation |
| 86a | pEYFP-N1 (mYFP A206K) | Maik | | Monomeric YFP (A206K mutation); clone #86 mutagenised using primers 1537 and 1538 |
| 87 | pEYFP-N1 (mCFP A206K) | | | Monomeric CFP (A206K mutation) |
| 275 | Rat RARalpha - GFP | Jason Aoto | rat | amplified from rat cDNA using an internal primer that introduced a silent mutation T1017C to generate an internal *Xba*I site - sequencing OK |
| 276 | Mouse RARbeta-GFP | Jason Aoto | mouse | amplified mRARβ from mouse hippocampal cDNA - we used a natural *Eco*RV internal restriction site to amplify two fragments - full sequence OK |
| 276a | Mouse RARbeta(mutant)-GFP | Maik | mouse | internal *Bgl*II restriction sites within RARβ LBD from clone #276 abolished by silent nucleotide mutations T1111C and A1125T using primers 1568/1569; RARβ full sequence OK |
| 277 | rat RARgamma-GFP | Jason Aoto | rat | amplified from rat cDNA as a single PCR fragment - no stop codon |
| 496 | RARalpha FL in pGEX-KG | Mike Poon | rat | Amplified RARα from rat brain; cloned into pGEX KG with *Bam*HI/*Eco*RI |

# 3. RESULTS

## 3.1 Calcineurin Regulates RA-Dependent Homeostatic Synaptic Plasticity

We showed in a previous study that intracellular calcium levels maintained during normal synaptic transmission suppress RA production, and a drop in intracellular calcium level is sufficient to induce RA-dependent homeostatic synaptic strengthening. Additionally, this study showed that the intracellular calcium regulation and the following RA-dependent homeostatic synaptic strengthening occur cell-autonomously (Wang *et al.*, 2011). We therefore wanted to investigate how intracellular calcium levels and RA-dependent homeostatic synaptic plasticity are linked. Based on the hypothesis that the calcium-dependent effect of RA synthesis might be regulated through calcium-dependent phosphatase or kinase signaling pathways, we investigated the effects of pharmacological protein phosphatase blockers on synaptic transmission. We found that FK506 and cyclosporin A (CsA), two drugs that specifically block the activity of the calcium-dependent protein phosphatase calcineurin (CaN, also called protein phosphatase 2B, PP2B), both lead to an increase in excitatory synaptic transmission while reducing inhibitory synaptic transmission (Arendt *et al.*, 2015). Application of these calcineurin inhibitors can thus mimic the electrophysiological phenotype of RA-dependent homeostatic synaptic plasticity. By contrast, okadaic acid, a blocker of the calcium-independent protein phosphatases types 1 and 2A, had no such effect on synaptic transmission (Arendt *et al.*, 2015). We concluded from these experiments that calcineurin might be responsible for the homeostatic adjustment of synaptic transmission when intracellular calcium levels are decreased.

To confirm our hypothesis that calcineurin mediates homeostatic synaptic plasticity through the regulation of RA synthesis we utilized a transcription-based RA reporter to observe RA level changes in reporter-expressing neurons after calcineurin-blocking drug treatments. Our reporter contains a GFP which is expressed under the regulation of three repeats of a RA response element, and a weak thymidine kinase promoter from human

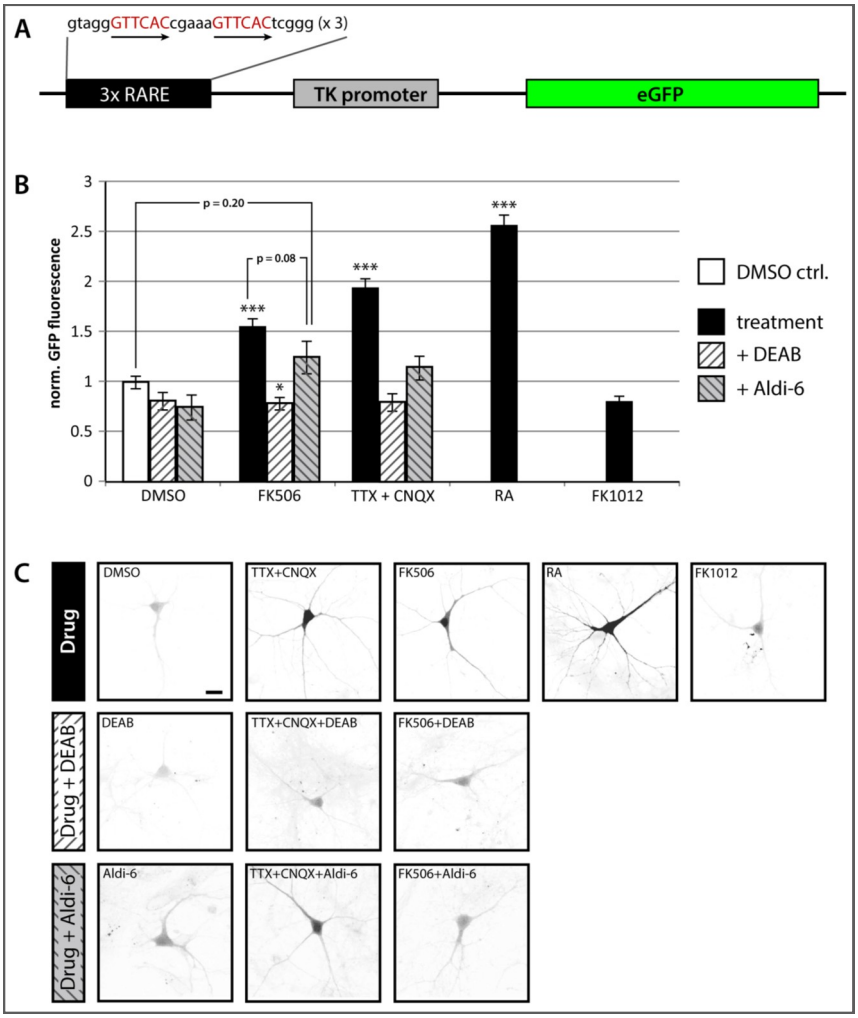


FIGURE 3.1| **RARE-TK::GFP Reporter Activation in Neurons after Calcineurin Blockade. A**, Schematics of the RARE-TK::GFP reporter. GFP is driven by a weak TK promoter and regulated by 3 repeats of a retinoic acid response element. **B**, Quantification of GFP fluorescence in reporter-expressing cultured hippocampal neurons with different drug treatments. Expression levels normalized to DMSO controls are (average ± SEM): DEAB, 80.61 ± 9.00% (N=4, n=51 neurons); Aldi-6, 75.05 ± 12.43% (3/25); FK506, 154.57 ± 8.94% (9/133); FK506+DEAB, 78.48 ± 6.70% (4/52); FK506+Aldi-6, 124.17 ± 16.34% (4/35); TTX+CNQX, 193.37 ± 10.07% (8/117); TTX+CNQX+DEAB, 79.72 ± 8.82% (4/45); TTX+CNQX+Aldi-6, 114.10 ± 12.25% (3/30); RA, 256.20 ± 11.40% (9/69); FK1012, 79.11 ± 7.28% (7/62). *$P < 0.05$; ***$P < 0.001$, student's t-test. **C**, Sample images of GFP intensities in reporter-expressing neurons. Scale bar, 10 µm. (Modified after Arendt *et al.*, 2015)

*Herpes simplex* virus; altogether we refer to this reporter construct as RARE-TK::GFP (Aoto *et al.*, 2008) (Figure 3.1A). We found that RARE-TK::GFP reporter expression in FK506-treated cells was significantly increased by almost 50% when compared to reporter levels in DMSO-treated control cells, comparable to treatment with the network activity-blocking drugs TTX+CNQX (Figure 3.1B and C). Moreover, we tested whether inhibiting the cellular RA synthesis pathway is sufficient to block the increase in reporter acti-

vity induced by calcineurin inhibitors or neuronal network activity blockers. We applied two mechanistically and structurally distinct inhibitors of retinaldehyde dehydrogenase (RALDH), the enzyme that catalyzes the last oxidative step of cellular RA synthesis. We found that DEAB, a competitive inhibitor of RALDH, completely blocked RARE-TK::GFP reporter activation, while Aldi-6, a suicide inhibitor of RALDH, significantly reduced the increase in reporter activity (Figure 3.1B and C).

The RARE-TK::GFP reporter robustly indicates differences in cellular RA concentration when transfected into dissociated neuron cultures. However, differences between RA-treated and DMSO-treated reporter-expressing cells can only be detected within about 10-16 hours after transfection (data not shown). At earlier time points, GFP expression is too low to exceed autofluorescence background, while at later time points even DMSO-treated cells quickly reach saturated GFP fluorescence levels. Similarly, the reporter lost its indicative power when it was delivered to neurons by means of viral infection, either by lentiviral or adeno-associated viral vectors (data not shown). We therefore tried to develop an improved reporter version that could overcome these limitations, thus allowing the use of such RA reporter system for *in vivo* applications in living and behaving animal brains.

## 3.2 Development of a Novel Transcription-Based Reporter for RA

Based on the modular structure of retinoid receptors and the observation that their different biochemical functions are located in distinct protein domains (Bourguet *et al.*, 2000a, Brelivet *et al.*, 2012) (Figure 3.2A, top panel), we engineered a chimeric receptor containing the Gal4 DNA-binding domain (Gal4-DBD) fused to different variants of retinoic acid receptor ligand-binding domains (RAR-LBD) with or without their respective F domains, and added a twofold tandem repeat of the *Herpes simplex* virus protein VP16-transactivation domain (Sadowski *et al.*, 1988) for enhanced transcriptional activity of the artificial receptor chimeras (Gal4-RAR-VP16, Figure 3.2A). These chimeric receptors can only function together with a reporter construct from which our luciferase-EGFP re-

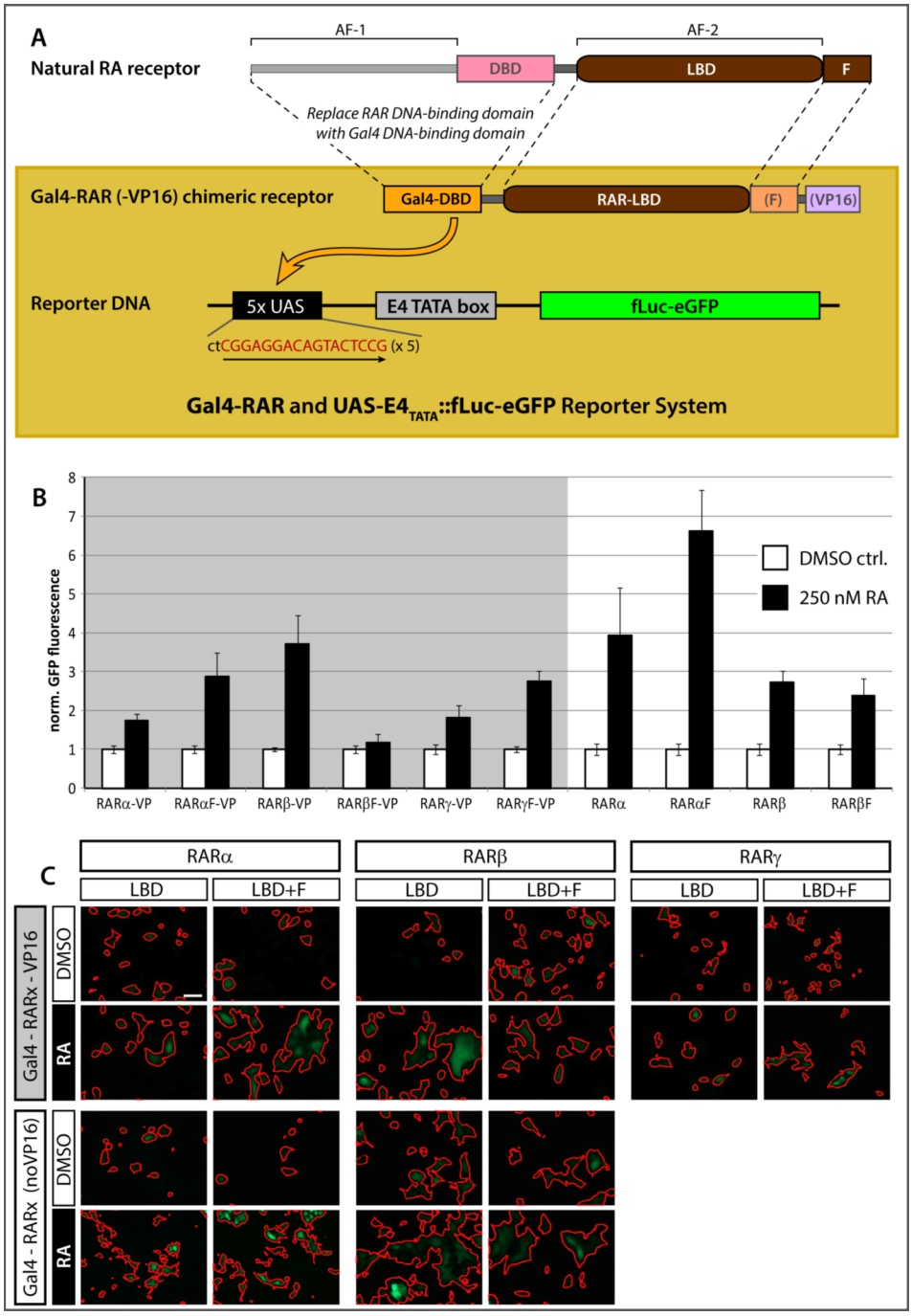


FIGURE 3.2| **Development of a Novel Transcription-Based RA Reporter System. A**, Schematics of the reporter system. Domain structure of a prototypical retinoid receptor is illustrated in the top panel with ligand-independent activation function AF-1 and ligand-dependent AF-2 indicated. N-terminal portion of the receptor including AF-1 and the DNA-binding domain (DBD) was replaced with the DBD from yeast transcription factor Gal4 to yield the chimeric Gal4-RAR receptors. Receptors including or lacking the respective F-domains or VP16 viral transactivator domain (labeled in parentheses) were tested for transcriptional activity and inducibility by ligands. Reporter DNA contains a luciferase-GFP fusion protein (fLuc-EGFP) driven by a weak viral E4 TATA box minimal promoter under the regulation of 5 repeats of the yeast "upstream activating sequence" (5x UAS) to which the Gal4-DBD can bind (orange curved arrow). The Gal4-RAR chimeric receptor and the UAS-E4$_{TATA}$::fLuc-EGFP reporter together constitute the novel transcription-based RA reporter system (beige box). **B**, Quantification of GFP fluorescence in HEK 293T cells cotransfected with UAS-E4::fLuc-EGFP reporter and different variations of Gal4-RAR chimeric re-

porter protein is expressed under the control of an adenoviral E4 TATA box minimal promoter and the "upstream activator sequence" (UAS) to which the Gal4-DBD can bind. We combined the TATA box minimal promoter and 5 repeats of UAS to regulate the expression of the luciferase-EGFP reporter protein (UAS-E4$_{TATA}$::fLuc-EGFP). While the Gal4-DBD thus confers the unique DNA-binding properties of the receptor, the RAR-LBD contributes to the ligand specificity. Together with the UAS-E4$_{TATA}$::fLuc-EGFP reporter DNA, the chimeric Gal4-RAR receptor should form a reporter system that specifically and exclusively responds to retinoic acid or potentially other RAR ligands (Figure 3.2A, beige box).

We first tested this reporter system with different variants of Gal4-RAR chimeras with and without the VP16-transactivation domain by cotransfection of reporter and receptor constructs in HEK 293T cells (Figure 3.2B and C). Transfected cells were stimulated by direct application of 250 nM all-*trans* retinoic acid (RA) at 24-48 hours post-transfection. We found that cells transfected with VP16-containing receptors appeared brighter in general, but the high background reporter activity in DMSO-treated control cells partially obscured further reporter activation by RA and thus reduced overall reporter sensitivity. Nevertheless, all but one VP16-containing receptor chimera induced a robust increase of reporter expression in the presence of RA; only the RARβ receptor chimera with the F domain (Gal4-RARbF-VP16) altogether failed to respond to RA (Figure 3.2B). The best responses were obtained with the two receptor constructs Gal4-RARaF-VP16 and Gal4-RARb-VP16, yielding 3-fold and almost 4-fold increases of reporter levels, respectively. Because of the high baseline fluorescence levels caused by the VP16-containing receptor

FIGURE 3.2| **Development of a Novel Transcription-Based RA Reporter System.** (continued)

ceptors, as indicated. Expression levels of cells treated with 250 nM RA for 24h (black bars) were normalized to DMSO controls (white bars; averages ± SEM of 9 images obtained from 3 independent experiments for each group): Gal4-RARα-VP16, 174.14 ± 17.12%; Gal4-RARαF-VP16, 286.77 ± 62.18%; Gal4-RARβ -VP16, 371.38 ± 74.08%; Gal4-RARβF-VP16, 117.28 ± 22.19%; Gal4-RARγ-VP16, 180.49 ± 33.08%; Gal4-RARγF-VP16, 275.69 ± 26.86%; Gal4-RARα, 394.15 ± 124.15%; Gal4-RARαF, 664.48 ± 104.38%; Gal4-RARβ, 273.25 ± 29.41%; Gal4-RARβF, 239.58 ± 43.70%. **C**, Representative images of GFP intensities in reporter-expressing HEK 293T cells. Regions outlined in red were selected by background thresholding for quantification of GFP intensities as shown in panel B. Scale bar, 50 μm.

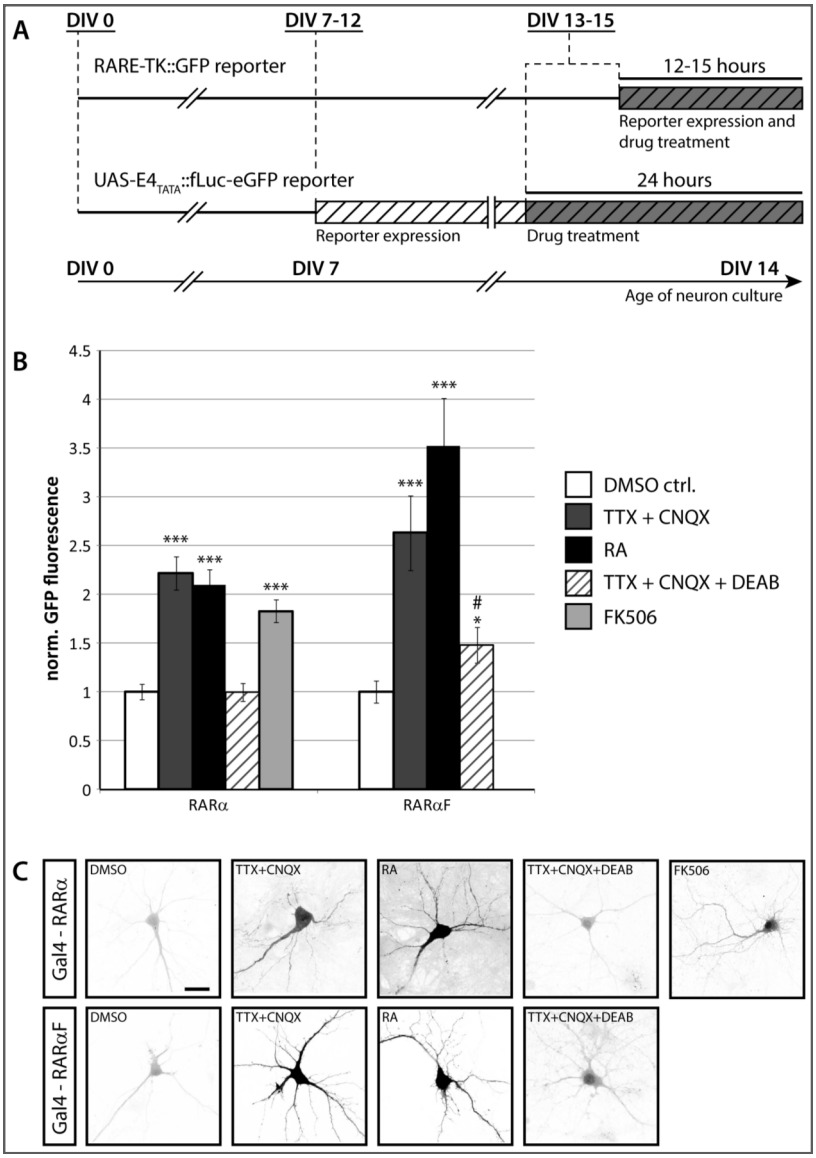


FIGURE 3.3| **UAS-E4::fLuc-EGFP Reporter Activation in Neurons after Calcineurin Blockade. A**, Time course of reporter expression (hatched bars) and drug treatment (shaded bars) compared between RARE-TK::GFP (top) and UAS-E4$_{TATA}$::fLuc-EGFP reporters (bottom). **B**, Quantification of GFP fluorescence in reporter-expressing cultured hippocampal neurons subjected to different drug treatments. Expression levels normalized to DMSO controls are (average ± SEM): *Gal4-RARα receptor*: TTX+CNQX, 221.89 ± 17.17% (N=7, n=103 neurons); RA, 210.00 ± 15.46% (7/103); TTX+CNQX+DEAB, 99.90 ± 9.06% (5/74); FK506, 182.89 ± 11.77% (2/32); *Gal4-RARαF receptor*: TTX+CNQX, 262.98 ± 38.53% (2/26); RA, 351.55 ± 49.43% (2/26); TTX+CNQX+ DEAB, 147.92 ± 18.47% (2/32). **P* < 0.05; ****P* < 0.001; #*P* < 0.01 (*Gal4-RARαF receptor*: TTX/CNQX/DEAB *vs.* TTX/CNQX groups) student's t-test. **C**, Sample images of GFP intensities in reporter-expressing neurons. Scale bar, 15 μm.

chimeras even in the absence of RA, we next tested the four receptor chimeras derived from RARα and RARβ without the VP16-transactivation domain. This modification improved the relative RA-induced response generated by the Gal4-RARa and the Gal4-RARaF receptor chimeras without the VP16-transactivation domains which yielded a 4-

fold and 6.5-fold increase of reporter expression upon RA-stimulation, respectively. By contrast, the RA-stimulated responses induced by RARβ-derived receptor chimeras did not improve after removal of the VP16-transactivation domain. (Figure 3.2B).

Having established the RA responsiveness of our chimeric reporters in HEK 293T cells, we examined the two most responsive constructs in neurons to test whether responsiveness could be maintained over extended times of reporter expression. We therefore cotransfected the UAS-E4$_{TATA}$::fLuc-EGFP reporter with either the Gal4-RARa or the Gal4-RARaF receptor chimeras into dissociated hippocampal neurons between 7 and 12 days *in vitro* (DIV), and tested the responsiveness of the reporter between 3 and 5 days post-transfection (DIV 13-15, Figure 3.3A). Our data show that reporter-expressing neurons are highly responsive to direct treatment with RA, as well as RA-inducing neuronal activity blockers; reporter activation could also be blocked with DEAB (Figure 3.3B and C). Moreover, the responses obtained with the UAS-E4$_{TATA}$::fLuc-EGFP reporters are comparable to results from our previously established RARE-TK::GFP reporter assay (*cf.* Figure 3.1B). Consistent with our observations in HEK 293T cells, the RARα-derived receptor chimera including the F-domain yielded the strongest response to RA or RA-inducing drug treatments. Compared to the DMSO-treated control group, the Gal4-RARaF chimera yielded a 3.5-fold higher GFP expression level in RA-treated neurons. The increase of GFP expression in TTX/CNQX-treated neurons was 2.6-fold of DMSO baseline level and could be reduced to 1.5-fold of baseline ($p = 0.03$) by the addition of DEAB, an inhibitor of RA-synthesizing enzymes of the RALDH family. The Gal4-RARa chimera without the F-domain yielded a 2.1-fold increase of GFP expression with RA. The 2.2-fold increase induced by treatment with TTX/CNQX could be completely blocked when DEAB was coapplied ($1.00 \pm 0.09$; $p = 0.99$). We also tested the Gal4-RARa chimeric reporter response to the calcineurin inhibitor FK506 and found a 1.8-fold significant increase of GFP expression in FK506-treated cells. All treatments yielded statistically highly significant results ($p < 0.0005$), except where otherwise stated.

## 3.3 Designing Modular FRET Sensors for RA

After having established calcineurin inhibition as another step of the biochemical cascade preceding the production of RA during homeostatic synaptic plasticity, we wondered how RA synthesis is regulated in time and space with respect to subcellular neuronal compartments and biochemical or signaling events. The overarching question is whether RA is produced globally or at defined subcellular compartments such as specific dendritic branches. To address the question of speed and location of RA synthesis upon synaptic activity blockade, we needed a tool that could indicate the concentration of RA with a high spatiotemporal resolution. We therefore aimed to develop a FRET-based RA reporter that would sense and indicate the presence of RA in real-time with a subcellular spatial resolution.

Our first approach was to develop a FRET sensor for RA according to a modular design as suggested by Umezawa and colleagues, whose concept exploited the fact that nuclear receptors such as estrogen receptor can recruit transcription co-activators upon activation by their ligands (Awais *et al.*, 2004). The authors constructed a chimera protein consisting of the nuclear receptor itself (estrogen receptor in their case) linked to a NR box, the binding motif found in a transcriptional co-activator. The NR box is separated from the nuclear receptor by a flexible linker domain. Additionally, a YFP is tagged to the N-terminal, and a CFP to the C-terminal end of the chimera. In this modular protein, the nuclear receptor co-factor binding motif acts as an intramolecular tethered ligand: In the presence of receptor agonist, the tethered ligand binds to the nuclear receptor, positioning the YFP and CFP in close proximity to one another to yield a significant increase in the observed FRET signal. In analogy to the estrogen receptor-based design of Umezawa and colleagues, we developed a FRET sensor based on retinoic acid receptor alpha (RARα), because within the retinoid receptor protein family RARα has the highest affinity for all-*trans* retinoic acid (Repa *et al.*, 1993) (Figure 3.4A, top panel). Similar to Umezawa's construct, our reporter should undergo a conformational change that increases FRET upon ligand binding (Figure 3.4B, bottom panel). The "NR box" is a conserved

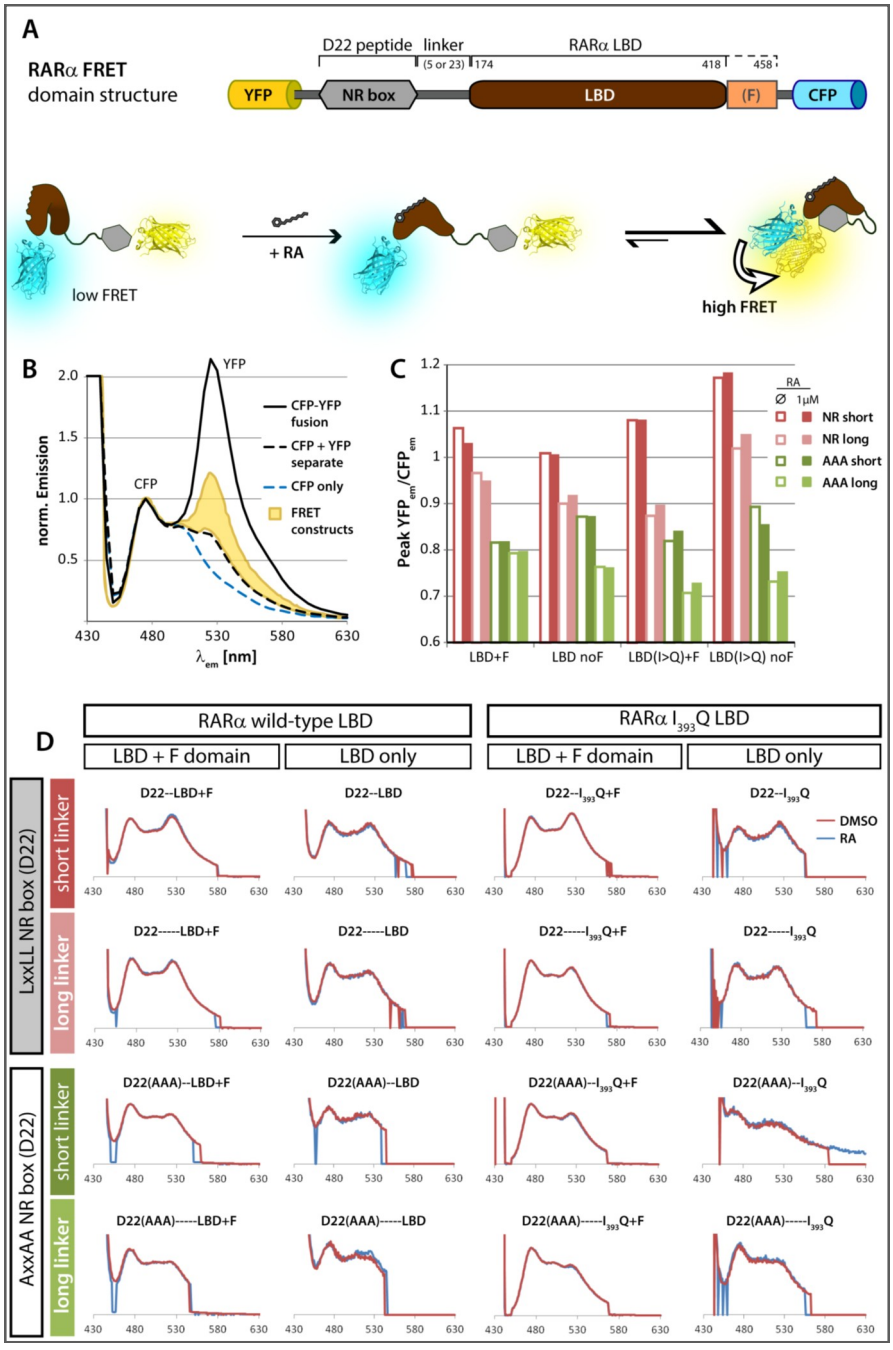


FIGURE 3.4| **Designing Modular FRET Sensors for RA. A**, Construct design for a modular FRET sensor for RA. Top panel illustrates the domain structure of modular FRET sensors: Mouse RARα LBD was connected by a linker domain to a cofactor binding motif (NR box). YFP and CFP are fused to the N- and C-terminals, respectively, allowing the detection of FRET. Linker lengths and residue positions of RARα LBD fragments (referring to full-length rat RARα) are indicated above. Bottom panel illustrates the principle of RA detection. In the absence of RA, the detector assumes an extended conformation, and CFP and YFP are far apart. When RA is bound, the RARα LBD can recruit the tethered NR box, bringing CFP and YFP into close proximity, thereby increasing FRET (white curved arrow). **B**, Emission spectra obtained between 430 nm - 630 nm from lysates of HEK cells expressing FRET constructs illustrated in panel A. Spectra were obtained under specific CFP excitation at 434 nm and showed clearly distinguishable CFP and YFP emission peaks at 477 nm and 527 nm, respectively. Spectra were overlayed after normalization to CFP peak emission at 477 nm; lysates containing separately expressed CFP and YFP (black dashed line) or

interaction motif of transcriptional co-activators containing a consensus "LxxLL" amino acid sequence, where L indicates leucine and x indicates any amino acid (Heery *et al.*, 1997). A comparison of a number of natural and synthetic NR box peptides and their binding behavior to liganded and unliganded nuclear receptors revealed a peptide termed "D22" that shows the best differential binding behavior between unliganded RARα (very little binding) and liganded RARα (very strong binding) (Chang *et al.*, 1999). Mutating the essential leucines within the NR box consensus motif to other amino acids abolishes the ability to bind nuclear receptors. Hence, leucine-to-alanine "AxxAA" mutants of the D22 peptide could serve as powerful negative controls for the construct function.

Based on the general design principle mYFP-NR box-linker-RARα(LBD)-mCFP (Figure 3.4A), we obtained 8 constructs with their respective "AxxAA" negative controls. We chose to examine 3 parameters for their influence on FRET efficiencies of the constructs: 1. linker length (short linker, 5 amino acids: GGNGG; or long linker, 23 amino acids: $[GGN]_7GG$), 2. the F-domain (RARα LBD with or without F-domain), and 3. a beta sheet-destabilizing RARα LBD $I_{393}Q$ point mutation (RARα LBD wt or RARα LBD $I_{393}Q$). The latter mutation renders the LBD incapable of binding nuclear co-repressors (le Maire *et al.*, 2010), thereby potentially enhancing its ability to differentially bind the tethered intramolecular D22 NR box peptide.

To test whether these reporter constructs could respond with an increase of FRET efficiency when RA is added, we obtained crude protein extracts from HEK 293T cells expressing the constructs. Using a spectrophotometer, the lysates were excited with 415 nm

FIGURE 3.4| **Designing Modular FRET Sensors for RA.** (continued)

a CFP-YFP fusion protein (black solid line) served as FRET negative and positive controls, respectively; emission of CFP alone is plotted for comparison (dashed blue line). YFP emission of modular RA sensors falls in between FRET negative and positive controls (beige shaded area). **C**, Lysates of HEK cells expressing different FRET sensor variants based on the design principle illustrated in panel A were tested by spectrophotometry as described in panel B. Bar graph shows YFP peak emission at 527 nm in spectra normalized to CFP peak emission at 477 nm. White and colored bars represent ratios determined in the absence or presence of 1 μM RA, respectively. Red and green bars refer to constructs containing the LxxLL wild type NR box or the AxxAA binding-incompetent NR box, respectively, and darker and lighter hues indicate short (5 residues) or long linkers (23 residues), respectively, between the RARα LBD and the NR box. **D**, Overlays of emission spectra for all tested constructs without (red line) or with 1 μM RA (blue line).

light, and emission spectra were obtained between 430 nm and 630 nm in 5 nm steps. The emission spectra we obtained from our FRET constructs exhibit two peaks, one CFP emission peak at 475 nm and a YFP emission peak at 530 nm. We plotted the spectra and normalized the emission values to the CFP peak at 475 nm (Figure 3.4B). Because 415 nm excitation excites CFP without directly causing YFP excitation, we can assume that the emission spectra reflect directly excited CFP with its emission peaking at 475 nm, and the YFP indirectly excited from CFP through FRET, with YFP emission peaking at 530 nm. This assumption was confirmed by obtaining emission spectra from lysates of cells coexpressing CFP and YFP as separate proteins where no FRET is expected to occur between the fluorophores. In this lysate the 530 nm YFP peak is indeed reduced to a barely noticeable shoulder on top of the CFP emission spectrum (Figure 3.4B, dashed black line). When we measured spectra from cells expressing a CFP-YFP tandem fusion protein with high expected FRET efficiency between the fluorophores, we detected a very high YFP peak (Figure 3.4B, solid black line). The YFP emission peaks of all our RARα-derived FRET constructs fall in between the CFP + YFP (no FRET) value and the CFP-YFP tandem protein (high FRET) value and can therefore be considered to represent intermediate FRET efficiencies (Figure 3.4B, beige shaded area).

All spectra obtained from our RARα-derived FRET constructs exhibit intermediate FRET values for the wild-type NR box-containing constructs, while their inactive AxxAA NR box mutants consistently show less FRET than their LxxLL counterparts. We also noticed that FRET decreased with increasing linker length between the fluorophores, and observed a general trend that the FRET efficiencies for any variant of the RARα LBD ranged in the order LxxLL (short linker) > LxxLL (long linker) > AxxAA (short linker) > AxxAA (long linker) (Figure 3.4C and D). The FRET efficiency thus showed a clear correlation with the linker length separating the NR box from the RARα LBD. The other two factors we examined, F-domain and $I_{393}Q$ mutation, had a less pronounced effect on FRET efficiencies. While the presence of the F-domain very mildly increased FRET efficiency in the wild-type RARα LBD construct, it decreased FRET efficiency in the RARα

LBD $I_{393}Q$ mutants. Despite the differences in FRET efficiencies between the various constructs we tested, none of our constructs showed by itself a response to RA beyond the variability within the assay (Figure 3.4C and D). While the YFP emission peaks of the AxxAA constructs are reduced by around 10% - 20% compared to their LxxLL counterparts, the RA-induced differences we observed for any construct were consistently below 5%. Moreover, the FRET changes we observed with the active LxxLL NR box constructs appeared generally similar in magnitude to their inactive AxxAA counterparts. Importantly, the expected change with the addition of RA would be a FRET increase, but we observed random changes, including increases and decreases, of FRET efficiencies upon RA addition to our constructs (Figure 3.4C). The reason why none of our various constructs respond to RA remains obscure; reduced FRET in the AxxAA mutants as compared to the LxxLL wild-type NR box constructs indicates that specific interaction between the RARα LBD and the NR box does indeed occur. Interestingly, a commercial kit (LanthaScreen, ThermoFisher #PV4409) to probe RARα ligands for coactivator recruitment is reported to exhibit clear RA-dependent binding of the D22 peptide to the RARα LBD with components almost identical to the domains included in our FRET sensor, though the commercial kit uses the RARα LBD in combination with a molecularly separated D22 NR box peptide instead of intramolecular FRET.

## 3.4 aGEPRA RA Reporter Activity in Living Hippocampal Neurons

It has been firmly established that retinoic acid is both necessary and sufficient for a specific form of homeostatic synaptic plasticity (HSP). An important open question is when and where exactly within a neuron the synthesis and release of RA take place. The answer to this question is not only relevant to understand RA-mediated HSP, but would also allow a deeper understanding of the mechanisms of HSP in general, specifically how "local" (e.g. single dendritic branches) or "global" (i.e. involving the entire neuron) the homeostatic regulation of synaptic strength within a given neuron can be.

Because none of our own FRET-based sensor designs responded to RA (Figure 3.4),

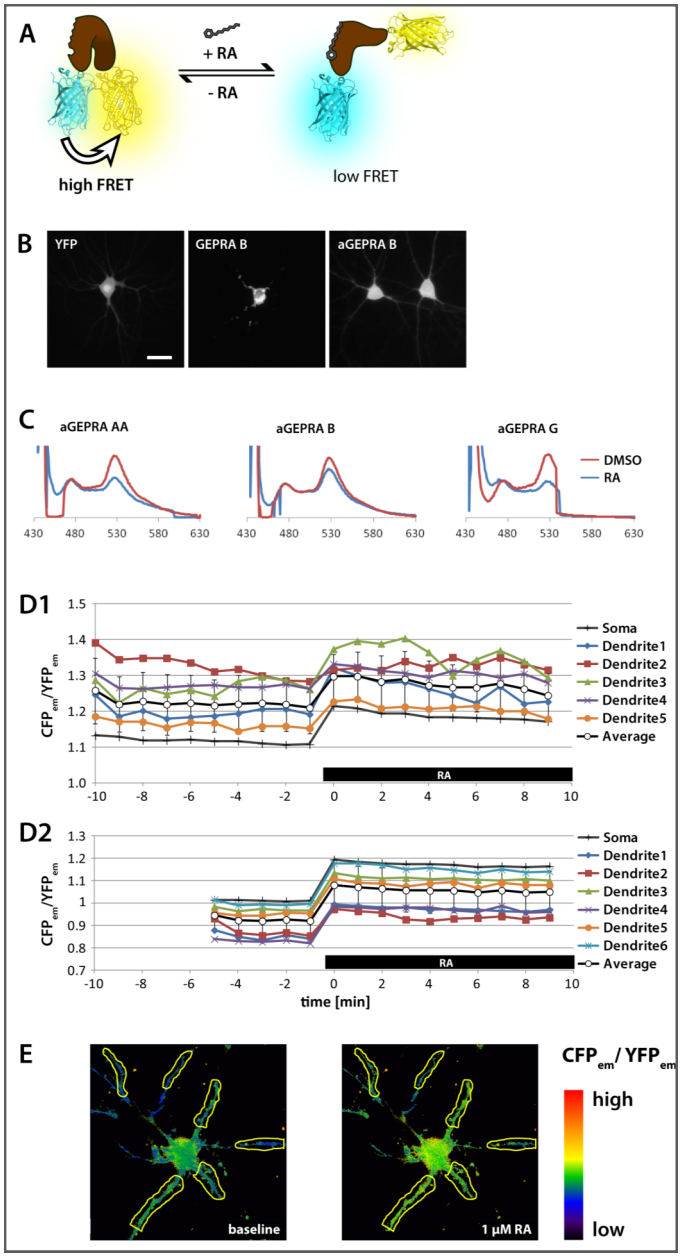


FIGURE 3.5| **GEPRA RA FRET Sensor Expression in Hippocampal Neurons. A**, Principle of GEPRA FRET sensors for RA showing high FRET in the absence of RA and low FRET after RA binding (Shimozono *et al.*, 2013). **B**, Toxicity of GEPRA FRET sensors is illustrated by unhealthy morphology and fluorescent aggregates forming inside GEPRA-expressing neurons (middle panel), as opposed to a YFP-expressing control neuron (left panel). GEPRA sensors were modified by adding an N-terminal solubility domain to generate aGEPRA. Toxicity of aGEPRA was greatly reduced as demonstrated by healthy morphology of aGEPRA-expressing neurons (right panel). Scale bar, 20 µm. **C**, Overlays of emission spectra from HEK cell lysates were obtained as described in Fig. 3.4B. Spectra obtained from all aGEPRA constructs without (red line) or with 1 µM RA (blue line) show reduced YFP emission after addition of RA, indicating lower FRET in the presence of RA. **D**, Example $CFP_{em}/YFP_{em}$ ratio traces obtained from two aGEPRA B-expressing neurons by life cell confocal microscopy. Acute administration of 1 µM RA evokes an immediate response in $CFP_{em}/YFP_{em}$ ratio of the FRET sensor in the soma and all dendrites. **E**, Heat map sample images before (left panel) and after addition of 1 µM RA (right panel) of the neuron shown in panel D2 clearly illustrate a response to RA throughout the entire cell.

we used a different, recently published FRET-based RA sensor termed "Genetically Encoded Probe for RA", or GEPRA, to localize RA concentrations within living neurons (Shimozono *et al.*, 2013). GEPRA is a fusion protein where a retinoic acid receptor ligand-binding domain is directly sandwiched between CFP4 and cpYPet (a CFP variant, and a circularly permuted YFP variant, respectively). In contrast to our modular FRET sensor design, GEPRA responds to RA with a decrease in FRET efficiency (Shimozono *et al.*, 2013) (Figure 3.5A). Expression of GEPRA in dissociated hippocampal neurons was not possible because of the toxicity of the sensor protein, evidenced by morphological changes, fluorescent aggregates near the nucleus, and eventual cell death (Figure 3.5B). Miyawaki *et al.* therefore introduced an N-terminal solubility domain to facilitate solubility of the protein in mammalian neurons, and termed the new construct "aGEPRA" (Figure 3.5B). aGEPRA responsiveness to RA was first confirmed by analyzing crude lysates from aGEPRA-expressing HEK cells by spectrophotometry; the FRET efficiency decreases upon RA addition to the lysates, which is reflected by a decrease of YPet peak emission relative to the normalized CFP peak emission (Figure 3.5C). To further test how aGEPRA responds to RA in the context of an intact neuron, we transfected dissociated hippocampal neurons with aGEPRA B (the RARβ-derived variant of aGEPRA) and recorded CFP and YPet fluorescence emission while only exciting CFP directly with 458 nm laser light. We calculated the $CFP_{em}/YFP_{em}$ ratio image on a pixel-by-pixel basis. We selected dendritic regions of interest and the soma to plot $CFP_{em}/YFP_{em}$ ratios over time (Figure 3.5D and E). When neurons transfected with aGEPRA B were incubated with 1 µM RA, the $CFP_{em}/YFP_{em}$ ratio increased by about 10% both in the soma and in the dendrites, as shown in the plots (Figure 3.5D) and the ratiometric $CFP_{em}/YFP_{em}$ ratio images (Figure 3.5E).

We next proceeded to transfect aGEPRA G (a RARγ-derived GEPRA variant) into dissociated hippocampal rat neuron cultures between 10 and 14 days *in vitro* to observe cellular RA concentration in living cells while pharmacologically blocking synaptic transmission. 2 days post-transfection, we added a synaptic activity blocking TTX/CNQX

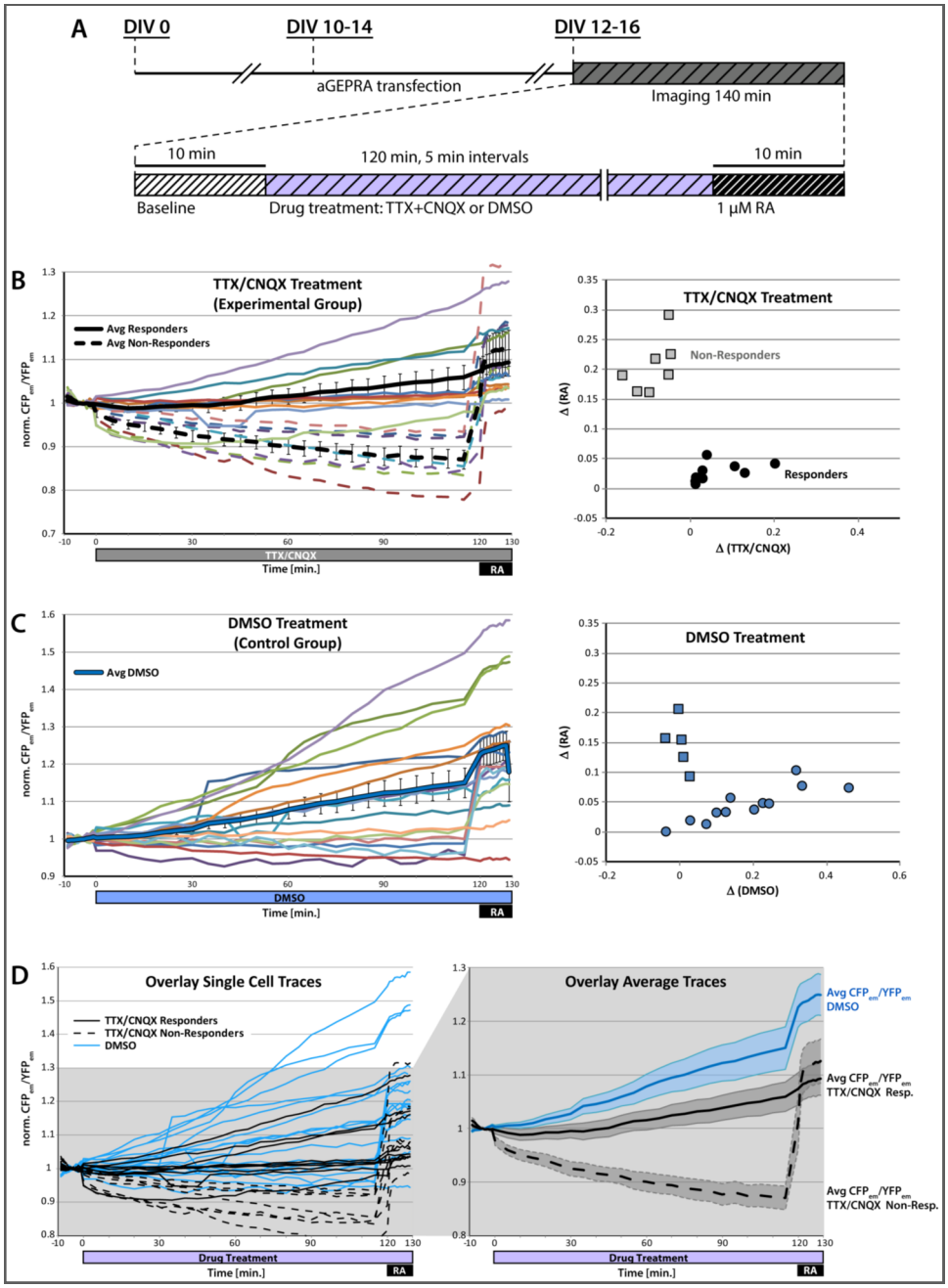


FIGURE 3.6| **aGEPRA RA Reporter Activity in Living Hippocampal Neurons. A**, Time course of aGEPRA transfection (top panel) and imaging (bottom panel) of dissociated hippocampal neurons. Neurons were imaged for 120 minutes at a 5 min. image acquisition rate in the presence of TTX/CNQX to block synaptic transmission or DMSO as a control. Application of 1 µM RA at the end of each imaging session was to test for sensor saturation. **B**, $CFP_{em}/YFP_{em}$ ratios were recorded for individual TTX/CNQX-treated neurons and baseline-normalized ratios were plotted (left panels). TTX and CNQX were present during the entire imaging period of 130 min. as indicated below each plot. RA was supplied for the last 10 minutes in addition to TTX and CNQX which remained in the bath. Two subgroups of cells responding differently to drug treatments became apparent: "non-responders" (dashed lines) showed declining $CFP_{em}/YFP_{em}$ ratios during TTX/CNQX treatment and a sharply increasing $CFP_{em}/YFP_{em}$ ratios after RA administration, "responders" (solid lines) showed constant or increasing $CFP_{em}/YFP_{em}$ ratios during TTX/CNQX treatment

cocktail to the cultures while observing aGEPRA G-expressing neurons by fluorescence microscopy in real time over 120 minutes. Our imaging protocol included a sequence of 10 baseline images (1 min. intervals) followed by addition of drugs (either activity blockers TTX + CNQX or vehicle control DMSO) and recording fluorescence images in 5 min. intervals over 120 minutes. To test whether the FRET sensor was saturated by RA at the end of the imaging session, we last added 1 µM RA and recorded another 10 images, again at 1 min. intervals (Figure 3.6A). Because changes in intracellular RA concentrations $[RA]_i$ should proportionally translate into changes of the $CFP_{em}/YFP_{em}$ ratio in aGEPRA G-expressing cells, we plotted the baseline-normalized $CFP_{em}/YFP_{em}$ ratios recorded from each cell to visualize $[RA]_i$ changes while synaptic activity-blocking drugs or DMSO as a vehicle control were applied to the cultures (Figure 3.6B and C, left panels).

We could classify cells treated with TTX/CNQX into two distinct subgroups based on their $CFP_{em}/YFP_{em}$ time courses: in 9 of 16 recorded cells (56% of cells) formed the first subgroup, exhibiting continuously increasing $CFP_{em}/YFP_{em}$ during the treatment period, while the 7 cells (44%) forming the second subgroup showed a $CFP_{em}/YFP_{em}$ ratios (Figure 3.6B, left panel). Moreover, the group 2 cells responded with a strong increase when 1 µM RA was applied at the end of the imaging session, while group 1 cells showed little or no response to 1 µM RA treatment. The separation of the two groups became even clearer when the relative changes of the aGEPRA sensor "RA response" (i.e. the dif-

FIGURE 3.6| **aGEPRA RA Reporter Activity in Living Hippocampal Neurons.** (continued)

without appreciable responses to the final administration of RA. ΔRA *vs.* ΔTTX/CNQX and ΔRA *vs.* Δ DMSO plots (right panel) were generated by plotting the differences observed during 120 minutes drug treatment (average of the first minus average of last three images obtained during drug administration) against the differences induced by acute administration of RA (last three images before RA minus last three images after RA). Groups of "non-responders" (gray squares) and "responders" (black circles) are clearly separated. **C**, Same as panel B, but with DMSO treatment instead of TTX/CNQX treatment. No DMSO-treated cell showed a decline in $CFP_{em}/YFP_{em}$ ratio, and only few cells responded moderately with an increase of $CFP_{em}/YFP_{em}$ ratio after RA was added at the end of the imaging session (blue squares in right panel). **D**, Overlay of $CFP_{em}/YFP_{em}$ ratios from individual cells of all treatment groups, color coded by drug treatment and response group. Traces show partial overlap between TTX/CNQX "responder" group (solid black lines) and DMSO-treated control group (blue lines), but both groups are clearly separated from cells of the TTX/CNQX "non-responder" subgroup (dashed black lines). Averages (right panel, averages ± SEM [shading]) show clear separation between all groups.

ference between $CFP_{em}/YFP_{em}$ ratio after the addition of RA compared to the time points immediately before RA application) was plotted against the relative change of the "drug response" (i.e. the values at the end of the drug treatment compared to the values at the beginning of drug treatment) (Figure 3.6B, right panel). We therefore termed the two groups "responders" (subgroup 1) and "non-responders" (subgroup 2), according to the responses of the aGEPRA G sensor signals during TTX/CNQX administration. "Responders" showed an increase in $[RA]_i$ which presumably reached saturating levels of the aGEPRA G dynamic range such that the sensor signal could not be further increased by exogenously applied RA, while "non-responders" showed no increase or, perhaps, a decrease in $[RA]_i$.

When we applied DMSO as a vehicle control to another set of cells, we observed different responses (Figure 3.6C). The most obvious difference was that all cells responded with an increasing or at least stable $CFP_{em}/YFP_{em}$ ratio while none of the DMSO-treated cells showed an appreciable decrease in $CFP_{em}/YFP_{em}$ ratio (Figure 3.6C, left panel); only 29% of the cells (5/17) showed a marked response when 1 µM RA was added at the end of the imaging session (Figure 3.6C, right panel, squares). These observations resemble the responses of the "responder" group of TTX/CNQX-treated cells. The overlay of the TTX/CNQX- and DMSO-treated cells shows that the two groups differ considerably. Most individual cell traces from the DMSO group fall within the same range as the increases observed for the "responder" group of the TTX/CNQX-treated cells, but the average increase in $CFP_{em}/YFP_{em}$ ratio in the DMSO group is higher than in the TTX/CNQX-treated cells (Figure 3.6D).

To exclude the possibility that photobleaching might have contributed to the differences between TTX/CNQX-treated and DMSO-treated cells, we plotted the average traces of individual fluorescence channels to compare how they differed between groups. The changes observed in single channels are consistent with $CFP_{em}/YFP_{em}$ ratio changes. The TTX/CNQX "non-responder" group exhibited a roughly constant CFP fluorescence and a parallel YFP fluorescence in the FRET channel, and the strong increase in $CFP_{em}/YFP_{em}$

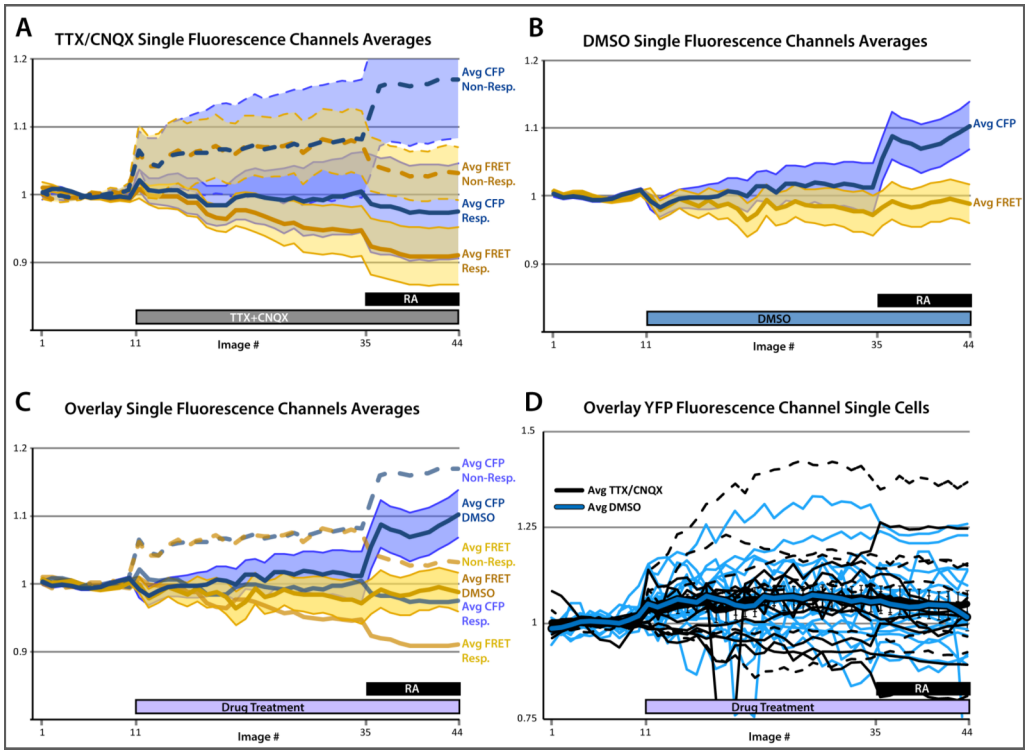


FIGURE 3.7| **Photobleaching Cannot Explain Different aGEPRA G Responses between Treatment Groups. A**, Averages of individual fluorescence channels (CFP emission and FRET channels) obtained from TTX/CNQX-treated groups were plotted against image number, separated between "non-responder" and "responder" subgroups. Both groups exhibited signal fluctuation of less than 10% in either channel; the parallel changes apparent both channels occuring at the time of TTX/CNQX application in the "non-responder" subgroup were likely due to minor changes in focal planes of the sample cells caused by manual drug administration. **B**, Same as panel A, but for DMSO-treated group. Again, signals remained stable within a ±10% window around baseline. **C**, Overlay of channels obtained in all groups shows overall conformity and stability for signals in all groups. **D**, Overlay of YFP fluorescence channel signals (YFP emission under direct YFP excitation) from individual cells of all treatment groups, color coded by drug treatment and response group. TTX/CNQX "non-responders" and "responders" (dashed and solid black lines, respectively) as well as DMSO-treated cells (blue lines) all fall within a completely overlapping region of signal fluctuation. Averages of TTX/CNQX and DMSO groups (thick black and blue traces, respectively) are virtually identical and show no signs of photobleaching during the time course of image acquisition. Traces and shaded areas represent averages ± SEM for all plots.

ratio after RA addition is well reflected by the increase in CFP emission with a concomitant decrease in the YFP (FRET) channel. The TTX/CNQX "responder" group however showed a constant CFP emission with a slight decrease in YFP (FRET) channel signal, but both channels showed a parallel decrease after RA addition, thus not altering $CFP_{em}$/$YFP_{em}$ ratio any further (Figure 3.7A). The DMSO-treated cells exhibited roughly constant levels of both CFP and YFP (FRET) emission over the course of the treatment, again the slight increase of CFP emission with a reduction of YFP (FRET) emission reflecting the increase of the $CFP_{em}/YFP_{em}$ ratio. CFP emission increased by about 9% after

RA addition without detectable changes in average YFP (FRET) emission signal, consistent with a noticeable average increase in $CFP_{em}/YFP_{em}$ ratio after RA addition (Figure 3.7B). An overlay of all fluorescence channels of all groups demonstrates that averages of individual fluorescence channels fluctuate within a range of ± 10% around the normalized baseline intensity (Figure 3.7C). Because the CFP and YFP (FRET) channels both are directly influenced by FRET, they do not reliably reflect the direct contribution of photobleaching. We thus also recorded a YFP fluorescence channel where YFP is directly excited by a 514 nm laser and the YFP emission signal is detected with the same emission settings as used for the FRET channel. We plotted this YFP emission signal for each cell over the time course of the imaging sessions and calculated the averages for all three groups (TTX/CNQX responders, TTX/CNQX non-responders, DMSO control group). Figure 3.7D clearly shows that all individual cells show fluorescence levels that scatter within a range of ± 25% around the normalized baseline intensity, with only two outliers showing an increase of up to 40% of YFP fluorescence. This figure also demonstrates that no photobleaching occurred during the imaging, as average YFP fluorescence rather increased by about 10% throughout the imaging session, with TTX/CNQX-treated and DMSO-treated cells showing virtually identical traces (Figure 3.7D).

## 3.5 Ratiometric FRET Measurements by Two-Photon Microscopy

Two-photon excitation comes with the advantage of deeper tissue penetration with less scattering and out-of-focus photobleaching compared to single-photon excitation, thereby allowing for the observation of neurons in semi-intact thick tissue sections with preserved circuitry, or even *in vivo*. However, two-photon excitation is modulated by tuning the excitation laser wavelength and collecting the emitted fluorescence through fixed filter sets. Since many fluorescent proteins have broad single-photon excitation spectra, and even broader two-photon excitation spectra, the advantages of two-photon laser excitation may come at the cost of substantial crosstalk between different FRET fluorophores, thus limiting the feasibility of ratiometric FRET measurements.

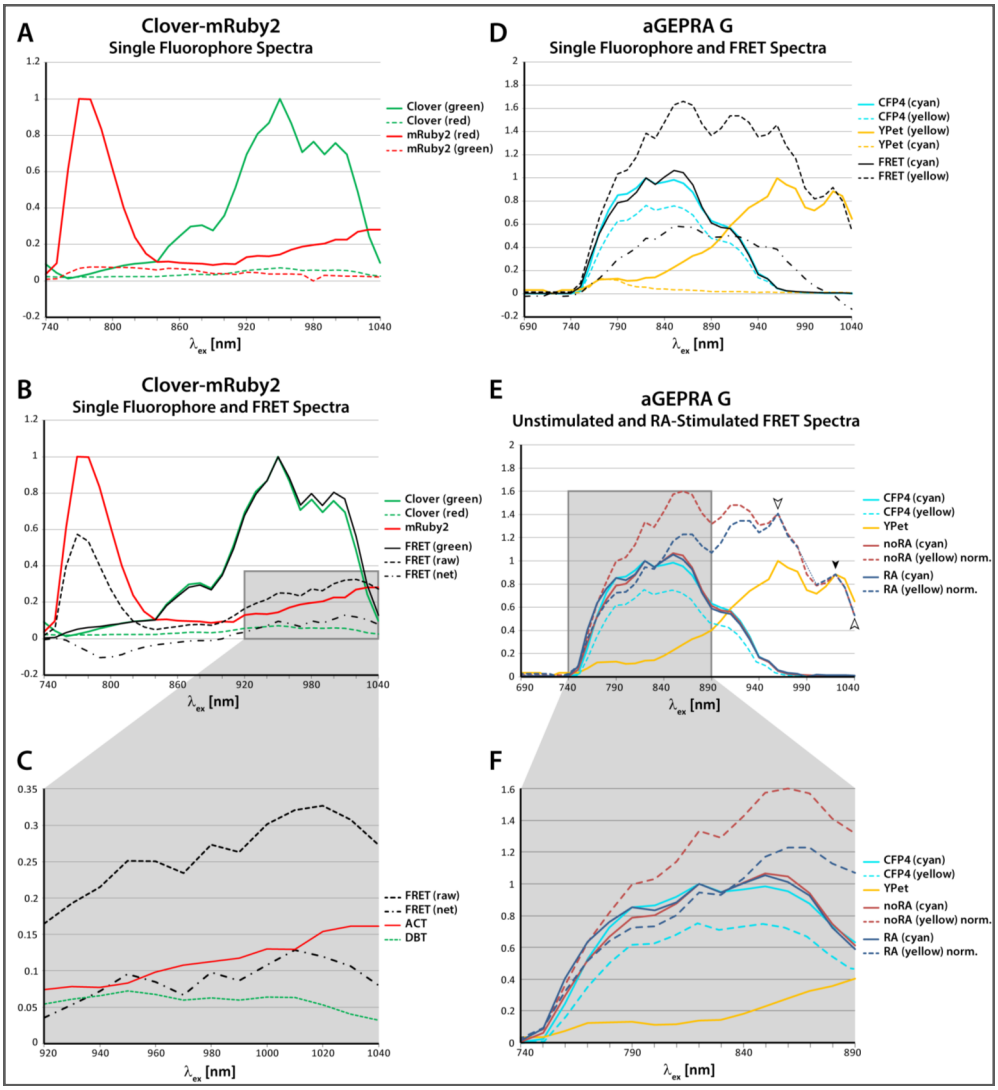


FIGURE 3.8| **Ratiometric FRET Measurements by 2-Photon Microscopy. A-C**, excitation spectra of Clover, mRuby2, and Clover-mRuby2 fusion protein obtained between 740 nm and 1040 nm. Spectra for both fluorophores were normalized to excitation maxima in the appropriate emission channels (solid green and red lines), and Clover-mRuby2 fusion protein excitation spectrum was normalized to Clover excitation maximum at 940 nm (solid black lines). Bleed-through spectra obtained for all fluorophores in the opposite emission channel was scaled according to scaling factors applied for normalization in the first channel. Panel C shows a magnification of the signals between 920 nm and 1040 nm relevant for the calculation of FRET contribution to total donor emission signal; see main text for detailed calculations. Filter sets for emission were 525/70 (Clover) and 607/45 (mRuby2), separated by a 575 dichroic. **D-F**, Same as A-C, but with excitation spectra obtained between 690 nm and 1040 nm for CFP4, YPet, and the aGEPRA G FRET sensor. Normalization was performed as described for panels A-C, except that spectra obtained in the YPet channel for the FRET construct were normalized to the secondary YPet emission peak at 1020 nm. Panel F shows a magnification of the signals between 740 nm and 890 nm which are relevant for FRET observation. Filter sets for emission were 480/40 (CFP4) and 535/50 (YPet), separated by a 505 dichroic.

We therefore wanted to explore the possibility of ratiometrically measuring FRET efficiencies with direct two-photon excitation of the donor fluorophore. Our FRET probe for RA, aGEPRA, is based on the CFP/YPet FRET pair which emit in cyan and yellow, respectively. However, we first wanted to observe FRET with the spectrally better separated Clover/mRuby2 FRET pair (green/red) to minimize the potential problems of channel crosstalk (Lam *et al.*, 2012). In order to observe FRET from the Clover/mRuby2 FRET pair, we measured cells separately expressing each individual fluorophore and cells expressing a tandem fusion between the Clover FRET donor and mRuby2 FRET acceptor (Clover-mRuby2) that should yield substantial FRET to serve as a positive control.

We first confirmed low spectral excitation overlap in the 2-photon excitation mode for the Clover/mRuby2 FRET pair. We found that mRuby2 is directly excited mostly at wavelengths between 760 nm and 810 nm whereas Clover is excited mostly between 920-980 nm (Figure 3.8A). We next tested the Clover-mRuby2 tandem fusion construct as a FRET positive control to compare its excitation spectrum with the two single fluorophores. The excitation spectra of the fusion protein grossly resemble the individual green and red fluorophores with the major difference that fluorescence in the red emission channel is increased in the longer wavelength region of 920-1040 nm when compared to the mRuby2 alone (Figure 3.8B). Because direct excitation of the Clover FRET donor is very efficient and direct mRuby2 FRET acceptor excitation is low in this spectral region, these longer excitation wavelengths provide favorable conditions for calculating FRET efficiency. Generally, emission in the FRET channel needs to be corrected for donor bleed-through (DBT) and acceptor cross talk (ACT) to estimate the net FRET value:

$$net\ FRET = FRET(raw) - DBT - ACT$$

The large spectral separation of the Clover/mRuby2 FRET pair allows for specific excitation of either FRET donor or FRET acceptor at specific wavelengths, and the wavelength-specific contributions of $DBT_\lambda$ and $ACT_\lambda$ can be approximated by two formulas as below:

$$DBT_\lambda = FRET(raw)_\lambda \cdot \frac{Clover(red)_\lambda}{Clover(green)_\lambda}$$

where $DBT_\lambda$ is the excitation wavelength-specific donor bleed-through into the FRET emission channel. $FRET(raw)_\lambda$ represents the emission of the FRET construct into the green emission channel at the specific excitation laser wavelength, and $Clover(red)_\lambda$ and $Clover(green)_\lambda$ represent the emissions of Clover alone into the red and green emission channels, respectively, under excitation at the specific laser wavelength. At wavelengths between 860 nm and 1040 nm where mainly the Clover FRET donor is excited, the donor bleed-through of the FRET construct should be the same as the bleed-through of only Clover into the FRET emission channel which can be calculated for any wavelength and then scaled by the signal intensity in the green channel obtained for the actual FRET construct at that wavelength.

$$ACT_\lambda = mRuby2(red)_\lambda \cdot \frac{FRET(red\_raw)_{770nm}}{mRuby2(red)_{770nm}}$$

where $ACT_\lambda$ is the excitation wavelength-specific acceptor crosstalk, or direct excitation of the FRET acceptor by the respective two-photon laser wavelength. $mRuby2(red)_\lambda$ is the emission of mRuby2 alone when excited at the specific laser wavelength, and $FRET(red\_raw)_{770nm}$ and $mRuby2(red)_{770nm}$ represent the emissions in the red channel of the FRET construct, and mRuby2 alone, respectively, at 770 nm laser excitation wavelength where only specific mRuby2 excitation occurs without direct Clover excitation. The red channel emission signal at 770 nm excitation is purely contributed by mRuby2 emission; scaling the mRuby2 excitation spectrum to the emission recorded from the FRET construct at 770 nm excitation should therefore be a good estimate for mRuby2 crosstalk at any excitation wavelength throughout the FRET spectrum.

According to our calculations, FRET contributed approximately 30% to the total emission in the red channel between 920 nm and 1040 nm where mostly the Clover FRET donor is directly excited (Figure 3.8C, compare dash-dotted net FRET line to dashed raw FRET line).

On the contrary, the broad excitation spectra of CFP4 and YPet exhibit substantial overlap, leading to a unimodal emission spectrum of the examined CFP4-YPet fusion

construct (which is our FRET probe aGEPRA G) and thus impeding quantification of FRET (Figure 3.8D). Nevertheless, there is a spectral region between 760 nm and 880 nm where predominantly CFP4 excitation occurs with only minor direct excitation of YPet, offering acceptable conditions for ratiometric FRET measurements. It is noteworthy that with the fluorescence emission parameters chosen for this experiment, the CFP4 fluorophore did cause a substantial bleed-through into the yellow emission channel (compare dotted and solid cyan lines in Figure 3.8D-F).

We next wanted to test whether we were able to measure ratiometric changes in FRET efficiency of our aGEPRA G FRET sensor under 2p laser excitation. The aGEPRA sensor exhibits high FRET under basal conditions and responds with a decrease in FRET efficiency in the presence of RA (*cf*. Figure 3.5C). To test whether we could observe changes in FRET ratio under 2p laser excitation, we obtained the 2p laser excitation spectra of cells expressing aGEPRA in the absence and in the presence of 1 µM RA (Figure 3.8E and F).

To better visualize the differences between unstimulated and RA-stimulated aGEPRA G-expressing cells, we normalized the FRET excitation spectra to the YPet excitation peak at 1020 nm where no direct CFP4 excitation is detectable (Figure 3.8D, solid arrowhead). The stimulated and unstimulated FRET excitation curves overlap completely in the excitation region between 960 nm and 1040 nm where only direct YPet excitation occurs (Figure 3.8D, empty arrowheads), but they deviate at wavelengths below 960 nm with substantial CFP4 FRET donor excitation. In the relevant FRET region between 760 nm and 880 nm where the 2p laser mainly excites the donor fluorophore CFP4 with only minor direct excitation of YPet, normalized aGEPRA G raw FRET values are reduced in the presence of RA (Figure 3.8E and F, compare red and dark blue dashed lines), indicating a reduction in FRET as expected.

# 4. DISCUSSION

## 4.1 Calcineurin Regulates RA-Dependent Homeostatic Synaptic Plasticity

Our data presented in this study show that CaN mediates homeostatic synaptic plasticity by regulating RA synthesis (Figures 3.1 and 3.3). This novel function of CaN seems to be independent of its known role in regulating postsynaptic neurotransmitter receptor trafficking, as the effect was unaltered in phospho-deficient mutants of the GluA1 glutamate receptor subunit (not shown) (Arendt *et al.*, 2015). The results presented in Figure 3.3 also demonstrate that our novel RA reporter system could successfully detect changes in intracellular RA levels with similar sensitivity as our previously used RARE-TK::GFP reporter (*cf.* Figure 3.1). Using either one of two structurally and mechanistically unrelated RA-synthesizing enzyme inhibitors, DEAB or Aldi-6, reporter activity could be reduced to baseline levels, indicating that our reporter is specific for RA and that pharmacological blockade of calcineurin activity increases reporter expression indeed due to cellular RA synthesis.

## 4.2 Transcription-Based Reporter Assays for RA

We developed a novel transcriptional assay for RA based on the transcription-activating function of holo-RARs (Figure 3.2A). Because our previously used RARE-TK::GFP reporter reaches saturating GFP levels shortly after transfection (after 14-15 hours, data not shown), we developed a modified reporter system to eliminate that problem. We reasoned that the natural RARE in our previously used reporter might get occupied by endogenous RARs, thereby potentially causing ligand-independent basal reporter transcription (Nagpal *et al.*, 1993). We therefore fused the DNA-binding domain from the yeast transcription factor Gal4 (Gal4-DBD) to different RAR ligand-binding domains (RARx-LBDs) to yield a chimeric receptor that combines Gal4 DNA-binding specificity with RAR ligand-binding specificity. Together with a firefly luciferase-EGFP fusion reporter gene located downstream of the Gal4-binding "upstream activating sequen-

ce" (UAS), such chimeric Gal4-RAR receptors allowed regulated reporter expression dependent on RA concentration (Figure 3.2). The variants of the chimeric Gal4-RAR receptors we tested showed substantial differences in their responsiveness to RA, consistent with reports describing variable ligand affinities (Repa *et al.*, 1993), transcriptional activities (Nagpal *et al.*, 1992), and transcription cofactor binding (Wei, 2003), between different retinoic acid receptors. Our newly developed reporter system has two major advantages over our previously used RARE-TK::GFP reporter, namely (1) the use of yeast UAS foreign to the mouse genome should alleviate recruitment of endogenous transcription factors, and (2) deletion of the RAR N-terminal and DNA-binding domains from the Gal4 -RAR chimeric receptors eliminates the ligand-independent activating function AF-1, thereby reducing basal activity (Nagpal *et al.*, 1993). The initial chimeric receptor constructs contain a *Herpes simplex* virus VP16 transactivator domain because we designed our reporter following a recently published titratable transgene expression system based on a chimeric transcription factor consisting of the estrogen receptor ligand-binding domain sandwiched between the Gal4 DNA binding domain and a VP16 transactivator domain (Gal4-ER-VP16) (Paulmurugan *et al.*, 2009). Our initial tests revealed noticeable GFP expression already in the absence of RA when VP16-containing receptors were used for reporter activation; hence we chose VP16-lacking receptor chimeras for further testing in neuron cultures because they displayed less baseline activity and therefore higher inducibility in HEK 293T cells. The most responsive receptor was the Gal4-RARαF chimera, mostly because it showed a low baseline activity while being highly inducible by RA, consistent with a report suggesting active repression of RARα-mediated transcription by its specific F-domain in the absence of ligand (Farboud and Privalsky, 2004) (Figure 3.2B and C).

Our new reporter thus exhibits low baseline GFP expression in neurons even several days post-transfection and hence extends the applicability of transcription-based RA detection beyond our previously used RARE-TK::GFP reporter. This novel RA detection assay offers the possibility to temporally uncouple reporter delivery from RA detection to

overcome the tight limitations imposed by quick saturation of the previously used RARE-TK::GFP reporter assay. The new reporter is hence feasible for viral delivery and stable expression in cultured cells, which are prerequisites for reporter use in high-throughput screens to identify further components of the RA-mediated homeostatic synaptic signaling cascade in reporter-expressing neuronal cell cultures. The reporter has been designed to express a fusion protein of firefly luciferase and EGFP (fLuc-EGFP) to facilitate such high-throughput approaches, allowing either the overall population-wide detection of RA by measuring luciferase-activity or the examination of RA production in individual cells by observing cellular EGFP fluorescence. Another attractive option is viral delivery of only the Gal4-RARα chimeric receptor into a universal reporter mouse where either EGFP (Niu *et al.*, 2015) or luciferase are expressed under the control of the yeast "upstream activating sequence" (Pichler *et al.*, 2008), providing means of studying RA production *in vivo* by fluorescence microscopy or by non-invasive luminescence imaging of living subjects.

## 4.3 RA Detection in Living aGEPRA G-Expressing Neurons

Our data presented in Figure 3.6B show that TTX/CNQX-treated aGEPRA G-expressing hippocampal neurons clearly segregate into two subgroups according to their FRET ratio changes induced by synaptic activity blockers followed by subsequent saturating RA application. The first subgroup displays a high response to TTX/CNQX treatment and a very low or no response to the subsequent addition of saturating RA ("responders") while the other group shows low response during the TTX/CNQX treatment and a high RA response at the end ("non-responders"). As shown in Figure 3.6C, we observed a similar response pattern in the DMSO-treated group which even showed a trend towards a stronger average "response" of the aGEPRA signal to the DMSO treatment with less pronounced responses to the final saturating RA addition. The overlay of all individual traces in Figure 3.6D (left panel) clearly shows that most cells from both groups fall into an overlapping region where normalized $CFP_{em}/YFP_{em}$ ratios remain between 1.0 and 1.3

during the drug treatment period. Only three outliers from the DMSO control group rise above a ratio of 1.3, while all cells identified as "non-responders" (dashed lines) exhibit falling ratios dropping to values between 0.75 and 0.95, at the end of the drug treatment. However, the ratios of all cells from the "non-responder" group return to the region between 1.0 and 1.3 where the ratios of almost all cells were recorded after the final, saturating RA treatment. The overlay of the averages of the three identified response groups clearly visualizes how similarly DMSO-treated and TTX/CNQX-treated groups behaved with the exception of the cells from the TTX/CNQX-treated "non-responder" subgroup.

Further analysis of our data confirmed that photobleaching effects could not explain the differences between cells from different groups, because all individual fluorescence channels remained stably within ± 10% around the initially recorded (normalized) intensities (Figure 3.7A-C). The YFP channel where YPet emission is recorded under direct excitation by a 514 nm laser provides the most valuable readout of photobleaching because the signal in this channel is unaffected by FRET. When we plotted the traces obtained in this channel we observed complete overlap of cells from all groups, and the averages between the TTX/CNQX-treated and DMSO-treated groups are virtually identical. To our surprise, we even noticed a trend towards a slight increase of about 10% over the whole imaging sessions (Figure 3.7D).

Possible explanations for our inability to detect increasing RA levels in TTX/CNQX-treated cells include (1) a treatment time too short to allow cellular RA synthesis to occur, (2) the assay sensitivity being too low to detect endogenous RA level changes, or (3) cellular RA synthesis occuring in a more localized and potentially transient fashion at dendrites and synapses, below the spatio-temporal resolution of our imaging protocol.

(1) The time course of RA production during synaptic activity blockade of neuronal networks is unclear, and our 2 hour time course might have been insufficient to observe the onset of cellular RA synthesis. However, RA-mediated homeostatic synaptic plasticity is transcription-independent (Aoto *et al.*, 2008), and synaptic activity blockade stimulates RA synthesis most likely through post-translational modifications of signaling networks.

Enhanced local dendritic translation and insertion of synaptic glutamate receptors can be observed after as little as 1 hour of synaptic activity blockade by TTX/CNQX/APV-treatment (Sutton *et al.*, 2004, Sutton *et al.*, 2006). Because RA production is required for enhanced dendritic glutamate receptor translation and synaptic insertion (Aoto *et al.*, 2008), it needs to occur well within the 2 hour time course of our imaging protocol.

(2) The sensitivity of our assay is dependent on sensor affinity for the RA, FRET ratio changes induced by RA binding, and sensor expression level inside the recorded cells. Sensor affinity and ratio changes have been reported in the original publication where three variants of GEPRA based on RARβ and RARγ were tested (Shimozono *et al.*, 2013). The authors reported that the RARβ-based GEPRA B had a higher affinity but lower FRET change (ΔR/R ~50%) than RARγ-based GEPRA G (ΔR/R ~100%). The reported FRET ratio changes are in good agreement with the changes we observed with our slightly modified variants of the originally published constructs (see Figure 3.5C). However, homeostatic synaptic plasticity is mainly if not exclusively mediated through RARα, and this receptor has a tenfold higher affinity for RA than RARγ upon which aGEPRA G is based (Repa *et al.*, 1993). Homeostatic synaptic plasticity thus possibly functions with RA levels below the sensitivity of the aGEPRA G FRET sensor. This problem is further exacerbated by the remaining toxicity of the aGEPRA probes limiting sensor expression to low levels and potentially increasing background fluorescence noise during the measurements. Even though adding an N-terminal solubility domain to the orginal GEPRA sensors to generate aGEPRAs dramatically reduced cell toxicity, the modified sensors nevertheless caused abnormalities in some transfected neurons (such cells were excluded from analysis).

(3) The third important point of concern is the subcellular localization of cellular RA synthesis which may have obscured possible differences between the treatment groups. For the data presented in Figures 3.6 and 3.7, we chose to plot fluorescence values only from cell somata because somatic fluorescence signals were clearly detectable and remained stable over the entire recording periods. Due to the low sensor expression levels we

could not always visualize fine dendritic branches and only rarely synaptic spines. However, wherever cellular sensor expression levels allowed faithful detection and analysis of dendritic $CFP_{em}/YFP_{em}$ ratios, their time courses always paralleled the ratios we obtained from the somata (data not shown). Moreover, because TTX/CNQX-induced neuronal RA production can be detected in *trans* by HEK 293 cells expressing the RARE-TK::GFP reporter (Aoto *et al.*, 2008), it should also be detectable within the somata of the RA-producing aGEPRA-expressing neurons themselves – again under the assumption of similar or identical sensitivities of both reporter systems.

From these observations we conclude that no biologically relevant differences in cellular RA production are detectable between the TTX/CNQX-treated and DMSO-treated groups under our assay conditions.

## 4.4 Ratiometric FRET Measurements by Two-Photon Microscopy

Our data presented in Figure 3.8 demonstrate that ratiometric FRET measurements are feasible with 2-photon excitation microscopy. Because the Clover and mRuby2 fluorophores are spectrally very well separated, even under 2-photon excitation (Figure 3.8A), we could select excitation wavelengths where either Clover or mRuby2 are selectively excited. This, in combination with the spectra obtained from the isolated fluorophores, allowed us to determine a FRET contribution of approximately 10% to the total emission of a Clover-mRuby2 fusion protein into the mRuby2 channel at wavelengths where only Clover gets directly excited (Figure 3.8C).

We also showed the ratiometric detection of FRET changes induced in aGEPRA G sensor-expressing HEK 293T cells by adding RA. However, the CFP4 and YPet 2-photon excitation spectra show a higher degree of overlap compared to the Clover/mRuby2 FRET pair (compare Figures 3.8D and 3.8A), making absolute quantification impossible without thorough calibration of the method with cells expressing CFP4 and YPet at equimolar concentrations as a FRET-negative bleed-through control. Because aGEPRA G-transfected cells respond reliably and reproducibly to the addition of exogenous RA, they

are nevertheless a useful tool to examine how well the changes in the FRET ratio are detectable under 2-photon excitation. Since donor and acceptor fluorophores are linked in a single polypeptide chain, they are always expressed at an equimolar ratio, justifying the assumption that reporter expression level can be estimated by specific YPet excitation at 1020 nm where no direct CFP4 excitation is detectable (Figure 3.8E, black arrowhead). A region near the YFP excitation peak shows complete overlap of normalized untreated and RA-treated aGEPRA G excitation spectra between 960 nm and 1040 nm, suggesting that this region is devoid of CFP4 excitation and FRET (Figure 3.8E, empty arrowheads). In the spectral region between 760 nm and 880 nm where CFP4 excitation is dominant, we observed a reduction of signal in the yellow fluorescence channel after addition of RA, indicating reduced FRET. The normalized CFP4 emission channel signals, however, show only minor differences between untreated and RA-treated aGEPRA G-expressing cells (Figure 3.8E and F, compare red and dark blue solid lines). We therefore conclude that the reduction in the yellow channel upon RA-stimulation is mostly caused by reduced YPet emission, despite the major bleed-through of CFP4 into the yellow emission channel (approximately 76%) at excitation wavelengths between 760 nm and 880 nm (Figure 3.8E and F, compare solid and dashed cyan lines). The assumption of YPet emission dominating the total signal collected in the yellow emission channel is strongly supported by the fact that YPet emission is much brighter than CFP4 emission in the CFP4/YPet FRET pair under single-photon excitation, even when only CFP4 is directly excited (Nguyen and Daugherty, 2005) (*cf*. Figure 3.5C).

From our measurements of FRET under 2-photon excitation we conclude that detection and quantification should be feasible when the donor and acceptor fluorophores are spectrally well resolved (as is the case for the Clover/mRuby2 FRET pair), and that FRET changes can be detected at least qualitatively with less well-resolved FRET pairs (Fan *et al.*, 1999, Okamoto *et al.*, 2004, Svoboda and Yasuda, 2006) (such as aGEPRA G with the CFP4/YPet FRET pair), even though precise quantification could only be achieved with thorough calibration of the method and subtraction of bleed-through and crosstalk

between channels using FRET positive (tandem fusion of donor and acceptor) and negative controls (molecularly separated donor and acceptor at equimolar concentrations).

## 4.5 Conclusion

We developed a novel transcription-based method that allows faithful detection of RA in reporter-expressing cells after long-term reporter expression. This will make the method useful for viral delivery, allowing its use in high-throughput methods or *in vivo* applications.

Using a non-integrating reporter to detect endogenous RA levels in neurons after synaptic activity blockade yielded uninterpretable results, either because of insufficient sensitivity of the reporter for low RA levels, or because of the volatile nature of RA itself, preventing the activation of a sufficient number of reporter molecules for a duration long enough to permit detection.

We therefore conclude that integrating, transcription-based reporter methods allow for a faithful detection of RA at the expense of subcellular spatial and temporal sensitivity, whereas the non-integrating aGEPRA reporters are an attractive means to indicate sufficiently high levels of RA but fail to detect cellular RA levels produced during the induction of homeostatic synaptic plasticity.

# 5. REFERENCES


1. Aoto, J, CI Nam, MM Poon, P Ting and L Chen (2008). Synaptic signaling by all-trans retinoic acid in homeostatic synaptic plasticity. Neuron 60: 308-320.
2. Arendt, KL, Z Zhang, S Ganesan, M Hintze, MM Shin, Y Tang, A Cho, IA Graef and L Chen (2015). Calcineurin mediates homeostatic synaptic plasticity by regulating retinoic acid synthesis. Proc Natl Acad Sci U S A 112: E5744-5752.
3. Awais, M, M Sato, K Sasaki and Y Umezawa (2004). A genetically encoded fluorescent indicator capable of discriminating estrogen agonists from antagonists in living cells. Anal Chem 76: 2181-2186.
4. Baumgartel, K and IM Mansuy (2012). Neural functions of calcineurin in synaptic plasticity and memory. Learn Mem 19: 375-384.
5. Beattie, EC, RC Carroll, X Yu, W Morishita, H Yasuda, M von Zastrow and RC Malenka (2000). Regulation of AMPA receptor endocytosis by a signaling mechanism shared with LTD. Nat Neurosci 3: 1291-1300.
6. Bienenstock, EL, LN Cooper and PW Munro (1982). Theory for the development of neuron selectivity: orientation specificity and binocular interaction in visual cortex. J Neurosci 2: 32-48.
7. Bliss, TV and T Lomo (1973). Long-lasting potentiation of synaptic transmission in the dentate area of the anaesthetized rabbit following stimulation of the perforant path. J Physiol 232: 331-356.
8. Bourguet, W, P Germain and H Gronemeyer (2000a). Nuclear receptor ligand-binding domains: three-dimensional structures, molecular interactions and pharmacological implications. Trends Pharmacol Sci 21: 381-388.
9. Bourguet, W, M Ruff, P Chambon, H Gronemeyer and D Moras (1995). Crystal structure of the ligand-binding domain of the human nuclear receptor RXR-alpha. Nature 375: 377-382.
10. Bourguet, W, V Vivat, JM Wurtz, P Chambon, H Gronemeyer and D Moras (2000b). Crystal structure of a heterodimeric complex of RAR and RXR ligand-binding domains. Mol Cell 5: 289-298.
11. Brelivet, Y, N Rochel and D Moras (2012). Structural analysis of nuclear receptors: from isolated domains to integral proteins. Mol Cell Endocrinol 348: 466-473.
12. Budde, T, S Meuth and HC Pape (2002). Calcium-dependent inactivation of neuronal calcium channels. Nat Rev Neurosci 3: 873-883.
13. Burley, JR and TS Sihra (2000). A modulatory role for protein phosphatase 2B (calcineurin) in the regulation of Ca2+ entry. Eur J Neurosci 12: 2881-2891.
14. Cahalan, MD, I Parker, SH Wei and MJ Miller (2002). Two-photon tissue imaging: seeing the immune system in a fresh light. Nat Rev Immunol 2: 872-880.
15. Campbell, RE (2009). Fluorescent-protein-based biosensors: modulation of energy transfer as a design principle. Anal Chem 81: 5972-5979.
16. Chang, C, JD Norris, H Gron, LA Paige, PT Hamilton, DJ Kenan, D Fowlkes and DP McDonnell (1999). Dissection of the LXXLL nuclear receptor-coactivator interaction motif using combinatorial peptide libraries: discovery of peptide antagonists of estrogen receptors alpha and beta. Mol Cell Biol 19: 8226-8239.
17. Chater, TE and Y Goda (2014). The role of AMPA receptors in postsynaptic mechanisms of synaptic plasticity. Front Cell Neurosci 8: 401.

18. Chen, L, AG Lau and F Sarti (2014). Synaptic retinoic acid signaling and homeostatic synaptic plasticity. Neuropharmacology 78: 3-12.

19. Chen, W, JJ Zhang, GY Hu and CP Wu (1995). GABAA receptor-mediated feedback inhibition in pyramidal neurons of cat motor cortex. Neurosci Lett 198: 123-126.

20. Coghlan, VM, BA Perrino, M Howard, LK Langeberg, JB Hicks, WM Gallatin and JD Scott (1995). Association of protein kinase A and protein phosphatase 2B with a common anchoring protein. Science 267: 108-111.

21. Colledge, M, RA Dean, GK Scott, LK Langeberg, RL Huganir and JD Scott (2000). Targeting of PKA to glutamate receptors through a MAGUK-AKAP complex. Neuron 27: 107-119.

22. Darimont, BD, RL Wagner, JW Apriletti, MR Stallcup, PJ Kushner, JD Baxter, RJ Fletterick and KR Yamamoto (1998). Structure and specificity of nuclear receptor-coactivator interactions. Genes Dev 12: 3343-3356.

23. Dell'Acqua, ML, KL Dodge, SJ Tavalin and JD Scott (2002). Mapping the protein phosphatase-2B anchoring site on AKAP79. Binding and inhibition of phosphatase activity are mediated by residues 315-360. J Biol Chem 277: 48796-48802.

24. Denk, W, JH Strickler and WW Webb (1990). Two-photon laser scanning fluorescence microscopy. Science 248: 73-76.

25. Di Filippo, M, B Picconi, M Tantucci, V Ghiglieri, V Bagetta, C Sgobio, A Tozzi, L Parnetti and P Calabresi (2009). Short-term and long-term plasticity at corticostriatal synapses: implications for learning and memory. Behav Brain Res 199: 108-118.

26. Dittmer, PJ, ML Dell'Acqua and WA Sather (2014). Ca2+/calcineurin-dependent inactivation of neuronal L-type Ca2+ channels requires priming by AKAP-anchored protein kinase A. Cell Rep 7: 1410-1416.

27. Dudek, SM and MF Bear (1992). Homosynaptic long-term depression in area CA1 of hippocampus and effects of N-methyl-D-aspartate receptor blockade. Proc Natl Acad Sci U S A 89: 4363-4367.

28. Fan, GY, H Fujisaki, A Miyawaki, RK Tsay, RY Tsien and MH Ellisman (1999). Video-rate scanning two-photon excitation fluorescence microscopy and ratio imaging with cameleons. Biophys J 76: 2412-2420.

29. Farboud, B and ML Privalsky (2004). Retinoic acid receptor-alpha is stabilized in a repressive state by its C-terminal, isotype-specific F domain. Mol Endocrinol 18: 2839-2853.

30. Feldman, DE (2009). Synaptic mechanisms for plasticity in neocortex. Annu Rev Neurosci 32: 33-55.

31. Förster, T (1948). Zwischenmolekulare Energiewanderung und Fluoreszenz. Annalen der Physik 437: 55-75.

32. Goldberg, J, K Holthoff and R Yuste (2002). A problem with Hebb and local spikes. Trends Neurosci 25: 433-435.

33. Gomez, LL, S Alam, KE Smith, E Horne and ML Dell'Acqua (2002). Regulation of A-kinase anchoring protein 79/150-cAMP-dependent protein kinase postsynaptic targeting by NMDA receptor activation of calcineurin and remodeling of dendritic actin. J Neurosci 22: 7027-7044.

34. Göppert-Mayer, M (1931). Über Elementarakte mit zwei Quantensprüngen. Annalen der Physik 401: 273-294.

35. Groth, RD, RL Dunbar and PG Mermelstein (2003). Calcineurin regulation of neuronal plasticity. Biochem Biophys Res Commun 311: 1159-1171.

36. Groth, RD and RW Tsien (2008). A role for retinoic acid in homeostatic plasticity. Neuron 60: 192-194.

37. Heery, DM, E Kalkhoven, S Hoare and MG Parker (1997). A signature motif in transcriptional co-activators mediates binding to nuclear receptors. Nature 387: 733-736.

38. Huang, P, V Chandra and F Rastinejad (2014). Retinoic acid actions through mammalian nuclear receptors. Chem Rev 114: 233-254.

39. Husi, H, MA Ward, JS Choudhary, WP Blackstock and SG Grant (2000). Proteomic analysis of NMDA receptor-adhesion protein signaling complexes. Nat Neurosci 3: 661-669.

40. Ikegami, S and K Inokuchi (2000). Antisense DNA against calcineurin facilitates memory in contextual fear conditioning by lowering the threshold for hippocampal long-term potentiation induction. Neuroscience 98: 637-646.

41. Jablonski, A (1933). Efficiency of Anti-Stokes Fluorescence in Dyes. Nature 131: 839-840.

42. Jones, MV and GL Westbrook (1997). Shaping of IPSCs by endogenous calcineurin activity. J Neurosci 17: 7626-7633.

43. Ju, W, W Morishita, J Tsui, G Gaietta, TJ Deerinck, SR Adams, CC Garner, RY Tsien, MH Ellisman and RC Malenka (2004). Activity-dependent regulation of dendritic synthesis and trafficking of AMPA receptors. Nat Neurosci 7: 244-253.

44. Kessels, HW and R Malinow (2009). Synaptic AMPA receptor plasticity and behavior. Neuron 61: 340-350.

45. Klauck, TM, MC Faux, K Labudda, LK Langeberg, S Jaken and JD Scott (1996). Coordination of three signaling enzymes by AKAP79, a mammalian scaffold protein. Science 271: 1589-1592.

46. Klee, CB, TH Crouch and MH Krinks (1979). Calcineurin: a calcium- and calmodulin-binding protein of the nervous system. Proc Natl Acad Sci U S A 76: 6270-6273.

47. Klee, CB and MH Krinks (1978). Purification of cyclic 3',5'-nucleotide phosphodiesterase inhibitory protein by affinity chromatography on activator protein coupled to Sepharose. Biochemistry 17: 120-126.

48. Kotaleski, JH and KT Blackwell (2010). Modelling the molecular mechanisms of synaptic plasticity using systems biology approaches. Nat Rev Neurosci 11: 239-251.

49. Krupp, JJ, B Vissel, CG Thomas, SF Heinemann and GL Westbrook (2002). Calcineurin acts via the C-terminus of NR2A to modulate desensitization of NMDA receptors. Neuropharmacology 42: 593-602.

50. Lam, AJ, F St-Pierre, Y Gong, JD Marshall, PJ Cranfill, MA Baird, MR McKeown, J Wiedenmann, MW Davidson, MJ Schnitzer, RY Tsien and MZ Lin (2012). Improving FRET dynamic range with bright green and red fluorescent proteins. Nat Methods 9: 1005-1012.

51. Lane, MA and SJ Bailey (2005). Role of retinoid signalling in the adult brain. Prog Neurobiol 75: 275-293.

52. le Maire, A, C Teyssier, C Erb, M Grimaldi, S Alvarez, AR de Lera, P Balaguer, H Gronemeyer, CA Royer, P Germain and W Bourguet (2010). A unique secondary-structure switch controls constitutive gene repression by retinoic acid receptor. Nat Struct Mol Biol 17: 801-807.

53. Lee, HK and A Kirkwood (2011). AMPA receptor regulation during synaptic plasticity in hippocampus and neocortex. Semin Cell Dev Biol 22: 514-520.

54. Lieberman, DN and I Mody (1994). Regulation of NMDA channel function by endogenous Ca(2+)-dependent phosphatase. Nature 369: 235-239.

55. Lopez-Munoz, F, J Boya and C Alamo (2006). Neuron theory, the cornerstone of neuroscience, on the centenary of the Nobel Prize award to Santiago Ramon y Cajal. Brain Res Bull 70: 391-405.

56. Lukyanetz, EA, TP Piper and TS Sihra (1998). Calcineurin involvement in the regulation of high-threshold Ca2+ channels in NG108-15 (rodent neuroblastoma x glioma hybrid) cells. J Physiol 510 ( Pt 2): 371-385.

57. Luscher, B, T Fuchs and CL Kilpatrick (2011). GABAA receptor trafficking-mediated plasticity of inhibitory synapses. Neuron 70: 385-409.

58. Maden, M (2007). Retinoic acid in the development, regeneration and maintenance of the nervous system. Nat Rev Neurosci 8: 755-765.

59. Malleret, G, U Haditsch, D Genoux, MW Jones, TV Bliss, AM Vanhoose, C Weitlauf, ER Kandel, DG Winder and IM Mansuy (2001). Inducible and reversible enhancement of learning, memory, and long-term potentiation by genetic inhibition of calcineurin. Cell 104: 675-686.

60. Man, HY, Y Sekine-Aizawa and RL Huganir (2007). Regulation of {alpha}-amino-3-hydroxy-5-methyl-4-isoxazolepropionic acid receptor trafficking through PKA phosphorylation of the Glu receptor 1 subunit. Proc Natl Acad Sci U S A 104: 3579-3584.

61. Mansuy, IM, M Mayford, B Jacob, ER Kandel and ME Bach (1998a). Restricted and regulated overexpression reveals calcineurin as a key component in the transition from short-term to long-term memory. Cell 92: 39-49.

62. Mansuy, IM, DG Winder, TM Moallem, M Osman, M Mayford, RD Hawkins and ER Kandel (1998b). Inducible and reversible gene expression with the rtTA system for the study of memory. Neuron 21: 257-265.

63. Martin, SJ, PD Grimwood and RG Morris (2000). Synaptic plasticity and memory: an evaluation of the hypothesis. Annu Rev Neurosci 23: 649-711.

64. Michelini, E, L Cevenini, L Mezzanotte, A Coppa and A Roda (2010). Cell-based assays: fuelling drug discovery. Anal Bioanal Chem 398: 227-238.

65. Miller, KD and DJC MacKay (1994). The role of constraints in Hebbian learning. Neural Comp 6: 100-126.

66. Miller, SG and MB Kennedy (1986). Regulation of brain type II Ca2+/calmodulin-dependent protein kinase by autophosphorylation: a Ca2+-triggered molecular switch. Cell 44: 861-870.

67. Moras, D and H Gronemeyer (1998). The nuclear receptor ligand-binding domain: structure and function. Curr Opin Cell Biol 10: 384-391.

68. Morishita, W, H Marie and RC Malenka (2005). Distinct triggering and expression mechanisms underlie LTD of AMPA and NMDA synaptic responses. Nat Neurosci 8: 1043-1050.

69. Moutier, E, T Ye, MA Choukrallah, S Urban, J Osz, A Chatagnon, L Delacroix, D Langer, N Rochel, D Moras, G Benoit and I Davidson (2012). Retinoic acid receptors recognize the mouse genome through binding elements with diverse spacing and topology. J Biol Chem 287: 26328-26341.

70. Mulkey, RM, S Endo, S Shenolikar and RC Malenka (1994). Involvement of a calcineurin/inhibitor-1 phosphatase cascade in hippocampal long-term depression. Nature 369: 486-488.

71. Mulkey, RM, CE Herron and RC Malenka (1993). An essential role for protein phosphatases in hippocampal long-term depression. Science 261: 1051-1055.

72. Mulkey, RM and RC Malenka (1992). Mechanisms underlying induction of homosynaptic long-term depression in area CA1 of the hippocampus. Neuron 9: 967-975.

73. Nagpal, S, S Friant, H Nakshatri and P Chambon (1993). RARs and RXRs: evidence for two autonomous transactivation functions (AF-1 and AF-2) and heterodimerization in vivo. EMBO J 12: 2349-2360.

74. Nagpal, S, M Saunders, P Kastner, B Durand, H Nakshatri and P Chambon (1992). Promoter context- and response element-dependent specificity of the transcriptional activation and modulating functions of retinoic acid receptors. Cell 70: 1007-1019.

75. Napoli, JL (1996). Retinoic acid biosynthesis and metabolism. FASEB J 10: 993-1001.

76. Nguyen, AW and PS Daugherty (2005). Evolutionary optimization of fluorescent proteins for intracellular FRET. Nat Biotechnol 23: 355-360.

77. Niu, H, J Chacko, G Hadwiger and JS Welch (2015). Absence of natural intracellular retinoids in mouse bone marrow cells and implications for PML-RARA transformation. Blood Cancer J 5: e284.

78. Oja, E (1982). A simplified neuron model as a principal component analyzer. J Math Biol 15: 267-273.

79. Okamoto, K, T Nagai, A Miyawaki and Y Hayashi (2004). Rapid and persistent modulation of actin dynamics regulates postsynaptic reorganization underlying bidirectional plasticity. Nat Neurosci 7: 1104-1112.

80. Oliveria, SF, LL Gomez and ML Dell'Acqua (2003). Imaging kinase--AKAP79--phosphatase scaffold complexes at the plasma membrane in living cells using FRET microscopy. J Cell Biol 160: 101-112.

81. Paulmurugan, R, P Padmanabhan, BC Ahn, S Ray, JK Willmann, TF Massoud, S Biswal and SS Gambhir (2009). A novel estrogen receptor intramolecular folding-based titratable transgene expression system. Mol Ther 17: 1703-1711.

82. Perissi, V and MG Rosenfeld (2005). Controlling nuclear receptors: the circular logic of cofactor cycles. Nat Rev Mol Cell Biol 6: 542-554.

83. Pichler, A, JL Prior, GD Luker and D Piwnica-Worms (2008). Generation of a highly inducible Gal4-->Fluc universal reporter mouse for in vivo bioluminescence imaging. Proc Natl Acad Sci U S A 105: 15932-15937.

84. Pogenberg, V, JF Guichou, V Vivat-Hannah, S Kammerer, E Perez, P Germain, AR de Lera, H Gronemeyer, CA Royer and W Bourguet (2005). Characterization of the interaction between retinoic acid receptor/retinoid X receptor (RAR/RXR) heterodimers and transcriptional coactivators through structural and fluorescence anisotropy studies. J Biol Chem 280: 1625-1633.

85. Poon, MM and L Chen (2008). Retinoic acid-gated sequence-specific translational control by RARalpha. Proc Natl Acad Sci U S A 105: 20303-20308.

86. Pugh, JR and IM Raman (2009). Nothing can be coincidence: synaptic inhibition and plasticity in the cerebellar nuclei. Trends Neurosci 32: 170-177.

87. Rabinowitch, I and I Segev (2006). The endurance and selectivity of spatial patterns of long-term potentiation/depression in dendrites under homeostatic synaptic plasticity. J Neurosci 26: 13474-13484.

88. Rabinowitch, I and I Segev (2006). The interplay between homeostatic synaptic plasticity and functional dendritic compartments. J Neurophysiol 96: 276-283.

89. Renaud, JP, N Rochel, M Ruff, V Vivat, P Chambon, H Gronemeyer and D Moras (1995). Crystal structure of the RAR-gamma ligand-binding domain bound to all-trans retinoic acid. Nature 378: 681-689.

90. Repa, JJ, KK Hanson and M Clagett-Dame (1993). All-trans-retinol is a ligand for the retinoic acid receptors. Proc Natl Acad Sci U S A 90: 7293-7297.

91. Robello, M, C Amico and A Cupello (1997). A dual mechanism for impairment of GABAA receptor activity by NMDA receptor activation in rat cerebellum granule cells. Eur Biophys J 25: 181-187.

92. Sadowski, I, J Ma, S Triezenberg and M Ptashne (1988). GAL4-VP16 is an unusually potent transcriptional activator. Nature 335: 563-564.

93. Santos, SD, AL Carvalho, MV Caldeira and CB Duarte (2009). Regulation of AMPA receptors and synaptic plasticity. Neuroscience 158: 105-125.

94. Sarti, F, Z Zhang, J Schroeder and L Chen (2013). Rapid suppression of inhibitory synaptic transmission by retinoic acid. J Neurosci 33: 11440-11450.

95. Seung, HS (2000). Half a century of Hebb. Nat Neurosci 3 Suppl: 1166.

96. Sever, R and CK Glass (2013). Signaling by nuclear receptors. Cold Spring Harb Perspect Biol 5: a016709.

97. Shimozono, S, T Iimura, T Kitaguchi, S Higashijima and A Miyawaki (2013). Visualization of an endogenous retinoic acid gradient across embryonic development. Nature 496: 363-366.

98. Singer, JH, E Glowatzki, T Moser, BW Strowbridge, V Bhandawat and AP Sampath (2009). Functional properties of synaptic transmission in primary sense organs. J Neurosci 29: 12802 -12806.

99. So, PTC (2001). Two-photon Fluorescence Light Microscopy. eLS, John Wiley & Sons, Ltd.

100. Strack, S, MA Barban, BE Wadzinski and RJ Colbran (1997). Differential inactivation of postsynaptic density-associated and soluble Ca2+/calmodulin-dependent protein kinase II by protein phosphatases 1 and 2A. J Neurochem 68: 2119-2128.

101. Sutton, MA, HT Ito, P Cressy, C Kempf, JC Woo and EM Schuman (2006). Miniature neurotransmission stabilizes synaptic function via tonic suppression of local dendritic protein synthesis. Cell 125: 785-799.

102. Sutton, MA, NR Wall, GN Aakalu and EM Schuman (2004). Regulation of dendritic protein synthesis by miniature synaptic events. Science 304: 1979-1983.

103. Svoboda, K and R Yasuda (2006). Principles of two-photon excitation microscopy and its applications to neuroscience. Neuron 50: 823-839.

104. Sweatt, JD (2016). Neural plasticity and behavior - sixty years of conceptual advances. J Neurochem 139 Suppl 2: 179-199.

105. Takeuchi, T, AJ Duszkiewicz and RG Morris (2014). The synaptic plasticity and memory hypothesis: encoding, storage and persistence. Philos Trans R Soc Lond B Biol Sci 369: 20130288.

106. Tavalin, SJ, M Colledge, JW Hell, LK Langeberg, RL Huganir and JD Scott (2002). Regulation of GluR1 by the A-kinase anchoring protein 79 (AKAP79) signaling complex shares properties with long-term depression. J Neurosci 22: 3044-3051.

107. Thiagarajan, TC, M Lindskog and RW Tsien (2005). Adaptation to synaptic inactivity in hippocampal neurons. Neuron 47: 725-737.

108. Tong, G, D Shepherd and CE Jahr (1995). Synaptic desensitization of NMDA receptors by calcineurin. Science 267: 1510-1512.

109. Turrigiano, G (2012). Homeostatic synaptic plasticity: local and global mechanisms for stabilizing neuronal function. Cold Spring Harb Perspect Biol 4: a005736.

110. Turrigiano, GG, KR Leslie, NS Desai, LC Rutherford and SB Nelson (1998). Activity-dependent scaling of quantal amplitude in neocortical neurons. Nature 391: 892-896.

111. Turrigiano, GG and SB Nelson (2004). Homeostatic plasticity in the developing nervous system. Nat Rev Neurosci 5: 97-107.

112. Umezawa, Y (2005). Genetically encoded optical probes for imaging cellular signaling pathways. Biosens Bioelectron 20: 2504-2511.

113. Wang, H, E Nakata and I Hamachi (2009). Recent progress in strategies for the creation of protein-based fluorescent biosensors. Chembiochem 10: 2560-2577.

114. Wang, HL, Z Zhang, M Hintze and L Chen (2011). Decrease in calcium concentration triggers neuronal retinoic acid synthesis during homeostatic synaptic plasticity. J Neurosci 31: 17764-17771.

115. Wang, J, S Liu, U Haditsch, W Tu, K Cochrane, G Ahmadian, L Tran, J Paw, Y Wang, I Mansuy, MM Salter and YM Lu (2003). Interaction of calcineurin and type-A GABA receptor gamma 2 subunits produces long-term depression at CA1 inhibitory synapses. J Neurosci 23: 826-836.

116. Wei, LN (2003). Retinoid receptors and their coregulators. Annu Rev Pharmacol Toxicol 43: 47-72.

117. Winder, DG, IM Mansuy, M Osman, TM Moallem and ER Kandel (1998). Genetic and pharmacological evidence for a novel, intermediate phase of long-term potentiation suppressed by calcineurin. Cell 92: 25-37.

118. Woolfrey, KM and ML Dell'Acqua (2015). Coordination of Protein Phosphorylation and Dephosphorylation in Synaptic Plasticity. J Biol Chem 290: 28604-28612.

119. Wu, ZZ, SR Chen and HL Pan (2005). Transient receptor potential vanilloid type 1 activation down-regulates voltage-gated calcium channels through calcium-dependent calcineurin in sensory neurons. J Biol Chem 280: 18142-18151.

120. Wurtz, JM, W Bourguet, JP Renaud, V Vivat, P Chambon, D Moras and H Gronemeyer (1996). A canonical structure for the ligand-binding domain of nuclear receptors. Nat Struct Biol 3: 206.

121. Yu, LM and Y Goda (2009). Dendritic signalling and homeostatic adaptation. Curr Opin Neurobiol 19: 327-335.

122. Zeng, H, S Chattarji, M Barbarosie, L Rondi-Reig, BD Philpot, T Miyakawa, MF Bear and S Tonegawa (2001). Forebrain-specific calcineurin knockout selectively impairs bidirectional synaptic plasticity and working/episodic-like memory. Cell 107: 617-629.

123. Zipfel, WR, RM Williams and WW Webb (2003). Nonlinear magic: multiphoton microscopy in the biosciences. Nat Biotechnol 21: 1369-1377.

# Appendix 1: List of Figures

# Appendix 2: List of Tables

# Appendix 3: List of Abbreviations

| | |
|---|---|
| % | per cent |
| > | larger |
| °C | degrees Celsius |
| µg | microgram |
| µL | microliter |
| µm | micrometer |
| 2p | two-photon |
| ACT | acceptor cross talk |
| AF | activating function |
| AID | autoinhibitory domain |
| AIP | autoinhibitory peptide |
| AKAP | A-kinase anchoring protein |
| AMPA | α-amino-3-hydroxy-5-methyl-4-isoxazole proprionate |
| AMPAR | AMPA-type glutamate receptor |
| APV | 2-amino-5-phosphonovaleric acid |
| Ara-C | cytosine β-D-arabinofuranoside |
| avg | average |
| BBH | calcineurin B binding helix |
| CaM | calmodulin |
| CaMB | calmodulin-binding |
| CaMKII | calmodulin-dependent protein kinase II |
| CaN | calcineurin |
| *cf.* | confer |
| CnA | calcineurin, A subunit |
| CnB | calcineurin, B subunit |
| CNQX | 6-cyano-7-nitroquinoxaline-2,3-dione |
| $CO_2$ | carbon dioxide |
| cpYPet | circularly permuted yellow fluorescent protein for energy transfer |
| CS | cover glass |
| CsA | cyclosporin A |
| C-terminal | carboxy-terminal |
| ctrl. | control |
| Δ | difference |
| DBD | DNA-binding domain |
| DBT | donor bleed-through |
| DEAB | 4-diethylaminobenzaldehyde |
| DIC | differential interference contrast |
| DIV | day *in vitro* |
| DMEM | DUBECCO's modified essential medium |
| DMSO | dimethyl sulfoxide |
| DNA | deoxyribonucleic acid |
| dNTP | deoxyribonucleotide trisphosphate |
| ΔR/R | normalized ratio change |

| | |
|---|---|
| e.g. | for example |
| ECFP | enhanced cyan fluorescent protein |
| EGFP | enhanced green fluorescent protein |
| em | emission |
| ER | estrogen receptor |
| *et al.* | and others |
| ex | excitation |
| EYFP | enhanced yellow fluorescent protein |
| F-actin | filamentous (polymeric) actin |
| FCS | fetal bovine serum (fetal calf serum) |
| $\Phi_D$ | donor quantum yield |
| fLuc | firefly luciferase |
| FRET | FÖRSTER resonance energy transfer |
| G | conductance |
| g | gram |
| GABA | γ-amino-butyric acid |
| $GABA_AR$ | A-type GABA receptor |
| G-actin | globular (monomeric) actin |
| Gal4 | regulatory yeast protein GAL4 |
| GEPRA | genetically engineered probe for RA |
| GFP | green fluorescent protein |
| GluA1 | AMPA-type glutamate receptor subunit 1 |
| GluN2A | NMDA-type glutamate receptor subunit 2A |
| H | helix |
| HBSS | HANK's balanced salt solution |
| HEK cells | human embryonic kidney cell line |
| HEPES | 4-(2-hydroxyethyl)-1-piperazineethanesulfonic acid |
| HSP | homeostatic synaptic plasticity |
| i.e. | that is |
| I-1 | protein phosphatase inhibitor 1 |
| $\mathcal{J}(\lambda)$ | spectral overlap integral between fluorophores |
| $\kappa^2$ | orientation factor between fluorophores |
| kbp | kilo basepairs |
| $k_T$ | energy transfer rate |
| L | liter |
| $\lambda$ | wavelength |
| LBD | ligand-binding domain |
| LSM | laser-scanning microscope |
| LTD | (synaptic) long-term depression |
| LTP | (synaptic) long-term potentiation |
| M | molar |
| MAGUK | membrane-associated guanylate kinase |
| mCFP | monomeric cyan fluorescent protein |
| MCS | multiple cloning site |
| MEM | minimum essential medium |

| | |
|---|---|
| mEPSC | miniature excitatory postsynaptic current |
| mg | milligram |
| MHz | mega Hertz |
| min. | minute |
| mL | milliliter |
| mm | millimeter |
| mRNA | messenger ribonucleic acid |
| mYFP | monomeric yellow fluorescent protein |
| N | number of independent experiments |
| n | number of events observed |
| *n* | refractive index |
| $NAD^+$ | nicotinamide adenine dinucleotide (oxidized form) |
| NADH | nicotinamide adenine dinucleotide (reduced form) |
| NaN | not a number |
| NB | neurobasal medium |
| ng | nanogram |
| NGM | neurobasal growth media |
| nm | nanometer |
| nM | nanomolar |
| NMDA | N-methyl-D-aspartate |
| NMDAR | NMDA-type glutamate receptor |
| non-resp. | non-responder |
| norm. | normalized |
| NR | nuclear receptor |
| N-terminal | amino-terminal |
| p | plasmid |
| P | p value |
| PBS | phosphate-buffered saline |
| PCR | polymerase chain reaction |
| PFA | paraformaldehyde |
| PKA | protein kinase A |
| PKC | protein kinase C |
| PLL | poly-L lysine |
| PP1 | protein phosphatase 1 |
| PP2B | protein phosphatase 2B (calcineurin) |
| PSD | post-synaptic density |
| *r* | distance between fluorophores |
| $R_0$ | FÖRSTER radius |
| RA | all-*trans* retinoic acid |
| RALDH | retinaldehyde dehydrogenase |
| RAR | retinoic acid receptor |
| RARE | retinoic acid response element |
| resp. | responder |
| RNA | ribonucleic acid |
| ROLDH | retinol dehydrogenase |

| | |
|---|---|
| RXR | retinoid X receptor |
| s | second |
| $S_0$ | electronic ground state |
| $S_1$ | first electronic excited state |
| SEM | standard error of the mean |
| SNM | serum neuron media |
| syn | synaptic |
| t | time |
| TA | transactivator |
| $\tau_D$ | donor fluorescence lifetime |
| TK | thymidine kinase |
| Tm | primer annealing temperature |
| TTX | tetrodotoxin |
| UAS | upstream activating sequence |
| V | voltage |
| VP16 | *Herpes simplex* viral protein 16 |
| *vs*. | versus |
| x | fold |
| XFP | fluorescent protein of any color |
| YPet | yellow fluorescent protein for energy transfer |

# Appendix 4: Sequences of DNA Constructs Used in This Study

## 1. Gal4-RAR-VP16 chimeric receptor constructs

Gal4-MCS-VP16 cloning vector sequence

```
TCC GCT AGC GAC AAG CTT ATG AAG CTA CTG TCT TCT ATC GAA CAA GCA TGC GAT ATT TGC
                        Met Lys Leu Leu Ser Ser Ile Glu Gln Ala Cys Asp Ile Cys
    NheI        HindIII

CGA CTT AAA AAG CTC AAG TGC TCC AAA GAA AAA CCG AAG TGC GCC AAG TGT CTG AAG AAC
Arg Leu Lys Lys Leu Lys Cys Ser Lys Glu Lys Pro Lys Cys Ala Lys Cys Leu Lys Asn

AAC TGG GAG TGT CGC TAC TCT CCC AGA ACC AAA AGG TCT CCG CTG ACT AGG GCA CAT CTG
Asn Trp Glu Cys Arg Tyr Ser Pro Arg Thr Lys Arg Ser Pro Leu Thr Arg Ala His Leu

ACA GAA GTG GAA TCA AGG CTA GAA AGA CTG GAA CAG CTA TTT CTA CTG ATT TTT CCT CGT
Thr Glu Val Glu Ser Arg Leu Glu Arg Leu Glu Gln Leu Phe Leu Leu Ile Phe Pro Arg

GAA GAC CTT GAC ATG ATT TTG AAA ATG GAT TCT TTA CAG GAT ATA AAA GCA TTG TTG ACA
Glu Asp Leu Asp Met Ile Leu Lys Met Asp Ser Leu Gln Asp Ile Lys Ala Leu Leu Thr

GGA TTA TTT GTT CAA GAT AAT GTG AAT AAA GAT GCC GTC ACA GAT AGA TTG GCT TCA GTG
Gly Leu Phe Val Gln Asp Asn Val Asn Lys Asp Ala Val Thr Asp Arg Leu Ala Ser Val

GAG ACT GAT ATG CCT CTA ACA TTG AGA CAG CAT AGA ATA AGT GCG ACA TCA TCA TCG GAA
Glu Thr Asp Met Pro Leu Thr Leu Arg Gln His Arg Ile Ser Ala Thr Ser Ser Ser Glu

GAG AGT AGT AAC AAA GGT CAA AGA CAG TTG ACT GTA TCG CCG GAA TTC CTG CAG CCC GGG
Glu Ser Ser Asn Lys Gly Gln Arg Gln Leu Thr Val Ser Pro Glu Phe Leu Gln Pro Gly
                                                    EcoRI   PstI    XmaI
                                                                    SmaI

GGT ACC GGT AGC GGA TCC GCC CCA CCG ACC GAT GTC TCA CTG GGA GAC GAG CTC CAT TTA
Gly Thr Gly Ser Gly Ser Ala Pro Pro Thr Asp Val Ser Leu Gly Asp Glu Leu His Leu
Acc65I          BamHI
KpnI  AgeI

GAC GGT GAG GAC GTG GCT ATG GCA CAT GCC GAC GCA CTA GAC GAT TTC GAT CTA GAC ATG
Asp Gly Glu Asp Val Ala Met Ala His Ala Asp Ala Leu Asp Asp Phe Asp Leu Asp Met

TTG GGA GAC GGT GAT TCC CCA GGT CCT aga tcc GCA CCT CCG ACC GAT GTC AGC CTG GGT
Leu Gly Asp Gly Asp Ser Pro Gly Pro Arg Ser Ala Pro Pro Thr Asp Val Ser Leu Gly

GAC GAG CTC CAC TTG GAC GGT GAG GAC GTG GCG ATG GCT CAT GCC GAC GCG CTA GAC GAC
Asp Glu Leu His Leu Asp Gly Glu Asp Val Ala Met Ala His Ala Asp Ala Leu Asp Asp

TTC GAT CTA GAC ATG TTG GGT GAC GGA GAT TCA CCA GGT CCG aga tcc tct aga tct aga
Phe Asp Leu Asp Met Leu Gly Asp Gly Asp Ser Pro Gly Pro Arg Ser Ser Arg Ser Arg
                                                            BglII

ggg ccc gtt taa GCG GCC GCG ACT
Gly Pro Val END
ApaI            NotI
```

The construct was synthesized as two separate gBlock fragments (Integrated DNA Technologies, Inc.) and was cloned into the pEGFP-N1 plasmid backbone using the *Nhe*I and *Not*I restriction enzyme sites. Amino acid sequences of **Gal4-DBD** and the 2x **VP16** tandem repeats are color indicated in **bold** print. The Gal4 **K43R** mutation is highlighted in **red**. All restriction enzyme sites indicated are unique.

RAR insert sequences

Sequence stretches [ … ] between indicated insertion sites correspond to GenBank entries XM_017597011.1 (rat RARα), NM_001289762.1 (mouse RARβ), NM_001135250.1 (rat RARγ).

RARα$_{182-416}$ (LBD)

```
CCG GAA TTC GGG GAA CTC [ ... ] TCT GAG GGC GGA TCC GCC
Pro Glu Phe Gly Glu Leu [ ... ] Ser Glu Gly Gly Ser Ala
    EcoRI                                   BamHI
```

RARα$_{182-459}$ (LBD + F domain)

```
CCG GAA TTC GGG GAA CTC [ ... ] CAA TCC CCA GGA TCC GCC
Pro Glu Phe Gly Glu Leu [ ... ] Gln Ser Pro Gly Ser Ala
    EcoRI                                   BamHI
```

RARβ$_{178-412}$ (LBD)

```
GGT ACC GGT GAC GAC CTC [ ... ] TCT GAA GGA GGA TCC GCC
Gly Thr Gly Asp Asp Leu [ ... ] Ser Glu Gly Gly Ser Ala
    AgeI                                    BamHI
```

RARβ$_{182-448}$ (LBD + F domain)

```
GGT ACC GGT GAC GAC CTC [ ... ] CTG CTG CAG GGA TCC GCC
Gly Thr Gly Asp Asp Leu [ ... ] Leu Leu Gln Gly Ser Ala
    AgeI                                    BamHI
```

RARγ$_{214-448}$ (LBD)

```
CCG GAA TTC GAG GAG CTC [ ... ] CCT GAG ATG GGA TCC GCC
Pro Glu Phe Glu Glu Leu [ ... ] Pro Glu Met Gly Ser Ala
    EcoRI                                   BamHI
```

RARγ$_{214-485}$ (LBD + F domain)

```
CCG GAA TTC GAG GAG CTC [ ... ] CAG GGC CCC GGA TCC GCC
Pro Glu Phe Glu Glu Leu [ ... ] Gln Gly Pro Gly Ser Ala
    EcoRI                                   BamHI
```

Amino acid sequences of RARs are indicated in **bold** print, along with the flanking restriction enzyme sites used for insertion into the Gal4-MCS-VP16 cloning vector.

## 2. UAS-E4$_{TATA}$::fLuc-EGFP reporter construct

UAS-E4$_{TATA}$::fLuc-EGFP reporter construct

```
CAT GCA TTA GTT att aat ccc gag ctc att tag gtg aca cta tag AAT ACA AGC TTG CAT
                VspI       SacI

GCC TGC AGG TCc tCG GAG GAC AGT ACT CCG ctC GGA GGA CAG TAC TCC Gct CGG AGG ACA
 SbfI
  PstI

GTA CTC CGc tCG GAG GAC AGT ACT CCG ctC GGA GGA CAG TAC TCC Gac TCT AGA GGA TCC
                                                                    BamHI

CCA GTC CTA TAT ATA CTC GCT CTG CAC TTG GCC CTT TTT TAC ACT GTG ACT GAT TGA GCT

GGT GCC GTG TCG AGT GGT GTC TCG AGG GGA CCG GTc gcc acc ATG GAA GAC GCC AAA AAC
                                                        Met Glu Asp Ala Lys Asn
                          XhoI         AgeI

ATA AAG AAA GGC CCG GCG CCA TTC TAT CCT CTA GAG GAT GGA ACC GCT GGA GAG CAA CTG
Ile Lys Lys Gly Pro Ala Pro Phe Tyr Pro Leu Glu Asp Gly Thr Ala Gly Glu Gln Leu

CAT AAG GCT ATG AAG AGA TAC GCC CTG GTT CCT GGA ACA ATT GCT TTT ACA GAT GCA CAT
His Lys Ala Met Lys Arg Tyr Ala Leu Val Pro Gly Thr Ile Ala Phe Thr Asp Ala His

ATC GAG GTG AAC ATC ACG TAC GCG GAA TAC TTC GAA ATG TCC GTT CGG TTG GCA GAA GCT
Ile Glu Val Asn Ile Thr Tyr Ala Glu Tyr Phe Glu Met Ser Val Arg Leu Ala Glu Ala

ATG AAA CGA TAT GGG CTG AAT ACA AAT CAC AGA ATC GTC GTA TGC AGT GAA AAC TCT CTT
Met Lys Arg Tyr Gly Leu Asn Thr Asn His Arg Ile Val Val Cys Ser Glu Asn Ser Leu

CAA TTC TTT ATG CCG GTG TTG GGC GCG TTA TTT ATC GGA GTT GCA GTT GCG CCC GCG AAC
Gln Phe Phe Met Pro Val Leu Gly Ala Leu Phe Ile Gly Val Ala Val Ala Pro Ala Asn

GAC ATT TAT AAT GAA CGT GAA TTG CTC AAC AGT ATG AAC ATT TCG CAG CCT ACC GTA GTG
Asp Ile Tyr Asn Glu Arg Glu Leu Leu Asn Ser Met Asn Ile Ser Gln Pro Thr Val Val

TTT GTT TCC AAA AAG GGG TTG CAA AAA ATT TTG AAC GTG CAA AAA AAA TTA CCA ATA ATC
Phe Val Ser Lys Lys Gly Leu Gln Lys Ile Leu Asn Val Gln Lys Lys Leu Pro Ile Ile

CAG AAA ATT ATT ATC ATG GAT TCT AAA ACG GAT TAC CAG GGA TTT CAG TCG ATG TAC ACG
Gln Lys Ile Ile Ile Met Asp Ser Lys Thr Asp Tyr Gln Gly Phe Gln Ser Met Tyr Thr

TTC GTC ACA TCT CAT CTA CCT CCC GGT TTT AAT GAA TAC GAT TTT GTA CCA GAG TCC TTT
Phe Val Thr Ser His Leu Pro Pro Gly Phe Asn Glu Tyr Asp Phe Val Pro Glu Ser Phe

GAT CGT GAC AAA ACA ATT GCA CTG ATA ATG AAT TCC TCT GGA TCT ACT GGG TTA CCT AAG
Asp Arg Asp Lys Thr Ile Ala Leu Ile Met Asn Ser Ser Gly Ser Thr Gly Leu Pro Lys

GGT GTG GCC CTT CCG CAT AGA GCT GCC TGC GTC AGA TTC TCG CAT GCC AGA GAT CCT ATT
Gly Val Ala Leu Pro His Arg Ala Ala Cys Val Arg Phe Ser His Ala Arg Asp Pro Ile

TTT GGC AAT CAA ATC GCT CCG GAT ACT GCG ATT TTA AGT GTT GTT CCA TTC CAT CAC GGT
Phe Gly Asn Gln Ile Ala Pro Asp Thr Ala Ile Leu Ser Val Val Pro Phe His His Gly

TTT GGA ATG TTT ACT ACA CTC GGA TAT TTG ATA TGT GGA TTT CGA GTC GTC TTA ATG TAT
Phe Gly Met Phe Thr Thr Leu Gly Tyr Leu Ile Cys Gly Phe Arg Val Val Leu Met Tyr

AGA TTT GAA GAA GAG CTG TTT TTA CGA TCC CTT CAG GAT TAC AAA ATT CAA AGT GCG TTG
Arg Phe Glu Glu Glu Leu Phe Leu Arg Ser Leu Gln Asp Tyr Lys Ile Gln Ser Ala Leu

CTA GTA CCA ACC CTA TTT TCA TTC CTG GCC AAA AGC ACT CTG ATT GAC AAA TAC GAT TTA
Leu Val Pro Thr Leu Phe Ser Phe Leu Ala Lys Ser Thr Leu Ile Asp Lys Tyr Asp Leu

TCT AAT TTA CAC GAA ATT GCT TCT GGG GGC GCA CCT CTT TCG AAA GAA GTC GGG GAA GCG
Ser Asn Leu His Glu Ile Ala Ser Gly Gly Ala Pro Leu Ser Lys Glu Val Gly Glu Ala
```

UAS-E4$_{TATA}$::fLuc-EGFP reporter construct (continued)

```
GTT GCA AAA CGC TTC CAT CTT CCA GGG ATA CGA CAA GGA TAT GGG CTC ACT GAG ACT ACA
Val Ala Lys Arg Phe His Leu Pro Gly Ile Arg Gln Gly Tyr Gly Leu Thr Glu Thr Thr

TCA GCT ATT CTG ATT ACA CCC AAG GGG GAT GAT AAA CCG GGC GCG GTC GGT AAA GTT GTT
Ser Ala Ile Leu Ile Thr Pro Lys Gly Asp Asp Lys Pro Gly Ala Val Gly Lys Val Val

CCA TTT TTT GAA GCG AAG GTT GTG GAT CTG GAT ACC GGG AAA ACG CTG GGC GTT AAT CAG
Pro Phe Phe Glu Ala Lys Val Val Asp Leu Asp Thr Gly Lys Thr Leu Gly Val Asn Gln

AGA GGC GAA TTA TGT GTC AGA GGA CCT ATG ATT ATG TCC GGT TAT GTA AAC AAT CCG GAA
Arg Gly Glu Leu Cys Val Arg Gly Pro Met Ile Met Ser Gly Tyr Val Asn Asn Pro Glu

GCG ACC AAC GCC TTG ATT GAC AAG GAT GGA TGG CTA CAT TCT GGA GAC ATA GCT TAC TGG
Ala Thr Asn Ala Leu Ile Asp Lys Asp Gly Trp Leu His Ser Gly Asp Ile Ala Tyr Trp

GAC GAA GAC GAA CAC TTC TTC ATA GTT GAC CGC TTG AAG TCT TTA ATT AAA TAC AAA GGA
Asp Glu Asp Glu His Phe Phe Ile Val Asp Arg Leu Lys Ser Leu Ile Lys Tyr Lys Gly

TAT CAG GTG GCC CCC GCT GAA TTG GAA TCG ATA TTG TTA CAA CAC CCC AAC ATC TTC GAC
Tyr Gln Val Ala Pro Ala Glu Leu Glu Ser Ile Leu Leu Gln His Pro Asn Ile Phe Asp

GCG GGC GTG GCA GGT CTT CCC GAC GAT GAC GCC GGT GAA CTT CCC GCC GCC GTT GTT GTT
Ala Gly Val Ala Gly Leu Pro Asp Asp Asp Ala Gly Glu Leu Pro Ala Ala Val Val Val

TTG GAG CAC GGA AAG ACG ATG ACG GAA AAA GAG ATC GTG GAT TAC GTC GCC AGT CAA GTA
Leu Glu His Gly Lys Thr Met Thr Glu Lys Glu Ile Val Asp Tyr Val Ala Ser Gln Val

ACA ACC GCG AAA AAG TTG CGC GGA GGA GTT GTG TTT GTG GAC GAA GTA CCG AAA GGT CTT
Thr Thr Ala Lys Lys Leu Arg Gly Gly Val Val Phe Val Asp Glu Val Pro Lys Gly Leu

ACC GGA AAA CTC GAC GCA AGA AAA ATC AGA GAG ATC CTC ATA AAG GCC AAG AAG GGC GGA
Thr Gly Lys Leu Asp Ala Arg Lys Ile Arg Glu Ile Leu Ile Lys Ala Lys Lys Gly Gly

AAG TCC AAA TTG GGA TCC GGT GGC GGA GGT AGC GGT GGC GGA GGT AGC ATG GTG AGC AAG
Lys Ser Lys Leu Gly Ser Gly Gly Gly Gly Ser Gly Gly Gly Gly Ser Met Val Ser Lys

GGC GAG GAG CTG TTC ACC GGG GTG GTG CCC ATC CTG GTC GAG CTG GAC GGC GAC GTA AAC
Gly Glu Glu Leu Phe Thr Gly Val Val Pro Ile Leu Val Glu Leu Asp Gly Asp Val Asn

GGC CAC AAG TTC AGC GTG TCC GGC GAG GGC GAG GGC GAT GCC ACC TAC GGC AAG CTG ACC
Gly His Lys Phe Ser Val Ser Gly Glu Gly Glu Gly Asp Ala Thr Tyr Gly Lys Leu Thr

CTG AAG TTC ATC TGC ACC ACC GGC AAG CTG CCC GTG CCC TGG CCC ACC CTC GTG ACC ACC
Leu Lys Phe Ile Cys Thr Thr Gly Lys Leu Pro Val Pro Trp Pro Thr Leu Val Thr Thr

CTG ACC TAC GGC GTG CAG TGC TTC AGC CGC TAC CCC GAC CAC ATG AAG CAG CAC GAC TTC
Leu Thr Tyr Gly Val Gln Cys Phe Ser Arg Tyr Pro Asp His Met Lys Gln His Asp Phe

TTC AAG TCC GCC ATG CCC GAA GGC TAC GTC CAG GAG CGC ACC ATC TTC TTC AAG GAC GAC
Phe Lys Ser Ala Met Pro Glu Gly Tyr Val Gln Glu Arg Thr Ile Phe Phe Lys Asp Asp

GGC AAC TAC AAG ACC CGC GCC GAG GTG AAG TTC GAG GGC GAC ACC CTG GTG AAC CGC ATC
Gly Asn Tyr Lys Thr Arg Ala Glu Val Lys Phe Glu Gly Asp Thr Leu Val Asn Arg Ile

GAG CTG AAG GGC ATC GAC TTC AAG GAG GAC GGC AAC ATC CTG GGG CAC AAG CTG GAG TAC
Glu Leu Lys Gly Ile Asp Phe Lys Glu Asp Gly Asn Ile Leu Gly His Lys Leu Glu Tyr

AAC TAC AAC AGC CAC AAC GTC TAT ATC ATG GCC GAC TAT TGT CTA AGC TTC TGT AAG AAC
Asn Tyr Asn Ser His Asn Val Tyr Ile Met Ala Asp Tyr Cys Leu Ser Phe Cys Lys Asn

GGC ATC AAG GTG AAC TTC AAG ATC CGC CAC AAC ATC GAG GAC GGC AGC GTG CAG CTC GCC
Gly Ile Lys Val Asn Phe Lys Ile Arg His Asn Ile Glu Asp Gly Ser Val Gln Leu Ala

GAC CAC TAC CAG CAG AAC ACC CCC ATC GGC GAC GGC CCC GTG CTG CTG CCC GAC AAC CAC
Asp His Tyr Gln Gln Asn Thr Pro Ile Gly Asp Gly Pro Val Leu Leu Pro Asp Asn His

TAC CTG AGC ACC CAG TCC GCC CTG AGC AAA GAC CCC AAC GAG AAG CGC GAT CAC ATG GTC
Tyr Leu Ser Thr Gln Ser Ala Leu Ser Lys Asp Pro Asn Glu Lys Arg Asp His Met Val
```

UAS-E4$_{TATA}$::fLuc-EGFP reporter construct (continued)

```
CTG CTG GAG TTC GTG ACC GCC GCC GGG ATC ACT CTC GGC ATG GAC GAG CTG TAC AAG TAA
Leu Leu Glu Phe Val Thr Ala Ala Gly Ile Thr Leu Gly Met Asp Glu Leu Tyr Lys End

aGC GGC CGC GAC
 NotI
```

The plasmid was made by PCR amplification of the UAS$_5$-E4$_{TATA}$ regulatory sequences and cloning into the pEYFP-N1 plasmid backbone using the *Vsp*I and *Age*I restriction enzyme sites. Next, fLuc-EGFP was amplified by PCR and cloned behind the regulatory sequences using the *Age*I and *Not*I restriction enzyme sites, replacing the EYFP.

The upstream activating sequence (UAS) is highlighted in **yellow**, with UAS repeats printed as capital letters and spacer nucleotides as small letters. The *Herpes simplex* virus E4 TATA box minimal promoter is highlighted in **cyan**, and **fLuc** and **EGFP** amino acid sequence domains of the reporter gene are color indicated in **bold** print. All restriction enzyme sites indicated are unique.

## 3. Modular FRET sensors for RA

NR box gBlock sequence

```
acgGCTAGCatc tcg agc cta cct tat gaa ggc agc ctg ctg ctc aag ctg ctt aga gca
            Ser Ser Leu Pro Tyr Glu Gly Ser Leu Leu Leu Lys Leu Leu Arg Ala
   NheI*    XhoI

cca gta gag gaa gtt gga ggc aat ggt gga gat ctg aTGTACAgcc tcg agt ctg cca tac
Pro Val Glu Glu Val Gly Gly Asn Gly Gly Asp Leu             Ser Ser Leu Pro Tyr
                                    BglII      BsrGI*  XhoI

gag ggc tcg ctg ctg ctc aag ctg ctt aga gct cca gtt gaa gag gtc gga ggt aat ggc
Glu Gly Ser Leu Leu Leu Lys Leu Leu Arg Ala Pro Val Glu Glu Val Gly Gly Asn Gly

ggt aac ggc ggt aac gga ggc aac ggt ggc aat ggt ggc aat gga ggc aat ggt gga gat
Gly Asn Gly Gly Asn Gly Gly Asn Gly Gly Asn Gly Gly Asn Gly Gly Asn Gly Gly Asp
                                                                        BglII

ctg gaGAATTCgcc tcg agt cta cct tac gag ggc agt ctg gct ctt aat gca gcc aga gca
Leu             Ser Ser Leu Pro Tyr Glu Gly Ser Leu Ala Leu Asn Ala Ala Arg Ala
      EcoRI*  XhoI

cct gtg gag gag gtg ggt gga aac ggt gga gat ctg aGGATCCgcc tcg agt ctg cca tac
Pro Val Glu Glu Val Gly Gly Asn Gly Gly Asp Leu             Ser Ser Leu Pro Tyr
                                    BglII      BamHI*  XhoI

gaa ggc agc ctg gcg ctc aag gcg gct agg gca cct gtg gag gaa gtg ggt ggc aac ggt
Glu Gly Ser Leu Ala Leu Lys Ala Ala Arg Ala Pro Val Glu Glu Val Gly Gly Asn Gly

ggc aat gga ggc aat ggc ggc aat gga ggt aac gga ggt aac ggc ggc aat ggc gga gat
Gly Asn Gly Gly Asn Gly Gly Asn Gly Gly Asn Gly Gly Asn Gly Gly Asn Gly Gly Asp
                                                                        BglII

ctg aGCGGCCGCatc
Leu
     NotI*
```

The construct was synthesized as a gBlock fragment (Integrated DNA Technologies, Inc.) and was cloned into the pEGFP-N1 plasmid backbone using the *Nhe*I and *Not*I restriction enzyme sites. Amino acid sequences of NR boxes (corresponding to the D22 peptide, Chang *et al.*, 1999) are indicated in **bold** print, with reading frames as in the final modular FRET sensor constructs. Essential **Leucines** are highlighted in **red** and the corresponding mutated **Alanines** in the binding-deficient NR box mutants are highlighted in **green**. All NR boxes are flanked by *Xho*I and *Bgl*II restriction enzyme sites for cloning into the final modular FRET sensor constructs. For convenience, all NR box variants have been separated by unique restriction enzyme sites as indicated by capital letters. NR boxes as desired were excised using appropriate unique restriction enzyme sites, then digested with *Xho*I and *Bgl*II and introduced into the final modular FRET sensors. All restriction enzyme sites indicated with * are unique.

Rat RARα LBD + F domain sequence

```
gga gat ctg agc tac acg ctg aca ccg gag gtg ggg gaa ctc atc gag aag gtg cgc aaa
Gly Asp Leu Ser Tyr Thr Leu Thr Pro Glu Val Gly Glu Leu Ile Glu Lys Val Arg Lys
  BglII

gca cac cag gag acc ttc ccg gcc ctc tgc cag ctg ggc aag tac act acg aac aac agc
Ala His Gln Glu Thr Phe Pro Ala Leu Cys Gln Leu Gly Lys Tyr Thr Thr Asn Asn Ser

tca aaa caa cgt gtc tct ctg gac att gac ctc tgg gac aag ttc agt gaa ctc tcc acc
Ser Lys Gln Arg Val Ser Leu Asp Ile Asp Leu Trp Asp Lys Phe Ser Glu Leu Ser Thr

aag tgt atc att aag act gtg gag ttc gcc aag cag ctt ccc ggc ttc acc acc ctc acc
Lys Cys Ile Ile Lys Thr Val Glu Phe Ala Lys Gln Leu Pro Gly Phe Thr Thr Leu Thr

att gca gac cag att acc ctt ctc aag gct gcc tgc ctg gac atc ctg att ctg cga atc
Ile Ala Asp Gln Ile Thr Leu Leu Lys Ala Ala Cys Leu Asp Ile Leu Ile Leu Arg Ile

tgc acg cgg tac aca cct gag caa gac aca atg acc ttc tca gat gga ctg acc ctg aac
Cys Thr Arg Tyr Thr Pro Glu Gln Asp Thr Met Thr Phe Ser Asp Gly Leu Thr Leu Asn

cgg act cag atg cac aac gct ggc ttt ggc ccc ctc acc gac ttg gtc ttt gcc ttc gcc
Arg Thr Gln Met His Asn Ala Gly Phe Gly Pro Leu Thr Asp Leu Val Phe Ala Phe Ala

aac cag ctg ctg ccc ctg gag atg gac gat gct gag acc gga ctg ctc agt gcc atc tgc
Asn Gln Leu Leu Pro Leu Glu Met Asp Asp Ala Glu Thr Gly Leu Leu Ser Ala Ile Cys

ctc atc tgt gga gac cga cag gat cta gag cag cca gac aag gtg gac atg ctg cag gag
Leu Ile Cys Gly Asp Arg Gln Asp Leu Glu Gln Pro Asp Lys Val Asp Met Leu Gln Glu

ccg ctg ttg gaa gca ctg aaa gtc tat gtc cgg aaa cgg agg ccc agc cga ccc cac atg
Pro Leu Leu Glu Ala Leu Lys Val Tyr Val Arg Lys Arg Arg Pro Ser Arg Pro His Met

ttc ccc aag atg ctg atg aag atc acg gac ctt cgg agt atc agc gcc aag gga gct gaa
Phe Pro Lys Met Leu Met Lys Ile Thr Asp Leu Arg Ser Ile Ser Ala Lys Gly Ala Glu

        cag
cgg gtg atc aca ttg aag atg gag atc cct ggt tcc atg cca cca ctt atc cag gaa atg
Arg Val Ile Thr Leu Lys Met Glu Ile Pro Gly Ser Met Pro Pro Leu Ile Gln Glu Met
        Gln

ttg gag aac tct gag ggc ttg gac act cta agc gga cag tcg ggg ggc gga aca cga gat
Leu Glu Asn Ser Glu Gly Leu Asp Thr Leu Ser Gly Gln Ser Gly Gly Gly Thr Arg Asp

ggg ggt ggc ctg gcc cct cct ccg ggt agc tgt agc ccc agc ctc agt ccc agc tcc cac
Gly Gly Gly Leu Ala Pro Pro Pro Gly Ser Cys Ser Pro Ser Leu Ser Pro Ser Ser His

aga agc agc cca gcc act caa tct gga tcc gtg
Arg Ser Ser Pro Ala Thr Gln Ser Gly Ser Val
                                 BamHI
```

Amino acid sequence of the RARα **LBD** is indicated in **bold** print and the ***F domain*** in ***bold italic*** print, along with the flanking restriction enzyme sites used for insertion into the modular FRET sensor construct plasmids. The **I393Q** mutation is highlighted in **red**, with mutated nucleotide sequence indicated above and mutated amino acid residue below the wild-type sequence. All restriction enzyme sites indicated are unique.

Modular FRET sensor domain structure and variants


| Plasmid # | NR box* | Linker length** | LBD*** | F domain |
|---|---|---|---|---|
| 664 | D22 (wt) | Short linker | wild-type LBD | no F |
| 665 | D22 (wt) | Long linker | wild-type LBD | no F |
| 666 | D22 (wt) | Short linker | wild-type LBD | + F |
| 667 | D22 (wt) | Long linker | wild-type LBD | + F |
| 668 | D22 (AAA) | Short linker | wild-type LBD | no F |
| 669 | D22 (AAA) | Long linker | wild-type LBD | no F |
| 670 | D22 (AAA) | Short linker | wild-type LBD | + F |
| 671 | D22 (AAA) | Long linker | wild-type LBD | + F |
| 672 | D22 (wt) | Short linker | mutant LBD (I393Q) | no F |
| 673 | D22 (wt) | Long linker | mutant LBD (I393Q) | no F |
| 674 | D22 (wt) | Short linker | mutant LBD (I393Q) | + F |
| 675 | D22 (wt) | Long linker | mutant LBD (I393Q) | + F |
| 676 | D22 (AAA) | Short linker | mutant LBD (I393Q) | no F |
| 677 | D22 (AAA) | Long linker | mutant LBD (I393Q) | no F |
| 678 | D22 (AAA) | Short linker | mutant LBD (I393Q) | + F |
| 679 | D22 (AAA) | Long linker | mutant LBD (I393Q) | + F |

* D22 refers to a peptide identified to bind differentially to the ligand-bound *vs*. unliganded RARα LBD in a peptide library screen (Chang *et al.*, 1999). The wild-type variant, D22 (wt), with the amino acid sequence LPYEGSLLLKLLRAPVEEV, and the binding-deficient variant, D22 (AAA), with the amino acid sequence LPYEGSLALKAARAPVEEV.

** The short linker of 5 residues with the amino acid sequence GGNGG, and the long linker of 23 residues with the sequence $[GGN]_7GG$.

*** The LBD I393Q mutation acts as a beta sheet breaker and destabilizes the domain of the LBD that interacts with transcriptional co-repressors in the unliganded state (le Maire *et al.*, 2010).

## 4. aGEPRA solubility domain

aGEPRA solubility domain sequence

```
aag gat ccc ATG GCT GAA GAA AGT GAC AAT GTG GAT TCT GCT GAT GCG GAG GAG GAT GAC
            Met Ala Glu Glu Ser Asp Asn Val Asp Ser Ala Asp Ala Glu Glu Asp Asp
  BamHI

TCG GAT GTC TGG TGG GGC GGA GCA GAC ACA GAC TAT GCA GAT GGG AGT GAA GAC AAA GTA
Ser Asp Val Trp Trp Gly Gly Ala Asp Thr Asp Tyr Ala Asp Gly Ser Glu Asp Lys Val

GTA GAA GTA GCA GAG GAG GAA GAA GTG GCT GAG GTG GAA GAA GAA GAA GCC GAT GAT GAC
Val Glu Val Ala Glu Glu Glu Glu Val Ala Glu Val Glu Glu Glu Glu Ala Asp Asp Asp

GAG GAC GAT GAG GAT GGT GAT GAG GTA GAG GAA GAG GCT GAG GAA CCC TAC GAA GAA GCC
Glu Asp Asp Glu Asp Gly Asp Glu Val Glu Glu Glu Ala Glu Glu Pro Tyr Glu Glu Ala

ACA GAG AGA ACC ACC AGC ATT GCC ACC ACC ACC ACC ACC ACC ACA GAG TCT GTG GAA GAG
Thr Glu Arg Thr Thr Ser Ile Ala Thr Thr Thr Thr Thr Thr Thr Glu Ser Val Glu Glu

GTG act agt atg [ aGEPRA sequence ]
Val Thr Ser Met [ aGEPRA sequence ]
    SpeI
```

Solubility domain amino acid sequence is indicated in **bold** print, along with flanking restriction enzyme sites. The Met residue at the end of the sequence is the first amino acid residue of the GEPRA variants to which the solubility domain was fused. Sequence of the GEPRA variants is as reported (Shimozono *et al.*, 2013). All restriction enzyme sites indicated are unique.

## 5. Clover-mRuby2 FRET pair

pcDNA3-Clover sequence

```
cca agc ttg gta ccg agc tcg gat cca cta gta acg gcc gcc agt gtg ctg gaa ttc ggc
  HindIII                BamHI                                        EcoRI

ATG GTG AGC AAG GGC GAG GAG CTG TTC ACC GGG GTG GTG CCC ATC CTG GTC GAG CTG GAC
Met Val Ser Lys Gly Glu Glu Leu Phe Thr Gly Val Val Pro Ile Leu Val Glu Leu Asp

GGC GAC GTA AAC GGC CAC AAG TTC AGC GTC CGC GGC GAG GGC GAG GGC GAT GCC ACC AAC
Gly Asp Val Asn Gly His Lys Phe Ser Val Arg Gly Glu Gly Glu Gly Asp Ala Thr Asn

GGC AAG CTG ACC CTG AAG TTC ATC TGC ACC ACC GGC AAG CTG CCC GTG CCC TGG CCC ACC
Gly Lys Leu Thr Leu Lys Phe Ile Cys Thr Thr Gly Lys Leu Pro Val Pro Trp Pro Thr

CTC GTG ACC ACC TTC GGC TAC GGC GTG GCC TGC TTC AGC CGC TAC CCC GAC CAC ATG AAG
Leu Val Thr Thr Phe Gly Tyr Gly Val Ala Cys Phe Ser Arg Tyr Pro Asp His Met Lys

CAG CAC GAC TTC TTC AAG TCC GCC ATG CCC GAA GGC TAC GTC CAG GAG CGC ACC ATC TCT
Gln His Asp Phe Phe Lys Ser Ala Met Pro Glu Gly Tyr Val Gln Glu Arg Thr Ile Ser

TTC AAG GAC GAC GGT ACC TAC AAG ACC CGC GCC GAG GTG AAG TTC GAG GGC GAC ACC CTG
Phe Lys Asp Asp Gly Thr Tyr Lys Thr Arg Ala Glu Val Lys Phe Glu Gly Asp Thr Leu

GTG AAC CGC ATC GAG CTG AAG GGC ATC GAC TTC AAG GAG GAC GGC AAC ATC CTG GGG CAC
Val Asn Arg Ile Glu Leu Lys Gly Ile Asp Phe Lys Glu Asp Gly Asn Ile Leu Gly His

AAG CTG GAG TAC AAC TTC AAC AGC CAC AAC GTC TAT ATC ACG GCC GAC AAG CAG AAG AAC
Lys Leu Glu Tyr Asn Phe Asn Ser His Asn Val Tyr Ile Thr Ala Asp Lys Gln Lys Asn

GGC ATC AAG GCT AAC TTC AAG ATC CGC CAC AAC GTT GAG GAC GGC AGC GTG CAG CTC GCC
Gly Ile Lys Ala Asn Phe Lys Ile Arg His Asn Val Glu Asp Gly Ser Val Gln Leu Ala

GAC CAC TAC CAG CAG AAC ACC CCC ATC GGC GAC GGC CCC GTG CTG CTG CCC GAC AAC CAC
Asp His Tyr Gln Gln Asn Thr Pro Ile Gly Asp Gly Pro Val Leu Leu Pro Asp Asn His

TAC CTG AGC CAT CAG TCC GCC CTG AGC AAA GAC CCC AAC GAG AAG CGC GAT CAC ATG GTC
Tyr Leu Ser His Gln Ser Ala Leu Ser Lys Asp Pro Asn Glu Lys Arg Asp His Met Val

CTG CTG GAG TTC GTG ACC GCC GCC GGG ATT ACA CAT GGC ATG GAC GAG CTG TAC AAG tct
Leu Leu Glu Phe Val Thr Ala Ala Gly Ile Thr His Gly Met Asp Glu Leu Tyr Lys Ser
                                                          BsrGI     XbaI

aga ggg ccc tat tct ata gtg tca cct aaa tgc tag
Arg Gly Pro Tyr Ser Ile Val Ser Pro Lys Cys End
    ApaI
    Bsp120I
```

Clover amino acid sequence is indicated in **bold** print, along with flanking restriction enzyme sites in the pcDNA3 vector. All restriction enzyme sites indicated are unique.

pcDNA3-mRuby2 sequence

```
aag ctt gcg gcc gcc acc atg gtg cgg ggt tct cat cat cat cat cat cat ggt atg gct
HindIII NotI                                                              NheI

agc atg act ggt gga cag caa atg ggt cgg gat ctg tac gac gat gac gat aag gat ccg
                                                                  BamHI

ATG GTG TCT AAG GGC GAA GAG CTG ATC AAG GAA AAT ATG CGT ATG AAG GTG GTC ATG GAA
Met Val Ser Lys Gly Glu Glu Leu Ile Lys Glu Asn Met Arg Met Lys Val Val Met Glu

GGT TCG GTC AAC GGC CAC CAA TTC AAA TGC ACA GGT GAA GGA GAA GGC AAT CCG TAC ATG
Gly Ser Val Asn Gly His Gln Phe Lys Cys Thr Gly Glu Gly Glu Gly Asn Pro Tyr Met

GGA ACT CAA ACC ATG AGG ATC AAA GTC ATC GAG GGA GGA CCC CTG CCA TTT GCC TTT GAC
Gly Thr Gln Thr Met Arg Ile Lys Val Ile Glu Gly Gly Pro Leu Pro Phe Ala Phe Asp

ATT CTT GCC ACG TCG TTC ATG TAT GGC AGC CGT ACT TTT ATC AAG TAC CCG AAA GGC ATT
Ile Leu Ala Thr Ser Phe Met Tyr Gly Ser Arg Thr Phe Ile Lys Tyr Pro Lys Gly Ile

CCT GAT TTC TTT AAA CAG TCC TTT CCT GAG GGT TTT ACT TGG GAA AGA GTT ACG AGA TAC
Pro Asp Phe Phe Lys Gln Ser Phe Pro Glu Gly Phe Thr Trp Glu Arg Val Thr Arg Tyr

GAA GAT GGT GGA GTC GTC ACC GTC ATG CAG GAC ACC AGC CTT GAG GAT GGC TGT CTC GTT
Glu Asp Gly Gly Val Val Thr Val Met Gln Asp Thr Ser Leu Glu Asp Gly Cys Leu Val

TAC CAC GTC CAA GTC AGA GGG GTA AAC TTT CCC TCC AAT GGT CCC GTG ATG CAG AAG AAG
Tyr His Val Gln Val Arg Gly Val Asn Phe Pro Ser Asn Gly Pro Val Met Gln Lys Lys

ACC AAG GGT TGG GAG CCT AAT ACA GAG ATG ATG TAT CCA GCA GAT GGT GGT CTG AGG GGA
Thr Lys Gly Trp Glu Pro Asn Thr Glu Met Met Tyr Pro Ala Asp Gly Gly Leu Arg Gly

TAC ACT CAT ATG GCA CTG AAA GTT GAT GGT GGT GGC CAT CTG TCT TGC TCT TTC GTA ACA
Tyr Thr His Met Ala Leu Lys Val Asp Gly Gly Gly His Leu Ser Cys Ser Phe Val Thr

ACT TAC AGG TCA AAA AAG ACC GTC GGG AAC ATC AAG ATG CCC GGT ATC CAT GCC GTT GAT
Thr Tyr Arg Ser Lys Lys Thr Val Gly Asn Ile Lys Met Pro Gly Ile His Ala Val Asp

CAC CGC CTG GAA AGG TTA GAG GAA AGT GAC AAT GAA ATG TTC GTA GTA CAA CGC GAA CAC
His Arg Leu Glu Arg Leu Glu Glu Ser Asp Asn Glu Met Phe Val Val Gln Arg Glu His

GCA GTT GCC AAG TTC GCC GGG CTT GGT GGT GGG ATG GAC GAG CTG TAC AAG TAA gaa ttc
Ala Val Ala Lys Phe Ala Gly Leu Gly Gly Gly Met Asp Glu Leu Tyr Lys End
                                                        BsrGI          EcoRI

tct aga ggg ccc
XbaI    ApaI
        Bsp120I
```

mRuby2 amino acid sequence is indicated in **bold** print, along with flanking restriction enzyme sites in the pcDNA3 vector. All restriction enzyme sites indicated are unique.

pcDNA3-Clover-mRuby2 fusion vector sequence

```
ATG [ ... ] TAC AAG tct agc atg act ggt gga cag caa atg ggt cgg gat ctg tac gac
Met [ ... ] Tyr Lys Ser Ser Met Thr Gly Gly Gln Gln Met Gly Arg Asp Leu Tyr Asp

gat gac gat aag gat ccg ATG GTG [ ... ] AAG TAA gaa ttc tct aga ggg ccc
Asp Asp Asp Lys Asp Pro Met Val [ ... ] Lys End         XbaI    ApaI
```

mRuby2 was excised using *Nhe*I and *Apa*I and intoduced into the pcDNA3-Clover plasmid digested with *Xba*I and *Apa*I. Destroyed restriction enzyme sites from *Xba*I/*Nhe*I compatible ends ligation is indicated by dashed underline. **Clover** and **mRuby2** amino acid sequence domains of the fusion protein are color indicated in **bold** print. All restriction enzyme sites indicated are unique.